POLITECNICO

MILANO 1863

SCUOLA DI INGEGNERIA INDUSTRIALE E DELL' INFORMAZIONE

Laurea Magistrale In Ingegneria Meccanica

An Experimental, Analytical and Numerical Study of FOWT's Unsteady Aerodynamics

Supervisors:

Prof. Alberto Zasso

Ing. Paolo Schito

Candidate:

Simone Mancini

ID: 898194

Academic Year 2018-2019

Acknowledgements

Table of Contents

List of Figures

LIST OF FIGURES

List of Tables

Symbols and Conventions

Reference system

This is the frame of reference used throughout this Thesis. The turbine's rotational speed vector is directed as the x axis.
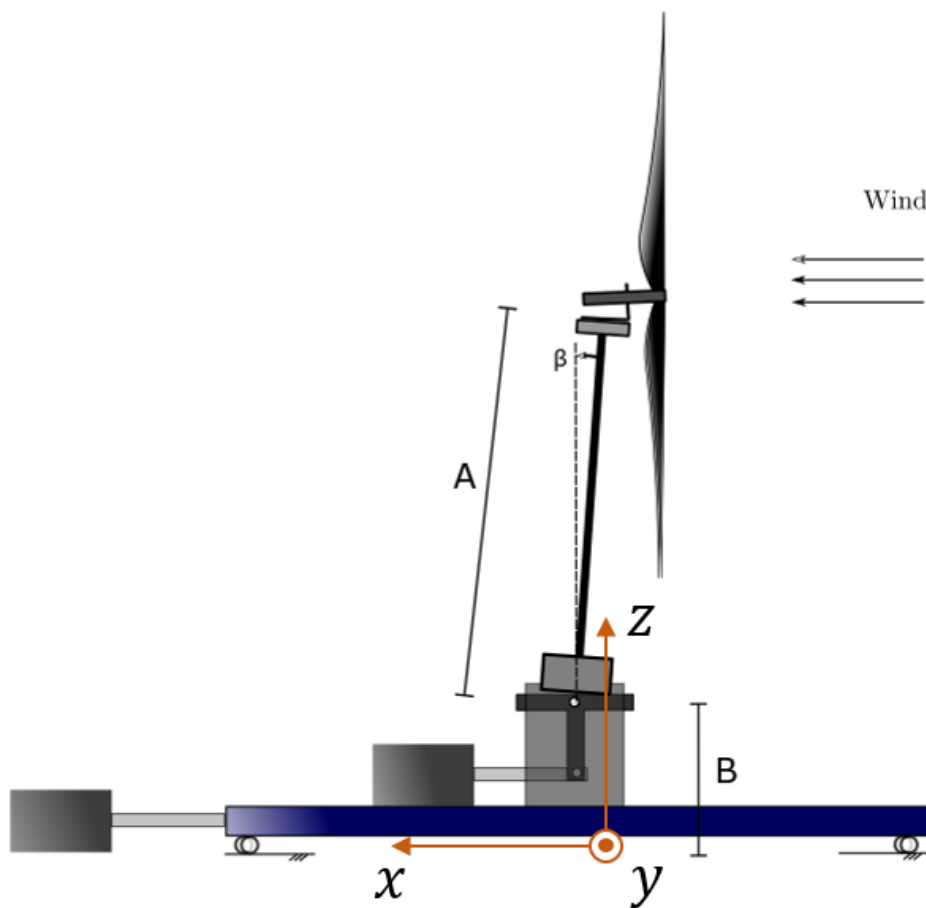
List of Symbols

$a \, [-] -$ Axial induction coefficient

$\hat{\mathbf{a}} \, [-] -$ Versor of the axial direction (along wind)

$a^* \, [-] -$ Rescaled axial induction coefficient (eq.5.4)

$a_0 \, [-] -$ Axial induction coefficient at $\vartheta_p = 0^o$

$a_6 \, [-] -$ Axial induction coefficient at $\vartheta_p = 6^o$

$A_D \, [m^2] = \pi R^2 -$ Turbine model's swept area

$A_s \, [m] -$ Imposed surge displacement amplitude

$a_t \, [-] -$ Tangential induction coefficient

$a1, a2 \, [-] -$ Coefficients of $\varphi(f_{red})$

$ACC \, [m/s^2] -$ Nacelle's accelerometer signal

$\alpha \, [^o] -$ Angle of attack (i.e. between chord and relative velocity)

$\beta \, [-] -$ Amplitude reduction coefficient of the extended

quasi-static model

$b1 \, [-] -$ Coefficient of $\beta(f_{red})$

$c \, [m] -$ Blade's chord

$c_0 \, [Kg/s] -$ Quasi-static aerodynamic damping coefficient

$c_{aero} \, [Kg/s] -$ Aerodynamic damping coefficient

$C_D \, [-] -$ Airfoil's drag coefficient

$C_L \, [-] -$ Airfoil's lift coefficient

$C_p \, [-] -$ Turbine's power coefficient

$C_s \, [-] -$ Smagorinsky's SGS model constant

$c_{str} \, [Kg/s] -$ Tower's structural damping coefficient (1 D.o.F. equivalent)

$C_T \, [-] -$ Turbine's thrust coefficient

$c1, c2 \, [1/s, m/s] -$ Coefficients of the equation of the line in fig.4.2b

$\chi \, [-] -$ Number of cells per actuator line

$d \, [m] -$ Distance between the cell center considered and the one

where the force is applied

$\mathbf{D}\,[N]$ – Drag force (vector)

$D\,[m]$ – Turbine model's diameter

$\Delta\,[mm]$ – LES filter size

$\Delta a\,[-]$ – Axial induction oscillation

$\Delta\alpha\,[^o]$ – Angle of attack oscillation

$\Delta P\,[W] = P - P_0$ – Power oscillation

$\Delta T\,[N] = T - T_0$ – Thrust force oscillation

$\Delta t\,[s]$ – Time step size

$\Delta\vartheta_p\,[^o]$ – Pitch step size

$\Delta V\,[m/s] = 2\pi f_s A_s$ – Amplitude of the surge velocity oscillation

$\varepsilon\,[m]$ – Regularization Kernel's smearing parameter

$\eta_{RK}\,[m^{-2}]$ – Regularization Kernel function

$\mathbf{f}\,[N/m^3]$ – Source term: force field per unit volume (vector)

$F^{ATI}\,[N]$ – ATI balance measurement, positive in -x direction

$f_I\,[Hz]$ – Turbine's first vibration mode frequency (i.e. tower's cantilever bending mode)

$f_{red}\,[-] = \dfrac{f_s D}{V_0}$ – Turbine's reduced frequency

$f_{red}^{airfoil}\,[-] = \dfrac{f_s c}{W_D}$ – Airfoil's reduced frequency

$f_s\,[Hz]$ – Imposed surge displacement frequency

$f_{samp}\,[Hz]$ – Sampling frequency

$\mathbf{f}_V\,[N/Kg]$ – Volume force field per unit mass (vector)

$h\,[m]$ – Spanwise length of the actuator line segment

$h_{HUB}\,[m]$ – Turbine model's hub height

$k\,[N/m]$ – Tower's stiffness coefficient (1 D.o.F. equivalent)

$\mathbf{L}\,[N]$ – Lift force (vector)

$l_{cell}\,[mm]$ – Characteristic cell length

$\lambda\,[-] = TSR = \dfrac{\Omega R}{V_0}$ – Tip Speed Ratio

$\lambda_0\,[-]$ – Operating Tip Speed Ratio

Symbols and Conventions

$$\lambda_w\,[-] = \frac{\Omega R}{(V_0 - \dot{x})} - \text{Tip Speed Ratio accounting for surge motion}$$

$$M\,[-] - \text{Mach number}$$

$$m\,[Kg] - \text{Mass of nacelle, hub and rotor}$$

$$M_0\,[Nm] - \text{Mean torque generated}$$

$$m_{aero}\,[Kg] - \text{Aerodynamic mass coefficient}$$

$$\mu\,[Pa\,s] - \text{Air dynamic viscosity}$$

$$\nu\,[m^2/s] = \mu/\rho - \text{Air kinematic viscosity}$$

$$\nu_{SGS}\,[m^2/s] - \text{SGS kinematic viscosity}$$

$$N_s\,[-] - \text{Number of samples}$$

$$\Omega\,[rad/s] - \text{Turbine's rotational speed}$$

$$p\,[Pa] - \text{Pressure field}$$

$$P\,[W] - \text{Power}$$

$$\bar{p}\,[Pa] - \text{LES filtered pressure field}$$

$$p'\,[Pa] - \text{LES sub-filtered pressure field}$$

$$P_0\,[W] - \text{Steady or mean power}$$

$$\phi\,[^o] = \angle\Delta T - \angle x\,(\text{or } x_B) - \text{Thrust force oscillation's phase with respect}$$
$$\text{to the surge displacement}$$

$$\varphi\,[^o] - \text{Phase delay of the extended quasi-static model}$$

$$\psi\,[^o] = \angle x_{SIW} - \angle x_{NOW} - \text{Phase shift between SIW and NOW responses}$$

$$R\,[m] = 0.5D - \text{Turbine model's radius}$$

$$Re\,[-] - \text{Reynolds number}$$

$$\rho\,[Kg/m^3] - \text{Air density}$$

$$t\,[s] - \text{Time}$$

$$\hat{\mathbf{t}}\,[-] - \text{Versor of the tangential direction}$$

$$T\,[N] - \text{Thrust force}$$

$$T^*\,[-] - \text{Non-dimensional thrust force (eq.5.1)}$$

$$T_0\,[N] - \text{Steady or mean thrust force}$$

$$T_6\,[N] - \text{Steady or mean thrust force at } \vartheta_p = 6^o$$

$$t_p\,[s] - \text{Time to complete the blade pitch step}$$

$$T_{rev}\,[s] = \frac{2\pi}{\Omega} - \text{Rotor's revolution period}$$

$$\tau\,[s] - \text{Generic time constant of the thrust decay}$$

$$\tau^*\,[-] = \frac{\tau V_0}{D} - \text{Non-dimensional time constant for thrust decay}$$

$$\tau^{**}\,[-] = \frac{\tau V_0(1-1.5a)}{D} - \text{Non-dimensional time constant for thrust decay}$$

$$\tau_A\,[s] = \frac{c}{W_D} - \text{Characteristic time of airfoil's unsteadiness}$$

$$\tau_B\,[s] - \text{Characteristic time constant for backward pitch}$$
$$\text{step (loading)}$$

$$\tau_F\,[s] - \text{Characteristic time constant for forward pitch}$$
$$\text{step (unloading)}$$

$$\tau_R\,[s] = \frac{D}{V_0} - \text{Characteristic time of rotor's unsteadiness}$$

$$\vartheta_p\,[^o] - \text{Blade pitch}$$

$$\dot{\vartheta}_p\,[^o/s] - \text{Blade pitch actuation velocity}$$

$$\mathbf{u}\,[m/s] - \text{Velocity field (vector)}$$

$$\overline{\mathbf{u}}\,[m/s] - \text{LES filtered velocity field (vector)}$$

$$\mathbf{u}'\,[m/s] - \text{LES sub-filtered velocity field (vector)}$$

$$\hat{\mathbf{u}}_D\,[-] - \text{Versor of the drag direction } (\parallel \mathbf{W}_D)$$

$$\hat{\mathbf{u}}_L\,[-] - \text{Versor of the lift direction } (\perp \mathbf{W}_D)$$

$$V_0\,[m/s] - \text{Undisturbed wind speed}$$

$$V_a^D\,[m/s] - \text{Absolute axial velocity in the rotor plane}$$

$$\overline{V}_a^{down}\,[m/s] - \text{Azimuthal averaged axial velocity in the}$$
$$\text{downstream sampling plane}$$

$$\overline{V}_a^{up}\,[m/s] - \text{Azimuthal averaged axial velocity in the upstream}$$
$$\text{sampling plane}$$

$$V_t^D\,[m/s] - \text{Absolute tangential velocity in the rotor plane}$$

$$\overline{V}_t^{down}\,[m/s] - \text{Azimuthal averaged tangential velocity in the}$$
$$\text{downstream sampling plane}$$

$$\overline{V}_t^{up}\,[m/s] - \text{Azimuthal averaged tangential velocity in the}$$
$$\text{upstream sampling plane}$$

$$V_w \, [m/s] = V_0 - \dot{x} - \text{Relative wind speed due to surge}$$

$$\mathbf{W}_D \, [m/s] - \text{Relative velocity in the rotor plane (vector)}$$

$$W_D \, [m/s] - \text{Norm of the relative velocity in the rotor plane}$$

$$\mathbf{x} \, [m] - \text{Generic position (vector)}$$

$$x, \dot{x}, \ddot{x} \, [m, m/s, m/s^2] - \text{Nacelle's displacement, velocity, acceleration}$$

$$x_B, \dot{x}_B, \ddot{x}_B \, [m, m/s, m/s^2] - \text{Basis' imposed displacement, velocity, acceleration}$$

$$x_{samp}^{down} \, [m] = 0.1D - \text{Downstream sampling plane axial position}$$

$$x_{samp}^{up} \, [m] = -0.1D - \text{Upstream sampling plane axial position}$$

$$\zeta_0 \, [N] - \text{Quasi-static proportionality coefficient}$$

$$\text{linking power output to } \dot{x}$$

Sommario

L'eolico flottante potrebbe segnare un punto di svolta nell'intero settore offshore. Tale tecnologia avrebbe infatti il potenziale di risolvere molti dei problemi che hanno limitato l'interesse nelle OWT a pochi paesi del mondo. Nonostante le prove preliminari siano state superate, lo sviluppo si trova ancora in una fase iniziale, in cui gli alti costi d'investimento tengono questa soluzione lontana dall'essere economicamente competitiva. Per contribuire all'abbattimento dei costi è necessario, tra le altre cose, investire nella ricerca sull'aerodinamica non stazionaria, acquisendo le conoscenze necessarie alla progettazione delle strategie di controllo. In assenza di una sottostruttura rigida infatti, le turbine sono soggette ad ampi spostamenti durante il loro normale funzionamento. Questi spostamenti causano una variazione dei carichi, in particolar modo aerodinamici, che potrebbero comportare problemi di stabilità oltre che la riduzione della vita a fatica. Un buon controllore dovrebbe garantire la stabilità, possibilmente riducendo anche le sollecitazioni tempo-varianti. Pertanto, non si può fare a meno di una conoscenza approfondita del comportamento non stazionario. Allo stesso tempo c'è una forte necessità di validazione dei codici numerici necessari alla progettazione, dato che i dati sperimentali non sono ottenibili a basso costo. Tuttavia, oltre che dei codici aerodinamici più avanzati, i controllisti hanno bisogno anche di modelli semplici in grado di riprodurre il comportamento globale della macchina [17], su cui basare i conti preliminari.

Con questa Tesi si è cercato di venire il più possibile incontro a tali esigenze. Il lavoro è completamente focalizzato sullo studio della risposta non stazionaria della forza di thurst ad uno spostamento armonico del rotore, assunto imposto, nella direzione del vento (surge). La scelta è stata dettata dall'importanza che questa forza ha nella dinamica di una FOWT e dalla volontà di ottenere una descrizione sufficientemente approfondita del suo comportamento, contribuendo così all'incremento della consapevolezza aerodinamica. La Tesi è ampiamente

basata sul lavoro svolto nel progetto UNAFLOW [11]. Tuttavia, una completa revisione è stata portata a termine e le differenze rispetto al lavoro originale sono notevoli. Per prima cosa, i risultati delle prove in galleria del vento sono stati rivisti e validati, verificando l'influenza della flessibilità della torre (Capitolo 2). In quest'ottica anche una nuova procedura per la sottrazione dell'inerzia dai dati sperimentali è stata sviluppata. Nel Capitolo 3 invece, il set up delle simulazioni svolte col codice Actuator Line è puntualmente descritto. Il nuovo paragone tra dati numerici, risultati sperimentali corretti e modello quasi-statico è riportato nel Capitolo 4. Grazie al contributo di alcuni partner, diversi modelli hanno preso parte al confronto: un modello CFD completo (da USTUTT); un modello BEM e un modello ai vortici AWSM (entrambi da TNO); un altro modello ai vortici (da Corniglion di EDF); il modello AL utilizzato dall'Autore. Il paragone ha rivelato un ottimo accordo tra i risultati sperimentali, la CFD, i modelli di TNO e la teoria quasi-statica. Anche gli altri due codici hanno previsto gli stessi trend, ma con la medesima discrepanza rispetto al valore di thrust del caso statico. Data l'assenza di comportamenti non stazionari nel range di frequenze di UNAFLOW, nel Capitolo 5 sono stati considerati casi con frequenze maggiori per verificare l'effetto del dynamic inflow sulla risposta al surge. Entrambi i codici utilizzati hanno identificato due effetti dinamici sulla componente dell'oscillazione di thrust alla frequenza di surge: una riduzione dell'ampiezza ed un ritardo di fase. Entrambi i fenomeni hanno mostrato una dipendenza quadratica dalla frequenza ridotta. In ottemperanza agli obiettivi descritti, un'estensione del modello quasi-statico è stata sviluppata, per permettere di considerare questi effetti in maniera semplice nella progettazione di un controllore. Il lavoro svolto per questa Tesi sarà la base di almeno una pubblicazione su rivista internazionale.

Abstract

FOWTs represent a new frontier for the wind energy field. This technology has the potential of solving most of the issues that have hampered the spreading of OWTs worldwide, signing a breakthrough for the whole market. Being at an infant development stage, the LCOE of these machines is still high and several challenges have to be faced to make the investment attractive. A critical aspect is the control of such devices, owing to the complexity that comes from the coupling of the aerodynamic and hydrodynamic worlds. Lacking a rigid foundation the turbines undergo large displacements during normal operation, generating relevant unsteady loads that affect both their fatigue life and stability. A deep knowledge of those phenomena is required to design effective controllers. Due to the high costs associated with experimental tests, numerical codes play a major role in the design of FOWTs. Then, a great need of validation and comparison of unsteady results has arisen. In parallel to that, also the development simpler models for preliminary controller design is a must [17].

The scope of this Thesis was defined trying to meet those needs. The work is focused on the unsteady aerodynamic response of the thrust force to an imposed harmonic surge motion. The thrust was considered because of its leading role in FOWTs' dynamics. Such a vertical approach was justified by the will of adding a solid brick in the unsteady aerodynamic knowledge framework. The grounds for this work were laid by the UNAFLOW project [11], from which part of the analysis was inherited. However, a complete revision of all the results is hereby presented. First, the wind tunnel tests were verified and validated estimating the impact of tower's flexibility; an alternative inertia subtraction procedure was indeed proposed, in order to increase the accuracy of the measurements (Chapter 2). In Chapter 3 the detailed set up of the Actuator Line simulations performed by the Author is described. The full comparison among numerical models, revised experimental results and quasi-static theory is reported in Chapter 4. The test

matrix was taken from the UNAFLOW campaign, but the codes' results were all updated. Thanks to the cooperation of the partners, the joint comparison comprehended: a full CFD model (from USTUTT); BEM and AWSM codes (from TNO); another free vortex code from Corniglion (EDF); Author's AL simulations. A very good agreement among experimental tests, CFD, TNO's results and quasi-static model was observed. The right trends were also captured by FVW and AL codes, although with a systematic error in the thrust amplitude that reflected the mismatch found in the steady condition. To investigate the effects of rotor unsteadiness (dynamic inflow), it was decided to consider also higher frequency cases in Chapter 5. Both FVW and AL spotted two unsteady trends, characterizing the thrust oscillation component at the surge frequency: an amplitude reduction effect and a phase delay. Both showed a quadratic trend with the reduced frequency. Also a simple extension of the quasi-static model was proposed, to account for these phenomena in preliminar design of a FOWT's controller. The work performed for this Thesis is leading to at least one joint publication with the partners involved.

KEYWORDS: floating offshore, wind turbine, surge, unsteady aerodynamics, CFD, Actuator Line, Free Vortex, BEM, quasi-static theory.

Chapter 1

Introduction

The Paris Agreement for climate change has set very ambitious targets for global warming impact reduction. The final goal is to keep the long-term global average temperature increase below $2°C$. Thus, it is necessary to "achieve a balance between anthropogenic emissions by sources and removals by sinks of greenhouse gases" as soon as possible [1]. To fulfill this commitment, CO_2 emissions have to be cut drastically in the medium term and the only way to do that is to shift towards carbon free energy sources. Despite the future share of renewables in the TPES is still an open debate, their central role in the energy mix is certain. Fortunately, one of the keys of the incoming energetic revolution is already in our hands: the wind power technology. In this chapter, first an overview on wind energy is provided in Section 1.1; then, a focus on the novel floating technology is given in Section 1.2; Section 1.3 discusses the unsteady aerodynamics of HAWTs and Section 1.4 remarks the importance of its comprehension; finally, a zoom in the dynamic inflow phenomenon is provided in Section 1.5. Since the great majority of the currently installed capacity is horizontal axis, unless diversely stated, with the generic term "wind turbine" an HAWT design is implied in this Thesis.

1.1 Wind energy outlook

The idea of exploiting wind as a power source is a very old one. Since ancient times, sailors have relied on wind to allow for small boats to travel long distances. Nevertheless, the first trace of rotating wind powered device dates back to the *I* century B.C. when Heron of Alexandria invented his *windwheel*. Signs of primeval

machines were also found in China. By the way, the closest ancestor of modern wind turbines is the windmill, which was brought in Europe from Persia by crusaders of the *Middle Age*. By the *XIV* century, this technology became very popular in the Netherlands and it has remained an iconic symbol of that country till today. The first wind turbine for electricity production, instead, was made in Scotland by Prof. James Blyth in 1887; his prototype was used to charge a battery. During the last century, several machines were installed especially in Northern Europe, but their use was often other than electricity production (typically water pumping in agricultural fields). Until 1973, in fact, petroleum derived fuels were thought as the only interesting way for making electricity. That year the price of oil rose dramatically and Governments understood that it was not wise to fully entrust their energy production on fossil (i.e. limited) resources. Henceforth, several research programs were funded in Europe and U.S. providing a significant push to the development of modern wind turbines.

Current wind technology is, besides solar photo-voltaic, the most promising solution to accomplish the required shift towards renewable energy. In the period 1990-2017, wind energy production experienced an average annual growth rate of 23.4% according to IEA [2]; the highest among all renewable sources exception made for the PV technology. This fast growth has resulted in an industry that is now present in more than 90 countries, 30 of which have more than 1GW already installed and 9 have more than 10GW. The total installed capacity in 2018 was estimated by the Global Wind Energy Council at 591GW [3], with China, U.S. and Northern Europe (Germany on top) being leaders worldwide. In the same year the new installations amounted to 51.3GW globally. GWEC forecasts that installed power will rise steadily of about 55GW per year till 2023, i.e. with an average annual rate of +2.7%. The drivers of this growth are expected to be the penetration in new markets, new financial solutions allowing to reduce investment's risk and, most importantly, governmental support measures. Since Europe and U.S. alone cannot provide such a growth in the near term, a major contribution will be given by developing markets in Latin America (e.g. Brazil, Argentina, Columbia) and South-Eastern Asia (mainly Thailand, Indonesia, Philippines and Vietnam). New financial solutions, capable of increasing the appeal of wind farm projects appraisal are also arising. A significant contribution is expected from long term corporate PPAs that guarantee an important risk relief for plants owners. Nevertheless, the LCOE of wind farms is not yet competitive with respect to

alternatives like CCGT plants, regardless the substantial drop occurred since the infant stage of the technology. At the time of writing a common range of LCOE for wind turbines is at 50-60 €/MWh, whilst for advanced combined cycle plants is around 35-50 €/MWh. This makes the action of politics fundamental to aid the market development by partial funding of construction projects, incentives, green certificates or any other measure that helps either reducing the costs of wind energy or increasing the costs of competitive fossil sources. These actions are inevitable if the near term targets of CO_2 reduction have to be met: the current growth rate of renewables is still far from meeting the Paris Agreement objectives.

1.1.1 Offshore wind energy

In the last decade, offshore wind turbine technology (OWT) has become a concrete alternative to its inland counterpart. The first offshore turbine was installed in Sweden in 1990, but, ever since 2010, the interest in such technology remained very limited (fig.1.1). Then, with the reduction of the number of possible inland sites and the maturity level reached by wind turbines, the offshore market experienced an important growth. Quantitatively, in the period 2010-2018 the mean yearly growth rate was close to 30% [4]. The main reason for this development were the valuable advantages versus classical WTs:

1. **Noise emission**: placing the turbines offshore eliminates the problem of acoustic emissions since no person is affected.

2. **Visual impact**: as for noise emission, if the turbine is placed kilometers away from the shore, visual pollution problem is avoided.

3. **Capacity Factor**: offshore turbines have shown to reach higher capacity factors (typically around 50%) than inland. For this reason offshore wind is often referred as a baseload renewable source.

4. **Turbines size**: since the turbines are assembled in harbours and then carried offshore, there is virtually no limit to the size of the machine unlike inland, where the available roads represent a strict constraint.

5. **Favourable sites**: a number of offshore sites are available, all characterized by high average wind speeds, low T.I. and less sheared wind profile.

It is worth to notice that the first two points alone drastically reduce the risk of unsuccessful outcome of the construction project, since public authorities will be less worried of the impact on local population. Although, these advantages are obtained at the expense of a much higher LCOE (around 90-120 €/MWh at the time of writing) and it is not easy to foresee when and whether, with the maturity of the technology, this cost gap will be cancelled. The main cause of such increase is the relevant investment cost to be sustained. The turbine does not require any significant change in its design, just some additional measures to cope with the harsh marine environment (e.g. corrosion resistant blades and tower paints, nacelle and tower air drying systems, etc...); these features are not cheap but are only a minor part of the problem. The bulk of the expense is due to the purchase and installation of the underwater substructure, which is largely inherited from the oil & gas industry. The main driver is the huge foundation that has to be laid on the seabed. Another voice of cost is the underwater cables system (big R&D investments from giants like Siemens are being devoted to find more cost efficient solutions). The last relevant contribution is due to the rental of very unique floating crane devices to lay the turbine on its supporting structure (e.g. *Saipem 7000*).

At the end of 2018, the total offshore installed capacity was 23.1 GW: about 4% of the total wind energy capacity (figure 1.1). Such data included also the small share of floating technology (discussed in Section 1.2). This overall capacity is foreseen to rise up to 100GW within 2025, with a major contribution from Asian market (mainly Taiwan, Japan and South Korea) [3].

At the moment, the only way to make offshore technology affordable -even with relevant governmental funding- is to exploit the economy of scale. Thus, to install the biggest turbines available in large farms rated hundreds of MW. The future importance of the offshore market is confirmed by the effort that OEMs are making towards a continuous increase in the size of their largest designs, for example: Siemens Gamesa (SGRE) is now producing a ⌀167m turbine (SG 8.0-167DD™) rated up to 8MW and it is developing a ⌀193m rated 10MW for 2022 (SG 10.0-193DD™); MHI Vestas is commercializing a ⌀164m turbine (V164™) up to 10MW and it is enlarging the size to ⌀174m (V174™); GE Renewables is developing the huge ⌀220m Haliade-X 12MW™.

Historic development of new installations
GW
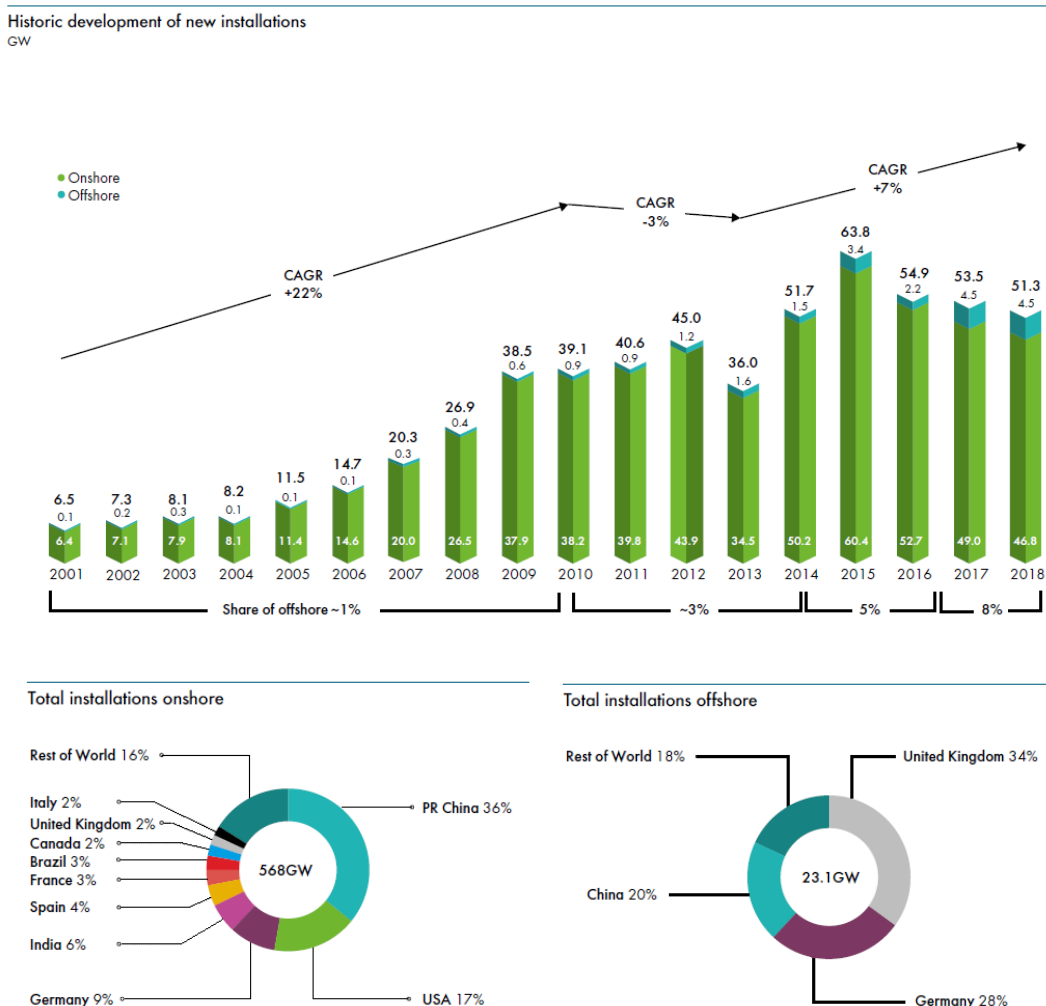
Figure 1.1: installed capacity trends inland and offshore (2018). *Source*: GWEC [3]

1.2 FOWT

The establishment of OWT technology has significantly increased the wind's potential energy output. IEA estimates that Europe alone has a yearly potential of about 33840TWh, which is almost 50% more than the current global electricity demand [4]. The relevant P&I costs of the underwater substructure though, hinder the full exploitation of such potential, making OWTs projects appealing only in shallow waters; above 40-50m of water depth, even with public support, the NPV of the investment tends to zero. For this reason, the interest in classical offshore wind was limited to few regions in the North Sea and off the coast of China, where favourable conditions are met. Neither North America nor the Mediterranean

part of Europe could benefit of this new technology. In these terms one can understand the outstanding potential of the latest development in the offshore field: the floating wind turbine (FOWT). The basic concept is the substitution of the stiff underwater structure with a floating substructure, anchored to the seabed by chains or cables. This would loosen the depth constraint dramatically. In fact, the absence of foundation and underwater frame means that water depth only affects the cost of the mooring lines, with a much lower relevance. Such a feature might result in a breakthrough for embracing new markets. Another advantage is the reduced environmental impact and decommissioning costs due to the lack of foundation.

The first to theorize a floating turbine was Prof. W.E. Heronemus (University of Massachusetts) in 1972, but the research community interest grew only after the first OWTs were put in operation in the 90's. The first to test a FOWT prototype were the Dutch of Blue H Technologies who installed a small 80KW 2-bladed unit on a tension-leg floating platform (fig.1.2), located ∼20Km off the coast of Puglia (Italy) at a depth of 113m in December 2007. However, the most important milestone was laid by Equinor (former Statoil) that installed the Hywind Demo turbine (a SGRE 2.3MW, ⌀85m) in 220m deep waters offshore Karmøy (Norway) in October 2009. The turbine was operated for 2 years to validate their Hywind™ floater concept, first conceived back in 2001. This design relies on a single tubular ballast underneath the turbine's tower, anchored to the seabed with cables just like a spar buoy (fig.1.2). The success of the demo project led the company to inaugurate the World's first floating wind farm in October 2017: the 30MW Hywind Scotland Park, made out of 6x⌀154m turbines located 30Km off the coast of Peterhead. The plant is still in operation and showed a CF over 50% in its first 2 years of life, confirming the baseload capabilities of offshore wind plants. Almost in parallel to Hywind™, Principle Power Inc. developed the WindFloat® floater concept. WindFloat® is a semi-submersible platform that relies on three tubular pillars with water entrapment plates for floating (similar to what shown in fig.1.2) and a ballast beneath for stability. The key advantage with respect to Equinor's design is that the draft of the floater can be minimized by emptying the entrapment plates. This feature provides the possibility to install the turbine on the floater directly in the harbour. Then, the complete assembly can be towed onsite where the mooring lines are fixed. Such characteristic allows for an important simplification of the installation phase,

reducing its cost significantly; floating crane vessels are not required anymore. It is also possible to tow the turbine back to the harbour when maintenance is needed, likely reducing O&M costs too. WindFloat® was first tested within the WindFloat1 pilot project from 12/2011 until 09/2016. It sustained a 2MW ∅80m turbine off the coast of Aguçadoura (Portugal), surviving wind and waves storms and producing about 17GWh before decommissioning.

Figure 1.2: main floater types: spar buoy (left), semi-submersible (middle), and tension-leg platform (right). *Source*: Josh Bauer/NREL

1.2.1 Industry status

The Hywind Demo aroused great interest from both the scientific and industrial communities. Several big oil & gas companies caught the business opportunity, since they already had deep knowledge in the offshore field and they believed in the long term profit potential of FOWTs. Several joint-ventures were created between energy and O&G players to share risks and knowledge. One example is the Wind Plus consortium (among EDP Renewables, Engie, Repsol and Principle Power Inc.) that, exploiting the WindFloat® floater, is completing the WindFloat Atlantic project: 3x8.4MW V-164™ turbines located 20Km off Viana Do Castelo (Portugal). The first of these turbines was connected to the grid in January 2020. Equinor instead, is planning an 88MW off-grid farm based on its Hywind™ design, called Hywind Tampen. The farm will be located in the middle of the North Sea to power two Equinor's oil platforms, witnessing the off-grid potential of this technology. At the time of writing, the installed capacity is within 100-200MW worldwide but the number of announced projects is soaring. Most of them rely on multi-leg semi-submersible platforms because of the advantages previously

discussed. The most active regions are Europe (mainly France, Portugal and Scotland) and Asia-Pacific (mainly Japan). In France for example, at least three pilot projects have already reached financial close, namely: 25MW Provence Grand Large (sponsored by EDF Renewables); 30MW les Eoliennes Flottantes du Golfe du Lion (sponsored by WindPlus); 28.5MW les Eoliennes Flottantes de Groix et Belle-Ile (sponsored by EOLFI, CGN Europe Energy and public administration).

The future of FOWT strictly depends on the outcomes of these pilot projects in the next decade. The investing companies forecast that ~10% of the offshore installed capacity will be floating by 2030. Due to the early infant stage of this technology it is difficult to say whether it will be competitive versus OWTs or inland WTs. What is clear is that there are still big challenges to face. The cost of the floaters is really high at the moment, even higher than OWT's foundation P&I cost. A sharp decrease is expected though, because at a certain point one floating solution will outperform the others and a serial production will shrink the costs. At the same time, massive research is required to study the dynamics of these complex systems.

1.2.2 Research status

The lack of rigid substructure let FOWTs undergo large displacements that will affect the turbine's aerodynamics. Since aerodynamic forces are transferred by the tower to the floater, they will affect the buoyancy of the system creating a complex non-linear coupling. Several aero-hydrodynamic codes were developed for designing floating turbines. One of the most popular is the FAST code, developed by NREL, which allows to include the HydroDyn subroutine for coupled aero-hydro-servo-elastic simulations. Although, due to the complexity of the coupling, the aerodynamic modelling is performed by a BEM solver. The first to underline the limitations of such models for FOWTs were Sebastian and Lackner [5]. They showed that the aerodynamic unsteadiness in floating turbines operation could not be adequately modelled with traditional unsteady corrections for BEM. Since then, researchers have produced numerous numerical studies on FOWTs employing complex high-fidelity methods. A benchmark for this field was the work of Tran and Kim, who used the $k - \omega$ SST model with overset grid for aerodynamic modelling: they started by studying the turbine behaviour under imposed motions [6,7]; then, they coupled the aerodynamics with floater's hydrodynamics by means

of a dynamic fluid body interaction technique [8]. Another example of coupled aero-hydrodynamic CFD-based method was provided by Liu et al. [9]. This kind of studies demonstrated the possibility of conducting high-fidelity multi-physics simulations. Nevertheless, the large amount of complexity included makes the understanding of the flow physics really hard. Moreover, the prohibitive computational cost of these models prevents their concrete use in the design phase. To enhance the aerodynamic comprehension it is necessary to consider simpler models where cause-effect links are clear. Only an improved aerodynamic comprehension allows for improvements in current design tools (Section 1.4).

In parallel to numerical research, there is a strong need for valuable experimental data for codes validation. Unfortunately, the complexity of such floating machines hindered the development of reliable experimental campaigns. In fact, scaled models of floaters and turbines are usually tested separately due to the compelling needs of respecting Froude and Reynolds similarities. Of course, full scale data from currently working FOWTs are property of the sponsor companies, i.e. generally not available to the scientific community. While vast effort is being made to study the floaters dynamics in water basins, wind tunnel tests on FOWTs are scarce. The only remarkable work was made at GVPM within LIFES50+ and UNAFLOW projects. Tests were carried out on a $\varnothing 2.38$m model, featuring imposed surge and pitch motions [10,11]. Furthermore, Politecnico di Milano also developed a 6 D.o.F. pedestal to reproduce the movement induced by the floater. Such system might be used for hardware-in-the-loop (HIL) testing of the turbine model [12]: the wind tunnel measured aerodynamic loads are inputs of an hydrodinamic code which rules the motion of the platform. HIL approach might be a key for future experimental testing since it allows to account for the aero-hydro coupling in wind tunnel tests. This would also solve the conflict between Reynolds and Froude scaling requirements. The main drawback of such approach is the high cost associated.

1.3   Unsteady aerodynamics of wind turbines

The focus of this Thesis is on the aerodynamic part. Two different types of unsteady effects can be distinguished in HAWTs: airfoil unsteadiness and rotor unsteadiness. This separation grounds on the fact that the two phenomena have very different characteristic time scales. Airfoil's unsteadiness occurs at a much

shorter time scale than rotor's. The first, is a well known phenomenon in the aeroelasticity field, since it is common to whatever structure interacting with an airflow; examples might be aircraft wings, helicopter rotors but also civil constructions like bridges. In wind turbines the characteristic time scale for airfoil unsteadiness is $\tau_A = c/W_D$, which is approximately the time required for an air particle to travel from the leading to the trailing edge of the airfoil. Since blade profiles' polars are based on the quasi-static theory, they are valid only as long as the airfoil motion time scale is much larger than τ_A. When this is not the case, different models have to be used to evaluate the aerodynamic forces. Another kind of airfoil unsteadiness typical of wind turbines is the *dynamic stall*. This phenomenon consists of an hysteretic behaviour of the lift coefficient of a profile in its stalled region. The cause is the boundary layer separation and reattachment at the airfoil's suction side, when the AoA changes around the stall value. The flow field redistribution has 'memory' of the past state, thus the B.L. reattachment does not follow the exact inverse path of the separation process. The physics of this phenomenon is really complex, as for all B.L. transition problems. VAWTs architectures are widely affected by this process, owing to the large AoA excursions. To a lower extent, also HAWTs are affected since the roots of the blades might work in the stall region, even under normal operation, to exploit the lift bonus from 3D effects.

Rotor unsteadiness has a characteristic time scale $\tau_R = D/V_0$ [13]. It is immediate to recognize that, in wind turbines, $\tau_R >> \tau_A$ because rotor effects scale with the machine's diameter rather than the chord. This unsteady phenomenon regards only open rotors like wind turbines, helicopters and propellers. In literature it is typically called *dynamic inflow* or *dynamic induction* (rarely also *dynamic wake*). A more detailed description will be given in Section 1.5.

Rigidly fixed onshore/offshore turbines are subjected to all of these unsteady effects during their life. The main sources of unsteadiness fall into three categories:

1. **Wind induced**: wind direction (yaw misalignment); wind speed (gusts); sheared inflow (ABL profile); turbulence.

2. **Controller induced**: pitch actuation (to stall or to feather); rotational speed changes (variable speed rotors/emergency stops).

3. **Machine layout induced**: blade-tower interaction; farm layout (upwind turbine wake effect); blades/tower/shaft vibrations (flexibility).

Floating offshore turbines add a fourth category to those just cited: the floater induced. In fact, the absence of a rigid supporting structure adds six degrees of freedom to the system (or better the stiffness associated to those D.o.F. is much smaller than with rigid substructures). The whole turbine is subjected to surge and sway displacements on the water plane, plus the heave in vertical direction. In addition, there are the three rotations of pitch, roll and yaw as shown in fig.1.3. These movements couple the aerodynamic and hydrodynamic worlds, leading to an increased impact of unsteady effects during normal operation.
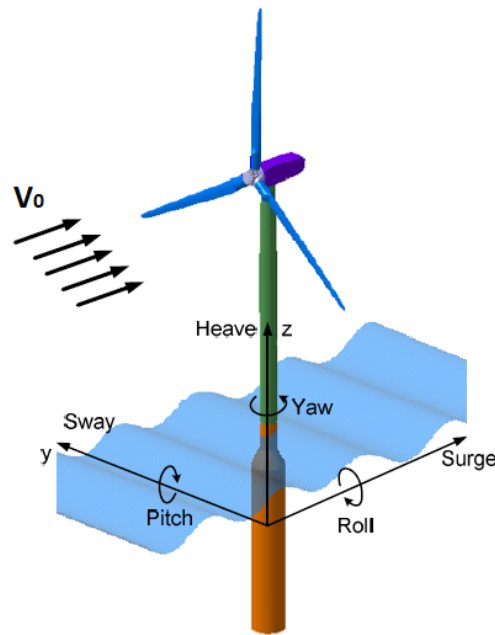
Figure 1.3: FOWT six degrees of freedom. *Source*: Tran and Kim [6]

1.4 Importance of aerodynamic comprehension

The future improvement of wind turbines technology cannot prescind from a better comprehension of all the complex aerodynamic phenomena that occur during their operation. Gaining insight in such mechanisms allows to produce more accurate and general models to be used as design tools. Those currently available have still limited capabilities when it comes to unsteadiness [16].

Even with rapidly increasing computational resources, the need for simple (yet reliable) models is large. To accurately perform a cost estimate indeed, an high accuracy structural model is required; input to that are the aerodynamic forces

that must come from a high-fidelity aerodynamic model. But for the load history to be accurate, also a reliable meteorological model is fundamental. Furthermore, turbines normally operate in farms and they have controllers regulating pitch, yaw and rotational speed. In this outstanding complexity, it becomes evident how the use of CFD will still remain confined to detailed optimisation for a long time. This is why the industries' favourite aerodynamic model for life (i.e. cost) predictions is still the BEM: it can be coupled with several other codes at reasonable computational costs. In the near term though, a progressive shift towards more accurate free wake vortex models is expected. Anyway, the need of sub-models to account for effects that cannot be appropriately captured by the aerodynamic model will always be present. The more these effects are known the more accurate the corrections will be. Each improvement in the chain increases the confidence of the final estimate. Narrower confidence intervals allow for more cost efficient designs, lowering the LCOE. This reasoning holds for all the disciplines involved in the process. However, aerodynamics determines not only the fatigue loads, but also the energy output and the development of the wake in the farm. The latter is of paramount importance to appropriately estimates the loads and performance of downwind turbines. This is what makes the aerodynamic part so important. Of course, narrowing the confidence intervals of meteorological models would be way more effective, but it is difficult to believe it possible on 15-20 years predictions.

With the development of FOWTs, another major source of complexity is added. In this context, a deep aerodynamic knowledge is even more important since the forces will be transferred to the floater and any unforeseen event might result in a catastrophic failure of the system. This poses new challenges to the design of the control system, which must account for the buoyancy of the floater too. For this reason, there is intense research effort in this field (e.g. [17]). Being a new frontier, simple tools for preliminary controller design are also necessary. The empirical models described in Chapters 4 and 5 were developed for such purpose. It is worth to notice that the control strategy has a primary impact on turbine's life and performance. An optimized controller reduces the loads and increases the power output, realizing relevant cost savings. While the margin for improvement in rigidly fixed turbines is small thanks to the long experience, with floating technology it is still relevant. Control strategy improvements may give a strong contribution to floating turbines' LCOE reduction.

1.5 Dynamic Inflow

For a turbine operating in steady-state conditions, there is a direct relation between the thrust/power coefficient and the induction field. This relation is given by the momentum theory, which links rotor's induction to the axial momentum change in the stream tube, leading to: $C_T = 4a(1-a)$; $C_P = 4a(1-a)^2$. Despite its simplicity, the error associated with momentum theory is very small for modern turbines (typically operating with $a \leq 0.35$ and $TSR \geq 6.5$) [18]. The same result can be obtained with the vortex theory, testifying the tight connection between the induction field and the wake development. Therefore, whenever the TSR is fixed, to a certain turbine loading (i.e. C_T) corresponds a certain induction field. In unsteady conditions, though, momentum theory does not hold anymore. For example, assuming that a sudden variation in turbine loading occurs (e.g. because of a fast blade pitch regulation) the induction field will readjust to this change with a time lag. Thus, during the transient there will not be the usual $C_T - a$ correspondence and this will cause relevant load variations with respect to steady-state. The reason for this delay is that the wake development is not immediate: it takes time before the old trailed vorticity is convected downstream and it is replaced by the new one, corresponding to the varied operating conditions (fig.1.4). This induction lag phenomenon is commonly called dynamic inflow or dynamic induction (rarely dynamic wake).
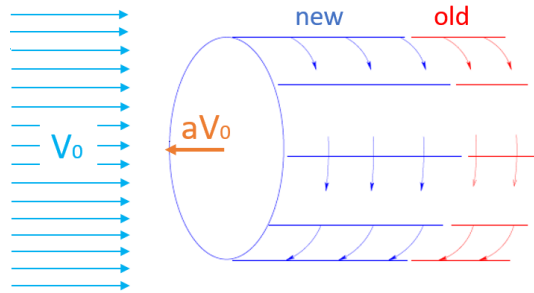
Figure 1.4: wake development and induction field. *Source*: Schepers [13]

Originally, all the studies on non-stationary behaviour of open rotors were focused on helicopters. The first to address the induction lag due to a collective pitch change of a hoovering rotor were Carpenter and Fridovich in 1953 [19]. To model this behaviour they introduced an 'apparent mass' term. Many other studies followed, but the most successful was that of Pitt and Peters (1980) [20], who developed a model that is still implemented in many rotorcraft codes. The

wind turbines unsteady aerodynamics research, instead, started only in the 90's when it was realized that the much higher loading of HAWTs than propelling rotors made the traditional theory poorly effective. A pioneering work in this field was done within the EU program JOULE I: a specific project on dynamic inflow involving several institutions was started in October 1990. At first, pitch step measurements were taken on the 2MW ⌀60m Tjæreborg turbine [21]. Then, additional experiments were performed on a ⌀1.2m scaled model at TUD open jet wind tunnel. In the final project report, by Snel and Schepers [22], several *engineering*[1] models were proposed and tested; the most important were those of ECN and Øye, who are still implemented in several BEM codes. The following milestone for dynamic inflow research was the NREL's NASA Ames wind tunnel test in 2000, featuring a ⌀10m instrumented turbine model. Part of the data concerning dynamic inflow were analysed within the IEA Wind Task 20 [23], giving a greater insight on the flow physics. Meanwhile, the EU MEXICO project was started in 2006. A ⌀4.5m heavily instrumented turbine model was tested in the DNW Large Low-Speed Facility. A huge database was created since also part of the flow field was mapped; the post-processing was made in the first phase of IEA Wind Task 29 - Mexnext [14]. Unfortunately, there were some troubles with instruments calibration and the dynamic inflow part was discarded. From 2007 to 2009 a large number of on-field measurements were taken on two instrumented turbines: a 2MW ⌀80m NM80™and a Siemens 3.6MW. This campaign was part of the DANAERO project, sponsored by the Risø laboratory with several industrial partners. The results were analysed in two phases [24,25] and used for codes validation. In 2012 a New Mexico campaign was funded, fixing the problems of MEXICO experiments. These results were deeply analysed in phase II and III of the IEA Wind Task 29 [15,16]. Phase III was completed in January 2018 and its final report constitutes the current state of the art for wind turbines aerodynamics. A wide experimental-numerical comparison is there reported, concerning both high-fidelity and low-fidelity codes. All codes provide almost perfect match in steady-state conditions, while when unsteadiness is considered relevant discrepancies arise. Even high-fidelity CFD codes demonstrated strong limits in representing those complex phenomena. This witnesses that there is still much to do in aerodynamic research to provide more effective models for

---

[1]the term 'engineering' is meant to indicate that the model is easily included in industrial design codes (BEM) without unduly increasing computational time.

unsteady behaviour.

Since JOULE I conclusion, dynamic inflow effects have remained bounded to sudden load changes, i.e. sudden pitch or rotational speed variations. Several simple models to include the induction lag in BEM codes were proposed. Schepers [13] listed them among others adds-on available, comparing the results of a fully equipped BEM code with Nasa Ames and New Mexico experiments. Traditional dynamic inflow models rely on either one (ECN) or two (e.g. Øye) time constants that rule the exponential behaviour of induction and thrust response. Every attempt of finding a universal formulation to evaluate these constants has failed. The main drawback is that in order to tune the constant properly, the thrust (or torque or flapwise bending moment) response has to be known first. The need for more complete models was highlighted in [16] and then confirmed by Pirrung and Madsen [26]. The latter argue that the partial vision that these models provide could also explain the controversial radial variation of the time constants. In attempt of finding a more reliable and holistic engineering model, Hammam used some analytical solutions for the unsteady actuator disk [27]. More importantly though, he reconsidered the presence of dynamic inflow effects due to wind gusts, separating this case from load changes. He argued that the lack of dynamic inflow effects due to wind gusts observed in JOULE I, was due to a too slow change of wind speed. This redirected the research interest to the dynamic wind case too. Another recent remarkable work was made by Yu [28,29], who proposed an integral-differential formulation based on vortex theory. To validate his model, he performed an experimental study (in the TUD wind tunnel) on a thin disc suddenly changing its porosity. Subsequently, Van Der Deijl [30] tried to extend Yu's model also to the dynamic wind case. Finally, In a recent experimental campaign at the wind tunnel of the University of Oldenburg some dynamic effects due to sinusoidal incoming wind have been observed. Oldenburg's wind tunnel is equipped with an active grid that allows a great freedom in the shaping of the inflow. The tests were conducted on the MoWiTO ⌀1.8m. First they studied the classical dynamic inflow problem with pitch steps [31]; then, they tested the response to an harmonically varying inflow velocity [32]. The corresponding loads oscillations showed a general amplitude reduction with respect to what expected with the quasi-static theory. These new developments in the dynamic inflow field, inspired the investigation described in Chapter 5.

The renewed interest in dynamic inflow ranks perfectly with what discussed in

Section 1.4. Despite the free vortex methods have shown very good performances for loads estimation, it is still necessary to better understand the physics behind this phenomenon. Only a better comprehension can result in models enhancement. An increased awareness on wind gusts and surge effects is a must for accurate load estimation and robust design a FOWT controller.

Chapter 2

UNAFLOW Project Review

The *UNsteady Aerodynamics for FLoating Wind* (UNAFLOW) project started in June 2017 and ended in April 2018. It was a collaborative project belonging to the EU-IRPWIND program, that involved four research institutions: POLIMI, ECN (now TNO), USTUTT and DTU. Its main goal was to investigate the unsteady aerodynamic behaviour of a FOWT under imposed surge motion, comparing wind tunnel tests with high-fidelity simulations results. Detailed information about the project can be found in [11,33]; all the database therein generated is available for download[1]. A thorough description of the wind tunnel campaign conducted in the facility of Politecnico di Milano (GVPM) was provided by Boldrin [34]. The complete tests matrix is reported in Appendix A for reference. In this chapter, the activity performed at GVPM is revised in order to validate the results and verify their quality. In Section 2.1 a brief description of the experimental set up is provided; Section 2.2 shows the inertia subtraction procedure originally followed; Section 2.3 discusses the dynamic amplification effects that pushed the development of the alternative procedure described in Section 2.4. Finally, conclusions are addressed in Section 2.5.

2.1 Tests description

Within the UNAFLOW project, a vast experimental campaign was carried out in the Boundary Layer Test Section of the GVPM. Such section is 13.84m wide x 3.84m high and about 35m long. It was specifically designed for wind engineering

---

[1]The interested reader can send a request to either: simone1.mancini@mail.polimi.it or alberto.zasso@polimi.it

tests structures subjected to atmospheric flow conditions. The wind tunnel is equipped with 14x100KW independently controlled fans, allowing to reach a maximum wind speed of 16 m/s in this test section. The tests were performed in empty inlet configuration (i.e. without roughness elements/turbulence generators), aiming to obtain an inflow velocity profile as constant as possible. The resulting profile (normalized by the value measured at hub height) and turbulence intensity for this configuration are shown in fig.2.1; the wind speed could be considered constant in the rotor zone with a T.I. ∼2%.
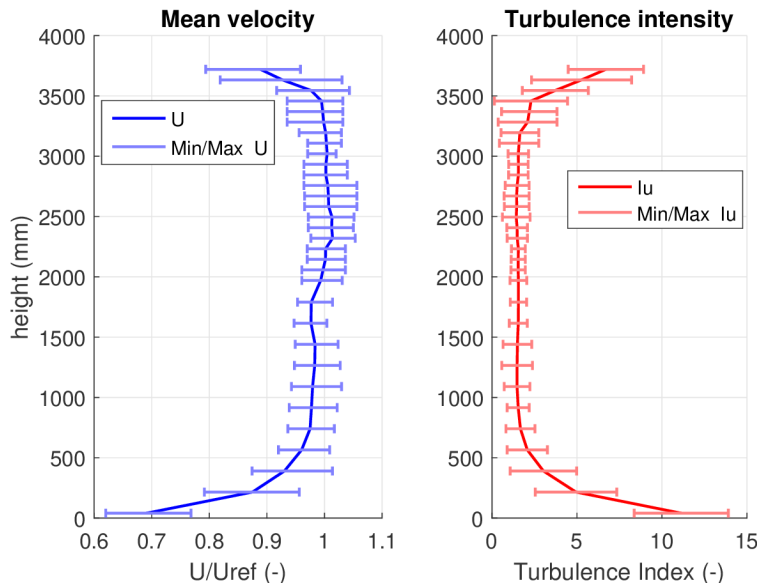
Figure 2.1: normalized wind speed and T.I. profiles with error bars

The turbine tested in the UNAFLOW project was a scaled version (⌀2.38m) of the DTU10MW Reference Wind Turbine [35]. The model was completely designed by Politecnico di Milano within the LIFES50+ project in 2015 [36]. The main objective of the design was to properly match the aerodynamic loads of the reference turbine, especially the thrust force which rules the dynamics of a FOWT. The scale of 1/75 was chosen to maximize the model size (i.e. to reduce Re mismatch), keeping the blockage factor below 10%. The wind velocity was scaled of a factor 3; this led to a Reynolds number 225 times lower than reality, forcing the use of a low Re profile (SD7032). To fulfill the loads compliance with a different profile, also the chord and twist distributions were changed. Finally, the thickness was chosen to place the first blade flapwise mode around 20Hz as for DTU10MW. The only difference with respect to LIFES50+ was

that, in UNAFLOW, a stiffer aluminum tower was employed to reduce dynamic amplification effects (Section 2.3). Fig.2.2a shows the scaled model inside the test section.

(a) Experimental setup

(b) Schematic sketch and reference system
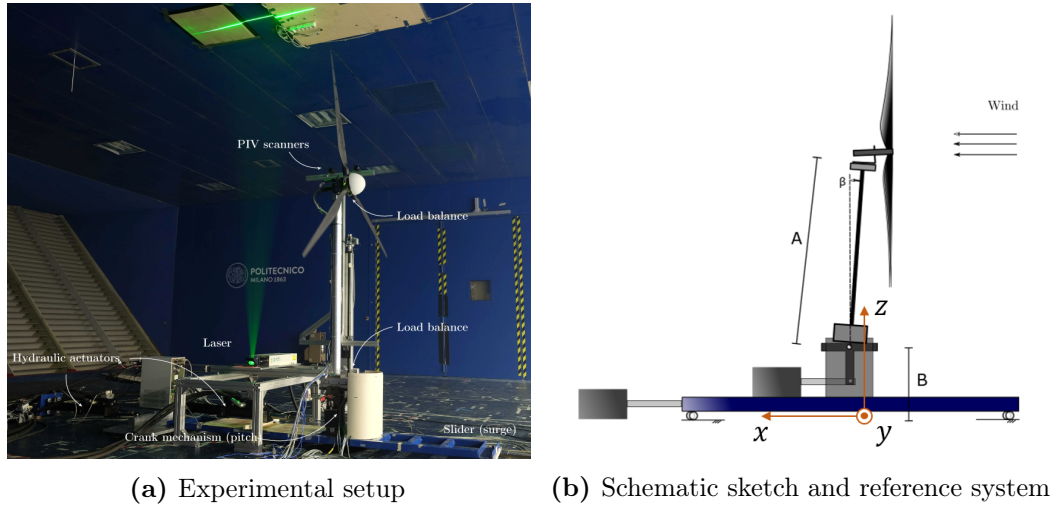
Figure 2.2: scaled model experimental setup

The turbine was mounted on a slider, commanded by means of an hydraulic actuator to produce the desired surge motion (fig.2.2 and 2.3). Furthermore, another hydraulic piston was connected to a slider-crank mechanism, located underneath the tower, that allowed to govern the turbine's pitch too. However, this feature was not exploited in the UNAFLOW project and the mechanism was only used to place the rotor perpendicular to the inflow, i.e. cancelling the 5° design tilt angle. This choice was made to simplify the aerodynamics avoiding periodic effects due to the rotor tilt.

(a) Surge piston

(b) Pitch piston
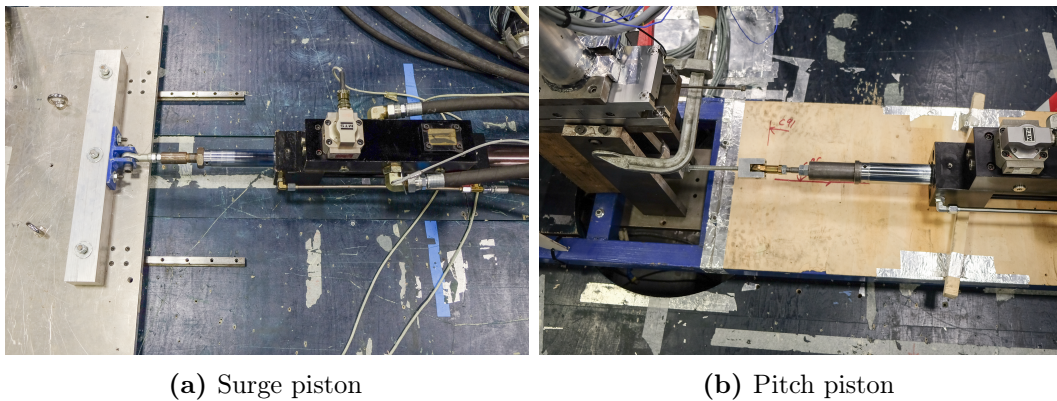
Figure 2.3: surge and pitch actuators

A wide array of sensors was employed, for measuring both the model's dynamic response and the near wake flow field downstream the turbine. All the instruments were synchronized and everyone sampled at 2KHz. The shaft was equipped with a proximitor, for angular position, and an encoder to measure the turbine's rotational speed. Two six-components balances were mounted respectively at the nacelle (ATI) and at the tower base (RUAG), as shown in fig. 2.4. A couple of accelerometers was placed right next to each balance: at the base they measured along surge and heave directions (x,z according to fig. 2.2); at the nacelle along surge and sway (x,y). To measure the base surge position, both an LVDT and a laser transducer were used. The first was only exploited to synchronize signals from different tests for the inertia subtraction (Section 2.2), due to its high precision but slow response (phase lag); the laser, instead, was chosen as surge reference signal. The reference system for all the analysis is shown in fig.2.2; note that the surge (x) direction has the same versus of the wind speed.

(a) Nacelle instruments   (b) Base instruments
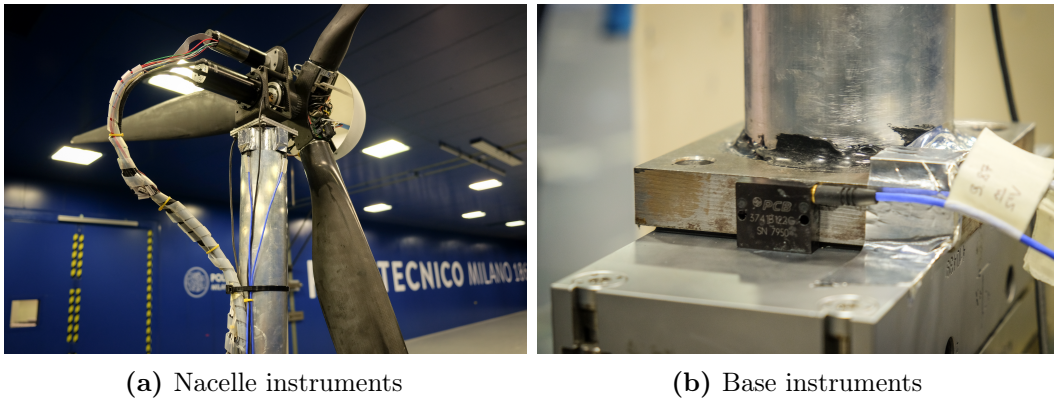
Figure 2.4: nacelle and base balances and accelerometers

For what concerns the flow field, the incoming wind speed was measured 5m upstream the turbine at a height of 1.5m. Moreover, the wake x and z velocity components on vertical plane behind the turbine were extracted with a PIV technique. The system comprised two synchronized 2Mpx cameras mounted on an automatic traversing system for vertical displacement. These cameras were connected with an Nd:Yag double pulsed laser (200 mJ). The pictures of the particle-seeded flow, enlightened by the laser (see fig. 2.2), were post-processed by a PIVview 3C by PIVTEC to recreate the two-dimensional velocity vector. These measures are not of considered in this Thesis, but a nice analysis of the main PIV results can be found in [37].

Tests were carried out at three different wind speeds and grouped accordingly, as reported in tab.2.1. The groups RATED1 and 2 represent tests conducted at two different wind velocities but both at optimal TSR (variable speed rotor). Conversely, ABOVE group is at above-rated conditions, i.e. higher wind speed and lower TSR. For each of these groups, both steady and unsteady turbine cases were considered (ref. Appendix A). As anticipated, for the unsteady tests a sinusoidal surge motion was imposed. Different surge frequencies representative of the sea spectrum were selected, recalling that the scaling process made the real-scale frequencies 25 times smaller than in tests. For each frequency, displacement amplitudes were chosen to have a maximum of the surge velocity signal at (5,3.75,2.5,1.25)% of the undisturbed velocity.

Name	Wind speed $[m/s]$	Rotor speed $[rpm]$	TSR $[-]$	ϑ_p $[°]$
RATED1	2.42	150.3	7.4	0
RATED2	4.0	242.2	7.5	0
ABOVE	6.1	265.8	5.5	12.5

Table 2.1: operating conditions tested UNAFLOW

2.2   Original inertia subtraction procedure

Imposing a motion to the turbine made the experimental evaluation of the aerodynamic thrust not straightforward. Indeed, the balances committed to the purpose also measured a relevant inertial contribution due to the surge acceleration. Increasing the surge frequency, this term became much larger than the aerodynamic one. Therefore, a lot of care had to be taken in removing inertial loads to correctly estimate the thrust force. This process will be referred to as *inertia subtraction procedure*. The strategy followed in the UNAFLOW project was inherited from LIFES50+ campaign and it is described hereinafter. For more details the reader can refer to [34].

To perform the inertia subtraction, each surge test was repeated without wind and with the rotor steady. This class of tests was called NOW (NO-Wind), whilst standard tests were called SIW. Because of some troubles with the calibration of the RUAG balance at the base of the turbine, only the signal of the ATI balance

(at the nacelle) was used. Its force measure along the x axis was:

$$-F_{NOW}^{ATI} = -m\ddot{x}_{NOW} \; ; \tag{2.1}$$

$$-F_{SIW}^{ATI} = -m\ddot{x}_{SIW} + T \; ; \tag{2.2}$$

the '−' sign ahead F_{NOW}^{ATI} was due to the opposite versus of x in the balance's reference system; the term m comprehended rotor, hub and nacelle masses. The inertia subtraction procedure strongly relied on the fact that the system could be assumed perfectly rigid. This hypothesis could be considered accurate as long as the surge frequency was far from the first vibration mode of the system, i.e. the tower's cantilever bending mode. This fact had caused problems in LIFES50+ measurements which were affected by dynamic effects, as discussed in Section 2.3. For this reason, in the UNAFLOW campaign a stiffer tower was employed, shifting the resonance from ∼4.2Hz to ∼6.5Hz. For what concerns the blades, their first flapwise bending mode was above 20Hz; thus, in the frequency range of interest, the rotor could be assumed rigid without consequences. For the rigid body hypothesis, nacelle's displacement was coincident with the one of the base, imposed by the surge actuator. Thus in complex notation:

$$x = A_s \, e^{\mathbf{i} \, 2\pi f_s \, t} \; ; \tag{2.3}$$

$$\dot{x} = \mathbf{i} \, 2\pi f_s \, A_s \, e^{\mathbf{i} \, 2\pi f_s \, t} \; ; \tag{2.4}$$

$$\ddot{x} = -(2\pi f_s)^2 A_s \, e^{\mathbf{i} \, 2\pi f_s \, t} \; . \tag{2.5}$$

Since eq.2.5 holds both for SIW and NOW tests, the thrust force could be obtained simply subtracting eq.2.1 to eq.2.2. Hence:

$$T = F_{NOW}^{ATI} - F_{SIW}^{ATI} \; . \tag{2.6}$$

Therefore, the aerodynamic force was obtained comparing the SIW and NOW measures of the ATI balance in the axial direction. In order to perform this operation the two signals had to be synchronised first, since they came from different tests. The reference signal chosen for the synchronization was the LVDT's. First, only the surge frequency component was taken to have a cleaner measure, even though the actuation quality was remarkable. Then, an integer number of surge periods were extracted (to avoid leakage) by counting the zero-crossing points of the mono-harmonic signal. Once the interesting part was withdrawn

from each test, the inertia subtraction could be finalised and the thrust force obtained. Finally, the oscillating part of the signal was considered subtracting its mean value. Once again, only the surge harmonic was considered and the equivalent aerodynamic coefficients could be calculated:

$$(T - T_0)|_{@f_s} = |\Delta T| \, e^{\mathbf{i}(2\pi f_s \, t + \phi)} = (|\Delta T| \cos \phi + \mathbf{i} \, |\Delta T| \sin \phi) \, e^{\mathbf{i} \, 2\pi f_s \, t} =$$
$$= - \, m_{aero} \, \ddot{x} - c_{aero} \, \dot{x} = (m_{aero} \, (2\pi f_s)^2 A_s - \mathbf{i} \, c_{aero} \, 2\pi f_s \, A_s) \, e^{\mathbf{i} \, 2\pi f_s \, t} \; ;$$

considering real and imaginary parts separately:

$$c_{aero} = - \frac{|\Delta T| \sin \phi}{2\pi f_s \, A_s} \; ; \qquad\qquad (2.7)$$

$$m_{aero} = \frac{|\Delta T| \cos \phi}{(2\pi f_s)^2 A_s} \; . \qquad\qquad (2.8)$$

2.3 Dynamic amplification effect

The rigid system is a good approximation as long as $f_s << f_I$. Since the maximum surge frequency tested was of 2Hz, in LIFES50+ campaign a tower with first mode at ∼4.2Hz was deemed definitely suitable. Though, the results obtained from the inertia subtraction procedure, shown in fig.2.8 at the end of this Section, proved this assumption to be wrong. A frequency margin like that would have been perfect for any civil engineering structure, but not for a wind turbine. In fact, a drastic increase of $|\Delta T|$ with the surge frequency was observed [38], in evident contrast with the quasi-static theory. At first, it was thought that this might had been caused by some dynamic inflow effects but then, a concern arose on the steepness of such increase and the energy content related to it. Since the structure's inertial contribution was the largest involved, it could likely provide that amount of energy. Furthermore, the sharp increase with frequency resembled more a solid-mechanics' problem rather than a fluid-dynamic one. The use of a stiffer tower in the UNAFLOW campaign confirmed latter hypothesis. Results for the thrust oscillation showed a much better agreement with the quasi-static theory. The reason behind LIFES50+ behaviour was the significant amount of aerodynamic damping characterizing SIW tests. There the rigid body assumption was not accurate and the results of the inertia subtraction procedure were altered by a dynamic amplification effect, as described in the following.

If tower's flexibility is accounted, in the frequency range of interest the turbine can be modelled as a simple 1 D.o.F. system (fig.2.5), considering that the base displacement is imposed. Having dumped the rigid body assumption, nacelle's
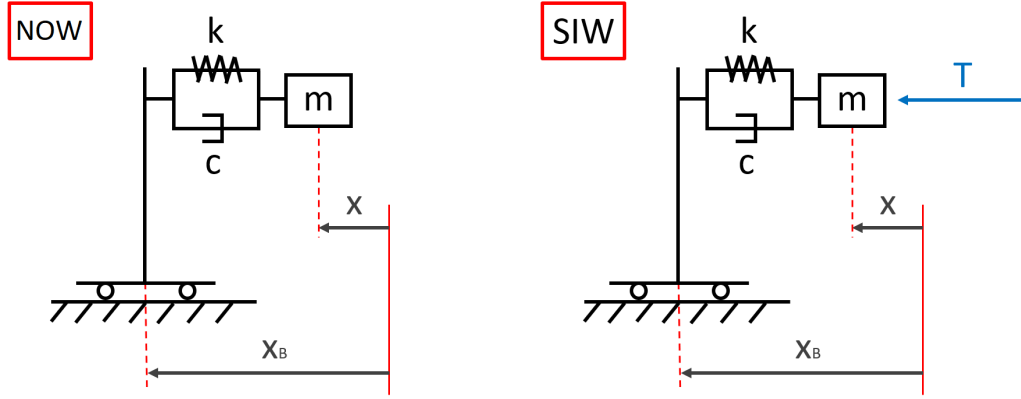
Figure 2.5: turbine's equivalent 1 D.o.F. systems (x_B imposed)

displacement is not coincident with the basis' one anymore. Then, the dynamics in the NOW case is given by:

$$m\,\ddot{x}_{NOW} + c_{str}\,\dot{x}_{NOW} + k\,x_{NOW} = c_{str}\,\dot{x}_B + k\,x_B \; ; \tag{2.9}$$

$$x_{NOW} = \frac{k + \mathbf{i}\,2\pi f_s\,c_{str}}{-(2\pi f_s)^2\,m + \mathbf{i}\,2\pi f_s\,c_{str} + k}\,x_B \; ; \tag{2.10}$$

with $x_B = A_s\,e^{\mathbf{i}\,2\pi f_s\,t}$ and having assumed zero initial conditions. When the wind is active and the rotor is operating instead, the aerodynamic thrust force appears in the equation of motion. Hence, for the SIW case:

$$m\,\ddot{x}_{SIW} + c_{str}\,\dot{x}_{SIW} + k\,x_{SIW} = c_{str}\,\dot{x}_B + k\,x_B + T; \tag{2.11}$$

with $x_B = A_s\,e^{\mathbf{i}\,2\pi f_s\,t}$. Then, eq.2.11 can be linearized for $A_s \to 0$ and the oscillating thrust contribution expressed in terms of equivalent aerodynamic damping (the mass contribution is negligible in this frequency range). The equilibrium equation becomes:

$$m\,\ddot{x}_{NOW} + (c_{str} + c_{aero})\,\dot{x}_{NOW} + k\,x_{NOW} = c_{str}\,\dot{x}_B + k\,x_B \; ; \tag{2.12}$$

$$x_{SIW} = \frac{k + \mathbf{i}\,2\pi f_s\,c_{str}}{-(2\pi f_s)^2\,m + \mathbf{i}\,2\pi f_s\,(c_{str} + c_{aero}) + k}\,x_B \; ; \tag{2.13}$$

again assuming same imposed x_B and null initial conditions. The responses of the two cases are shown in fig.2.6. The numbers used for the plots aimed at
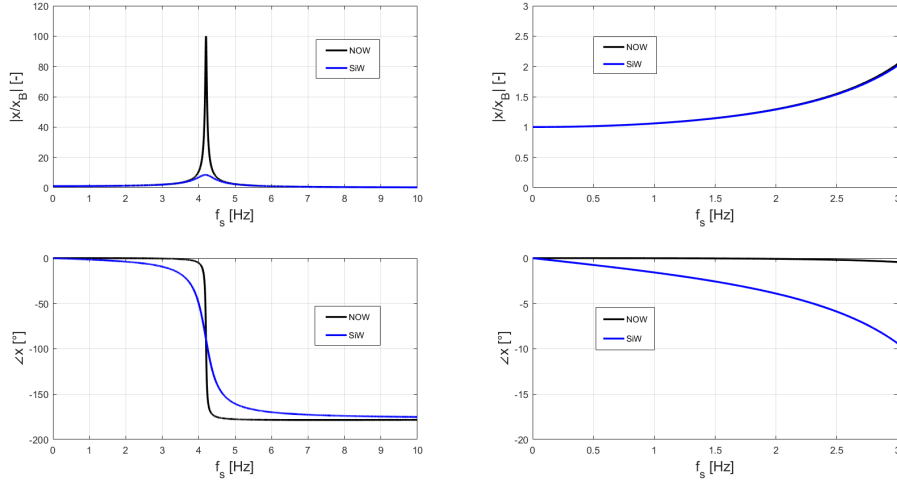
Figure 2.6: 1 D.o.F. systems' FRFs: modulus (up) and phase (bottom); broad view on the left, interesting range zoom on the right

reproducing RATED2 conditions of LIFES50+, having only guessed a structural non-dimensional damping of 5‰. Its effect on the frequency response functions was little in the interval 0-10Hz. Despite the maximum surge frequency was less than half of the resonance one, a $\psi \approx 5^o$ phase difference between NOW and SIW was present. In NOW conditions the rigid body assumption was consistent except for a small amplitude increase at the nacelle with respect to the base. The high aerodynamic damping of the second case delayed the phase already at 2Hz, whereas the influence on the modulus was none. This phase shift produced a biased estimate for the thrust oscillation if the inertia subtraction was performed according to Section 2.2. The reason is that when eq.2.1 is subtracted from eq.2.2, the inertial force terms do not cancel each other out because the signals are shifted in phase.

The phasors representation in the Gauss plane is reported in fig.2.7. Therein, the real aerodynamic thrust force oscillation is indicated as ΔT whilst the measured one as ΔT_{meas}. It is clear how the measured force has a higher amplitude than the real one, because of the inertial contribution; the greater the phase shift, the larger the amplitude difference. This results in an overestimation (as absolute values) of both c_{aero} and m_{aero} and, to a lower extent, a variation of ϕ (see the black box in fig.2.7). By the way, it is important to notice that while
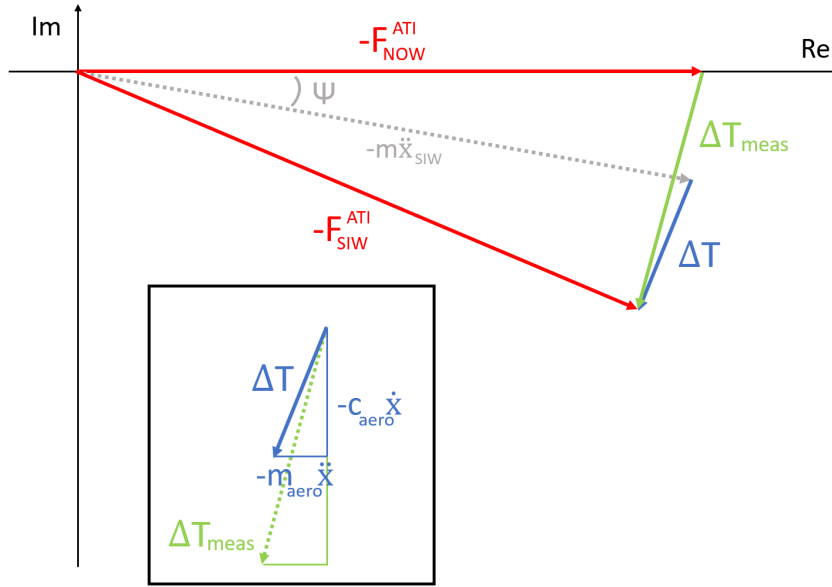
Figure 2.7: complex representation of the dynamic amplification effect; a zoom on the real and measured thrust oscillation phasors is shown in the box

the influence on the amplitude is univocal, the sign of the phase change depends both on ψ and on the real phase of the thrust (ϕ). In formulas:

$$\Delta T_{meas} - \Delta T = m \left(\ddot{x}_{NOW} - \ddot{x}_{SIW} \right) = m \, \ddot{x}_{NOW} \left(e^{-\mathbf{i}\,\psi} - 1 \right). \qquad (2.14)$$

The difference between measured and actual value is made of two factors: the first is the inertia force in NOW conditions, i.e. quadratically increasing with f_s; the second term depends on the phase shift ψ, also increasing with f_s in a non-linear way. The presence of this discrepancy could be clearly seen if LIFES50+ and UNAFLOW results, with that inertia subtraction procedure, were compared to the quasi-static theory predictions (fig2.8). The simple quasi-static model will be described in detail in Chapter 4. For now it is enough to anticipate that it models the aerodynamic damping coefficient as a constant which depends only on the steady turbine's operating conditions. This model has been shown in very good agreement with revised UNAFLOW results (Section 2.4), CFD and AL simulations (Chapter 4). In fig.2.8 the plots of the ratio between the thrust oscillation amplitude and the surge amplitude, for the three different operating conditions, are shown as a function of the surge frequency. This choice was made to have a clear reference since the quasi-static model foresees a linear behaviour:

$|\Delta T|/A_s = c_{aero}\, 2\pi f_s$, with $c_{aero} = c_0$ constant. The different slopes between UNAFLOW and LIFES50+ are due to slightly different test conditions (tab.2.1 and 2.2). It is also important to point out that in ABOVE conditions, due to pitch regulation, c_{aero} could not be evaluated from eq.4.13 (Chapter 4). Therefore, its values were estimated from the lowest frequency tests.
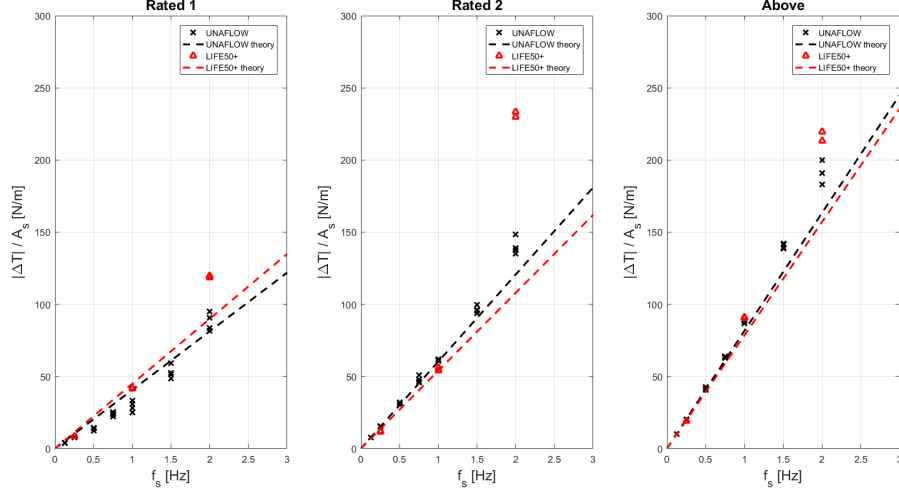
Figure 2.8: $|\Delta T|/A_s$ comparison among LIFES50+, UNAFLOW and quasi-static model for different conditions

Looking at fig.2.8, the dynamic amplification effect is clearly visible in LIFES50+ results. At low frequency the agreement was good, but towards 2Hz the amplitude became much larger. This behaviour was also accentuated by the fact that A_s referred to the base surge displacement imposed, not considering the amplification at the nacelle. The stiffer tower of the UNAFLOW campaign reduced such effect. Although, it was still possible to notice a slight influence at the maximum surge frequency. This evidence pushed the will of seeking a more accurate way to perform the inertia subtraction.

Name	Wind speed $[m/s]$	Rotor speed $[rpm]$	TSR $[-]$	ϑ_p $[°]$
RATED1	2.33	150	8	0
RATED2	3.67	221	7.5	0
ABOVE	5.33	239.5	5.6	12.5

Table 2.2: operating conditions tested LIFES50+

2.4   New inertia subtraction procedure

For the purpose of validating the wind tunnel tests of the UNAFLOW campaign, a new inertia subtraction procedure was developed. Such procedure was designed to avoid the previously discussed dynamic amplification effect, so as to remove any unwanted bias from the thrust measurement. The heart of this procedure was the accelerometer placed at the nacelle. In fact, it was used to evaluate the inertial term in eq.2.2 which could, then, be removed from the ATI balance's SIW signal to get the aerodynamic thrust. With this new approach, the NOW tests became only useful for precisely estimating the mass attached to the balance (m). To do so, the harmonic components at the surge frequency of both $-F_{NOW}^{ATI}$ and ACC_{NOW} ($\equiv \ddot{x}_{NOW}$) signals were extracted. Thus, the simple comparison of the two amplitudes allowed to estimate the mass for any surge case considered:

$$m = \frac{|F_{NOW}^{ATI}|_{@f_s}}{|ACC_{NOW}|_{@f_s}} \; . \tag{2.15}$$

To avoid leakage problems, the test's signals were cut in order to consider always six full surge periods, i.e. taking a number of samples $N_s = 6 * f_{samp}/f_s$. An alternative way might have been to directly divide the balance's signal by the accelerometer's one, obtaining a slightly time-variant estimate $m(t)$ whose average value could have been used as m. The first approach was preferred for better accuracy, since the comparison among signals from different instruments could be affected by their relative delay. Nevertheless, the difference between these two methods was verified negligible.

Once the value of m was estimated, the aerodynamic thrust force could be easily obtained from the SIW measurements:

$$T = -F_{SIW}^{ATI} + m \, ACC_{SIW} \; ; \tag{2.16}$$

provided that $ACC_{SIW} = \ddot{x}_{SIW}$. Also in this case, the component at the surge frequency was considered, and the equivalent aerodynamic coefficients (c_{aero} and m_{aero}) could be computed from $|\Delta T|$ and ϕ. This time though, there were two alternative ways to set the phase reference of the signal. Indeed, the accelerometer on top provided an indirect measure of the surge displacement at the nacelle: $x = -ACC_{SIW}/(2\pi f_s)^2$ (considering only the surge harmonic). Due to dynamic amplification, this signal had a slightly different amplitude and a phase shift of

ψ with respect to the base imposed displacement (eq.2.10 and 2.13, plotted in fig.2.6). Therefore, the values of aerodynamic damping and mass coefficients depended on the phase reference chosen, as shown in fig.2.9. The phasoric representation allows to recognize the difference between nacelle's displacement (from accelerometer) and the base one (from laser); note that such difference was dramatically enlarged for visualisation purposes. It is clear how the angle ψ modifies the components of ΔT depending on the reference chosen. In principle,
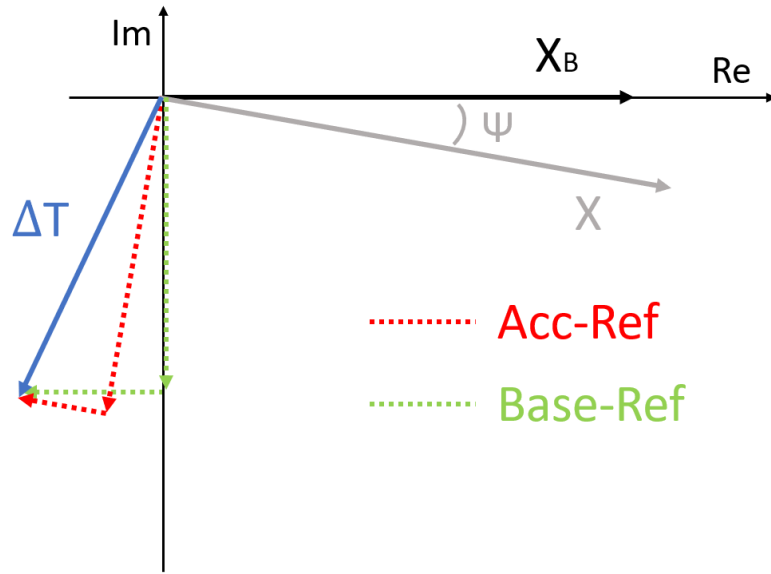
Figure 2.9: complex representation of the dynamic amplification effect; a zoom on the real and measured thrust oscillation phasors is shown in the box

the correct choice would be to use the accelerometer-derived signal (x) since it refers to the real rotor displacement. Nevertheless, the accelerometer signal was characterized by a much larger uncertainty, not only because of the lower instrument's accuracy. Acceleration measures are always more affected by high-frequency noise than position ones. Furthermore, being the instrument close to the rotor there were many sources of disturbances, from aerodynamic noise to rotor vibrations. Whenever this signal was used as reference, the term A_s in expressions 2.7 and 2.8 was substituted by $|x|$ and the phase of the thrust (ϕ) had to be referred to $\angle x$ (rather than $\angle x_B$). The base displacement instead, was not directly linked to the turbine's aerodynamics but it had the advantage to be a very accurate measurement. In addition, its surge harmonic content was known a-priori being imposed as an input of the test.

The very stiff tower used in the UNAFLOW campaign, limited the effect of

dynamic amplification. Hence, the choice of the reference made little difference on the results. The comparison in terms of thrust oscillation amplitude and phase is reported in fig.2.10 and 2.11 respectively. Also the original inertia subtraction results have been included in the comparison. For what concerns the amplitude,
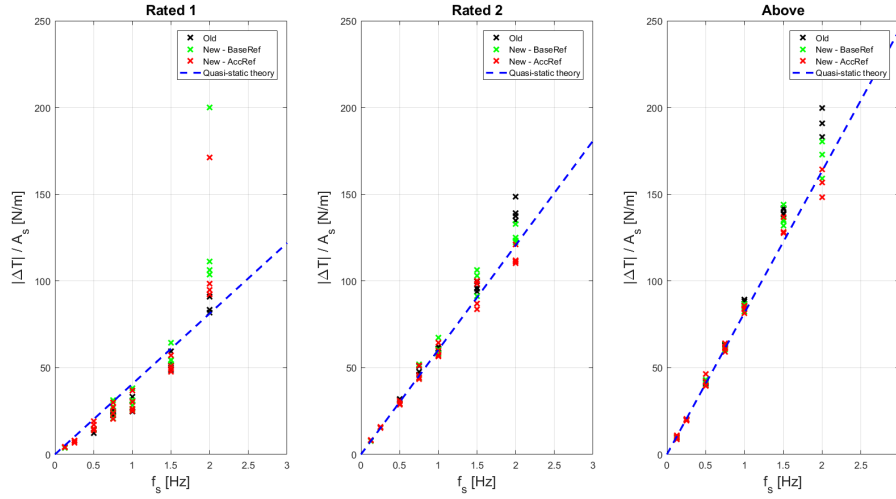
Figure 2.10: $|\Delta T|/A_s$ comparison among different inertia subtraction procedures for UNAFLOW campaign

despite the differences were quite small, the effects of the various choices could be recognized. First of all, at low frequency all the methods provided the same results confirming that new inertia subtraction techniques were implemented successfully. In the tests above 1Hz, the new approach prevented the amplitude increase due to dynamic amplification. Selecting the laser signal as reference, the bias due to ψ was cancelled. Although, the effect of dividing by the base surge amplitude A_s instead of the actual one (at the nacelle) remained. Conversely, choosing the accelerometer as reference also the latter was avoided, explaining why red crosses stay below green ones at $f_s > 1$Hz (fig.2.10). The exceptions found in RATED1 conditions could be attributed to the low signal-to-noise ratio of those tests, which hindered the quality of accelerometer's measures. Such aspect represents a major drawback of the new method proposed (Section 2.5).

Looking at the phase of the thrust oscillation in fig.2.11, it is soon noticed that the scatter is grater than for the amplitude. Again, this was particularly true for tests with low ΔV where the signal-noise ratio was poor. Difficulties in the precise phase estimation were not surprising though. The size of T was much smaller than the inertial part, thus a small amplitude error in the latter
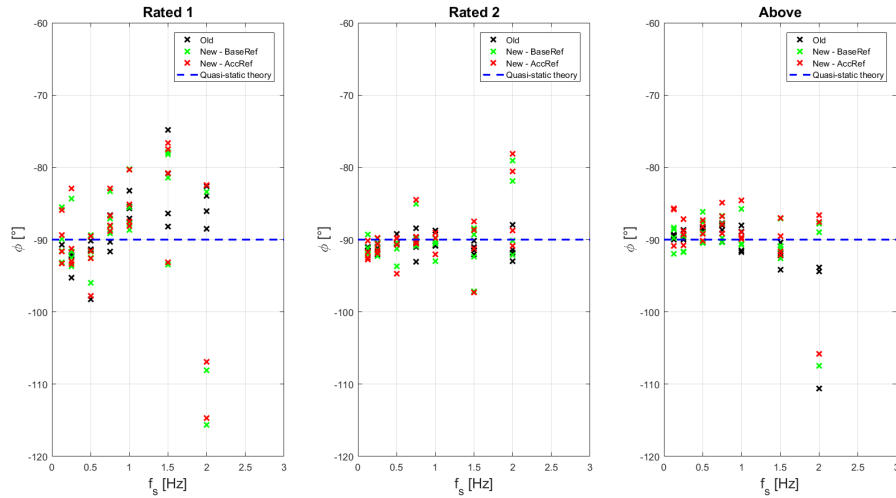
Figure 2.11: phase comparison among different inertia subtraction procedures for UNAFLOW campaign

produced a significant phase variation for ΔT. In this context, ACC-reference results presented a slightly higher variance than BASE-reference. Anyway, the ϕ samples could be well approximated by a Gaussian distribution around -90°, denoting the scatter to be likely induced by stochastic measurement error.

2.5 Conclusions

The alternative inertia subtraction procedure proposed has demonstrated to improve the quality of the results. The main advantage of the new approach, especially if the accelerometer is also chosen as phase reference, is the complete removal of the dynamic amplification bias. Thus, in the UNAFLOW project review, it was possible to clean wind tunnel results providing a reference for quantitative assessment of tower's flexibility impact. The comparison between new and old procedure for the UNAFLOW campaign confirmed the beneficial effect of a stiffer tower than LIFES50+. The difference among the methods was recognizable but limited, thus the rigid body assumption could still give acceptable results in the frequency range considered. The proposed technique would be even more useful for cleaning LIFES50+ results, which were heavily affected by the tower's dynamics. Such review was out of the scope of this Thesis, but it might be a cue for further validation of this new approach.

Besides the great advantage of removing dynamic effects, such procedure

entails two main drawbacks. As shown by RATED1 results of UNAFLOW, the use of accelerometers cannot prescind from a high signal-to-noise ratio to give reliable results; if this was not the case, it would be preferable to adopt the old method. Moreover, the new technique relies on the subtraction of two signals (eq.2.16) coming from different instruments, i.e. load balance and accelerometer. Therefore, great care has to be taken to verify the absence of delay between the two measurements, otherwise it would have to be compensated by re-phasing the signals. This involves a demanding effort for accurate instruments set up and calibration.

In conclusion, if the system is stiff enough to be assumed rigid, the traditional approach is the most suitable for its simplicity and robustness. Nevertheless, the high aerodynamic damping of the SIW case requires an extremely rigid (i.e. expensive) tower to achieve that. The alternative proposed allows to obtain accurate results at lower costs. For the sake of completeness, there might be also another way to perform the inertia subtraction. Indeed, the very good match provided by the quasi-static model (Chapter 4) would allow for a good initial estimate of c_{aero}. If also an accurate modal analysis of the tower was performed, the two things together would fully characterize the mechanical systems of fig.2.5. This would allow to avoid the need of nacelle's accelerometer, since $\ddot{x}_{SIW}$ could be obtained simply deriving eq.2.13 twice and used for the inertia subtraction. This would give an estimate of the thrust force oscillation from which a new value of c_{aero} can be computed. The latter can be used as input for the next iteration until convergence is reached on ΔT. A similar iterative procedure might be followed also if an m_{aero} term was present, provided that its contribution was accounted in the equation of the dynamics.

Chapter 3

Actuator Line Simulations Setup

For the numerical study of the unsteady aerodynamics of FOWTs, an Actuator Line (AL) model was chosen. In particular, the MECC's (Polimi) in-house developed code was used, owing to the long history of validation. Such code differs a little from commercial softwares because it relies on the Effective Velocity Model (EVM) proposed by Schito [39]; this technique was implemented in OpenFOAM by Bernini and Caccialanza [40]. Luca Bernini also programmed the possibility to assign a sinusoidal surge motion to the rotor and to freely impose the blades pitch time history. In this Chapter, a brief description of the AL technique is first given in Section 3.1; then, Section 3.2 provides an overview of the code used and the reasons for its selection; the complete list of settings employed to perform the CFD simulations is discussed in Section 3.3; finally, the mesh sensitivity analysis is reported in Section 3.4, while Section 3.5 presents the final considerations.

3.1 The Actuator Line model

The different scales characterizing wind turbines operation make the full CFD modelling of these machines an extremely demanding task. Indeed, the size of the rotor requires a domain cross-section of the order of $\sim 10^2 \text{x} 10^2 \text{m}^2$. Moreover, the need of imposing undisturbed conditions at inlet and far wake conditions at outlet, constraints the streamwise dimension to several rotor diameters. At this scale the induction field is determined. Conversely, the blades aerodynamics is ruled by the profiles lift generation which cannot prescind from an accurate reproduction of the boundary layer. This leads to very strict y^+ requirements that depend on the approach chosen to model turbulence and B.L.; in the simplest case, i.e.

solving RANS with a high-Re wall function, the characteristic cell size would be of $\sim 10^{-2}$m on the blade surface. In reality to get accurate results at least a $k-\omega$SST model with low-Re wall functions has to be used, pushing the smallest cell size down of one or two orders of magnitude. Then, the stability condition imposes a time step proportional to the smallest element of the mesh. All these aspects together make the computational cost of a full scale simulation prohibitive, even with modern HPC clusters. Furthermore, it was demonstrated that the accuracy of such simulations in complex conditions (e.g. unsteady aerodynamics) is still quite limited [16].

Nevertheless, the necessity of assessing the performances of turbines in farms, in order to optimize the array configuration, forced the development of intermediate models between BEM and pure CFD. At present, the three most popular alternatives are: the Free Vortex Wake method, the Actuator Disk and Actuator Line models. The first is based on the potential (i.e. inviscid) flow and cylindrical wake assumptions. It treats the blade as a lifting line, whose bound vorticity is calculated from the lift force with the Kutta-Joukowski theorem. The trailed and tip vortex lines convecting downstream model the wake. The knowledge of the undisturbed wind profile and the blades airfoil's polar data is required. The induction field is evaluated from the wake vorticity by means of the Biot-Savart law. This model provides substantial improvements in unsteady operations with respect to BEM, at a limited computational cost increase. For this reason it is likely to become the industry standard for life predictions in the medium term. Although, it has serious limitations when it comes to wind farm aerodynamics: it is very hard to model inflow turbulence, the flow is considered inviscid and wake expansion is neglected. Such aspects are of outmost importance for farms performance predictions. With this purpose Sørensen proposed the Actuator Disk (AD) method first [41], and the Actuator Line (AL) then [42]. Both the models are based on CFD, but they solve the problem of scales difference by replacing the turbine with either a disk or lines in which the aerodynamic forces are generated. This way the boundary layer modelling is avoided and most of the computational cost is saved. This allows to perform high fidelity LES (or DES if ground's boundary layer is accounted) simulations that guarantee an accurate reproduction of the wake evolution [43,44,47]. Since the forces at each spanwise section are distributed evenly on the annulus, the AD method cannot capture the influence of tip vortices without implementing a correction. Furthermore, the azimuthal

average makes it only valid for symmetric inflow conditions. The AL method instead, accounts for the finite number of blades adding just little complication to the model. A further evolution, called Actuator Surface, in which the blade forces are distributed along the chord to reproduce the airfoil pressure distribution, was proposed by Shen et al. [46]. Anyway, its popularity remained limited owing to the complexity of generating curve fits to airfoil pressure distributions over the range of angle of attack. Therefore, for the development of this Thesis, the Actuator Line was deemed the best trade-off between accuracy and computational cost to study the unsteady turbine's aerodynamics.

Both AD and AL models are based on the addition of a source term $\mathbf{f}(\mathbf{x}, t)$ to the momentum equation. Implying the time and space dependency of the variables, the Navier-Stokes system for the incompressible case becomes:

$$\nabla \cdot \mathbf{u} = 0 \; ; \tag{3.1}$$

$$\rho \, \frac{\partial \mathbf{u}}{\partial t} + \rho \, (\mathbf{u} \cdot \nabla) \, \mathbf{u} + \mathbf{f} = \rho \, \mathbf{f}_V - \nabla p + \mu \nabla^2 \mathbf{u} \; . \tag{3.2}$$

In the Actuator Line method, at each time step $\mathbf{f}$ is evaluated dividing the blade line in multiple segments according to mesh intersections (fig.3.1a); each one of them is studied as a 2-dimensional airfoil just like in BEM codes. To avoid wiggles in the numerical solution (i.e. unphysical oscillations), the aerodynamic force of the blade segment is smeared among neighbouring cells rather than applied to the nearest cell center (fig.3.1b). This is done by a convolution with the so-called *Regularization Kernel* function, typically a bi-variate normal distribution (2D) as suggested by Mikkelsen [44]. Hence:

$$\mathbf{f} = \eta_{RK} \otimes \frac{\mathbf{L} + \mathbf{D}}{V_{cell}} \; ; \tag{3.3}$$

$$\eta_{RK}(\varepsilon, d) = \frac{1}{2\pi\varepsilon^2} \, \exp\left(-\frac{d^2}{2\varepsilon^2}\right) \; ; \tag{3.4}$$

$$\mathbf{L} = \frac{1}{2} \, \rho c h \, C_L(\alpha) \, W_D^2 \, \hat{\mathbf{u}}_L \; ; \tag{3.5}$$

$$\mathbf{D} = \frac{1}{2} \, \rho c h \, C_D(\alpha) \, W_D^2 \, \hat{\mathbf{u}}_D \; ; \tag{3.6}$$

with d being the distance between the considered cell center and the central one (where the grid intersection is); whilst h is the spanwise length of the segment considered, e.g. $\overline{ab}$, $\overline{bc}$, etc... in fig.3.1a. Lift and drag forces are directly calculated

(a) Segments generation by mesh intersections

(b) Regularization kernel
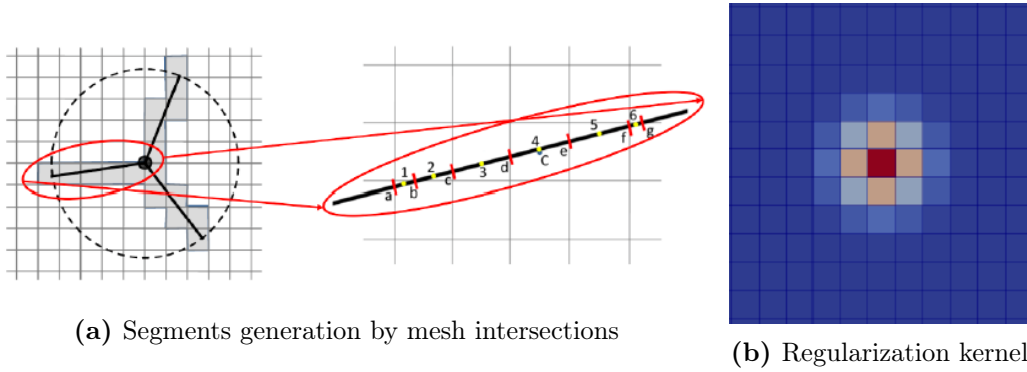
Figure 3.1: sketch of the actuator line method. *Source*: Bernini and Caccialanza [40]

from the airfoil's aerodynamic coefficients as in BEM. To do so, the blade's relative velocity vector in the rotor plane has to be evaluated. This allows to know both the angle of attack (α) and the value of W_D in order to compute the aerodynamic forces. Several ways to evaluate the blade's relative velocity have been proposed; the code used in this work adopts the EVM, a technique invented by Schito [39] which will be described in Section 3.2. Anyway, all the methods available have an explicit formulation, i.e. the velocity triangle is calculated from the velocity field of the previous time-step. This way the computational effort added to the solver is small and the implementation is simple.

Since its introduction, the Actuator Line method became very popular to perform detailed studies on the wake evolution [43,45]. Thanks to the absence of blades' boundary layer, most of the works published involved Large Eddy Simulations. Despite the good accuracy in wake reproduction, the integral loads (especially thrust) often showed discrepancies with respect to experimental values. The reasons for these differences can be various and will be discussed in Chapter 4. Even with the awareness of the difficulties in using AL method for precise dynamic analysis, it was decided to use it anyway to test its prediction capabilities with unsteady problems. Since dynamic inflow effects strongly depend on the wake evolution (Chapter 1), it was assumed that actuator line could provide accurate results in unsteady conditions (which are the focus of this Thesis). Furthermore, the choice of an AL code allowed to perform also a comparison with other codes results provided by partner institutions. The high detail in flow field modelling would even allow for a valuable unsteady wake development analysis in future work; for the purpose, PIV measurements of UNAFLOW are already available for validation. To the Author's knowledge there is no history of application of AL

for classical dynamic inflow problems (e.g. pitch steps); in the dynamic inflow work package of Mexnext III, no actuator line code was used. The FOWTs surge motion instead, was first studied with AL by Li et al. [49] who performed very similar simulations to those of Chapter 4. However, they focused on the impact of surge and pitch motions on wake and overall rotor performance, without going into the details of the thrust oscillation component. Indeed their aim was to arrive at building up a fully coupled solver including the hydrodynamic part [50]. With respect to this Thesis, a conceptually more similar work was that of de Vaal et al. [62], who investigated the relevance of dynamic inflow phenomena in FOWTs with a sinusoidal surge motion. They considered a very similar $A_s - f_s$ range to that of UNAFLOW, comparing AD simulations to BEM results featuring different dynamic inflow models; they also performed pitch steps validation as in Chapter 5. Despite the similar case studies, that work had a broader target embracing hints on wake development too. Here instead, the scope was more "vertical", analysing the thrust oscillation by virtue of its leading role in the dynamics of FOWTs. The main aim was to give a contribution to the knowledge base required for robust controller design. Moreover, thanks to the work already done in UNAFLOW and to the renewed partners' cooperation, a consistent cross comparison could be made up validating the data against experimental tests.

3.2 Code description

Several Actuator Line codes have been developed and are currently available. The most popular is probably the one included in SOWFA (Simulator fOr Wind Farm Applications), a set of CFD solvers, boundary conditions, and turbine models based on the OpenFOAM toolbox. SOWFA was developed by NREL and can be coupled with FAST, the NREL's CAE tool for aero-hydro-servo-elastic simulations of wind turbines. Nevertheless, such a complete tool was not useful for the scope of this Thesis. In fact, in order to understand the aerodynamic influence of the surge motion investigating the presence of dynamic inflow effects, it was necessary to separate this phenomenon from elastic and hydrodynamic contributions. Those would have dramatically increased the complexity of the results, hindering the recognition of clear cause-effect relationships. Despite the modular approach of SOWFA and FAST allows to decide what aspects have to be taken in consideration, it was decided to opt for a leaner solver package. Indeed,

the MECC's (Polimi) in-house developed code was selected, also owing to the long validation campaign conducted by that research group. The AL solver was written in C++ following the OpenFOAM programming rules. It is based on the PISO algorithm but it adds the routines for calculating the position of the actuator lines, evaluating mesh intersections, evaluating the velocity, calculating and applying aerodynamic forces to be included as source terms in the momentum equation. The code is rather simple as it only includes the aerodynamic part.

As anticipated, a key feature that distinguish such code from other AL codes available, is how the evaluation of the blade's relative velocity in the rotor plane ($\mathbf{W}_D$) is performed. Popular solvers, like SOWFA or EllipSys3D, sample the relative velocity vector at the very same point of the force application, i.e. the closest cell center to the actuator line intersection. Hence, the line representing the blade must pass through the airfoils pressure centers, often approximated with the quarter chord points. This way the bound circulation at those spots is close to zero and can be used to estimate $\mathbf{W}_D$. Unfortunately though, cell centers are not exactly positioned at the pressure centers and the quarter chord approximation is not accurate for non-symmetric profiles. Furthermore, the flow field in that zone is characterized by steep gradients, thus small displacements from the exact points cause rather significant α variations. This reduces the accuracy of loads estimation, especially when the inflow is turbulent. To improve the quality of relative velocity sampling, Schito proposed the Effective Velocity Model [39] that was implemented in the code used in this Thesis. The idea is based on the observation that in low solidity rotors, like those of typical HAWTs, the cascade effect is very small and the profiles act as they were isolated. This means that the aerodynamic force can be approximated with that of the isolated profile which depends on the upstream conditions only. The problem is that the presence of the induction field alters the far field conditions. Therefore the upstream velocity sampling must occur few chord lengths ahead of the leading edge, where a pseudo-far field velocity representative of the profile operating conditions is met. In order to reduce the impact of local effects (e.g. turbulence), Schito proposed to take a series of points along a line, perpendicular to the wind, estimating $\mathbf{W}_D$ as the vectorial average among the samples. The sampling line has to be placed a little upstream of the blade. Therefore, EVM depends on two parameters: the upstream distance where the line is placed and its length (the sampling points are obtained from grid intersections as standard actuator lines).

The EVM demonstrated to be a robust method as it was applied both for HAWTs [39,40] and lately also for VAWTs by Melani [51], providing promising results. A valuable advantage with respect to classical local velocity evaluation, is that it damps the traditional problem of RK's smearing parameter (ε) selection. In fact, an empirical evidence is that the turbine performance predictions of AL codes are heavily affected by the choice of ε in the regularization kernel function. Troldborg [45] stated that it had to be as small as possible but higher than $2\,l_{cell}$ to guarantee numerical stability. Several later works confirmed and aligned to this hypothesis [47,48,55], but still results appeared quite sensitive to such empirical parameter especially with fine grids. More recently, Martinez-Tossas et al. [52,53] found an optimal range for ε, basing on the comparison of the flow field with an analytical potential flow solution of a Joukowski airfoil. However, it is difficult to trust the generality of this approach. With EVM method instead, solution stability is guaranteed also setting $\varepsilon = 1\,l_{cell}$ which is expected to improve the accuracy of the AL model. It is worth to recall that also EVM has an explicit formulation, allowing the use of the conventional PISO algorithm to solve the pressure-velocity coupling.

Another widely exploited feature of the code was implemented by Bernini. He modified the original AL solver giving the possibility to assign both a sinusoidal surge motion to the turbine and a generic collective blade pitch law. The two can be combined together providing considerable freedom to the user. In this work though, surge and blade pitch motions were considered separately: the first for UNAFLOW and out-of-UNAFLOW simulations (Chapters 4 and 5); the other to perform pitch steps for dynamic inflow validation (Chapter 5). All the simulations performed for this Thesis ground on Bernini's remarkable programming work.

3.3   Simulations settings

The Actuator Line solver developed by Bernini is written in OpenFOAM and it is available only for the incompressible case. The small scale of the turbine to be reproduced resulted in a flow regime in the low subsonic range (M<0.3) even at the blades tips; thus, compressibility effects could be neglected without concerns. The scaled turbine was modelled simply as three rotating (and eventually surging) actuator lines. Neither the presence of the tower nor of the nacelle was taken into account. The lack of the latter had a certain influence on the flow field around

the root and, consequently, on the thrust estimation. Nevertheless, including it in the code would have required a relevant programming effort, provided that it had to move along with the blade lines in surge. Furthermore, since the blade root contribution is much smaller than the tip's, the inclusion of the nacelle could only partially affect the results and it was neglected indeed. For what concerns the tower instead, it could have been easily included in the model as another actuator line with an associated drag coefficient. Although, its influence on the aerodynamic loads was expected to be absolutely negligible. In the same way the gravitational force field was not considered.

In the following paragraphs all the set up of the CFD simulations and the models used for solving Navier-Stokes equations are discussed thoroughly.

3.3.1 Computational domain

The computational domain aimed at reproducing faithfully the Boundary Layer Test Section of the GVPM, where UNAFLOW tests were conducted. For this reason, the shape of the doamin was a simple parallelepiped with a cross section 13.84m wide x 3.84m high. Only the streamwise dimension was changed in order to guarantee the proper velocity inlet and the pressure recovery in the downstream wake. In particular, the inlet was placed 5m upstream of the turbine (i.e. where the inflow velocity was measured in UNAFLOW) and the outlet 15.36m (about $6.5\,D$) downstream. The overall axial length was 20.36m. The domain was divided in blocks for meshing purposes (fig.3.2). In the block of the turbine (block E), a background mesh made of cubic cells (i.e. with aspect ratio 1:1) was created using *BlockMesh*. This way refining the mesh up to level 2 with *SnappyHexMesh* provided better quality elements. For this reason the downstream dimension was chosen multiple of the height of the domain. As a result, within block E the cells could be described by a single characteristic length for each refinement level.

3.3.2 Grid layout

All the meshes produced for the mesh sensitivity analysis (Section 3.4) shared the same layout with equal refinement zones dimensions. The only parameter that changed was the characteristic length of the cubic cells within block E (fig.3.2). Such block ranged from 1 domain height ($\sim 1.6D$) upstream to 4 downstream,
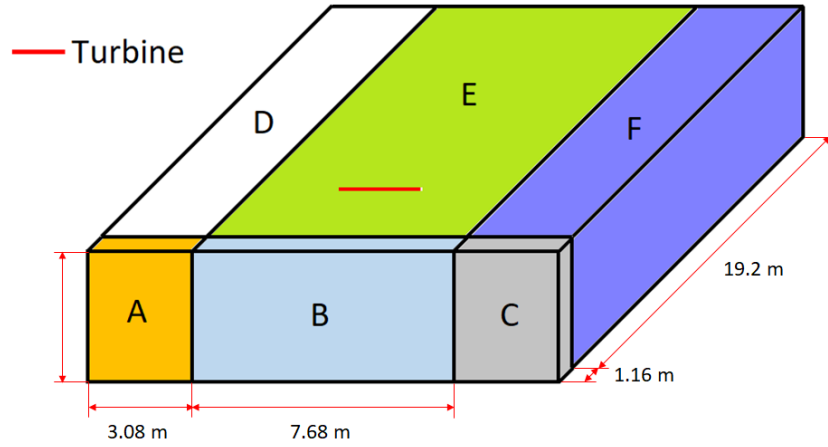
Figure 3.2: blocks division of the domain

with a width of 2 heights; hence, all the relevant part of the flow field was therein contained. The other blocks were only necessary to match the wind tunnel section dimensions and reach the velocity measurement point upstream. Therefore, in all those zones a grating was set in order to spare some cells farther from the bulk. Great care was taken in order to smooth the transitions: grating coefficients were all calculated to have the first cell out of block E of the same dimension of those inside. The effect of this choice can be appreciated in fig.3.3a. Thanks to the absence of the turbine, the simple geometry of the domain allowed for utterly structured grids made of hexaedral elements. After the creation of the base mesh, two cylindrical refinement zones were inserted in block E (fig.3.3c and 3.3b), both centered at the hub of the turbine ($h_{HUB} = 2.055$m). The first had a diameter of $2D$ and extended from $1D$ upstream of the turbine until the end of the domain. There the level of refinement was set to 1, i.e. the *BlockMesh* cell dimension was halved. This zone was required to better capture the wake evolution (reducing the impact of numerical viscosity). The second, instead, had a diameter slightly larger than the turbine ($7/6D$) and ranged from $0.125D$ upstream to $0.125D$ downstream with a refinement level of 2. In this zone the element size was $1/4$ of the initial one. The aim of such refinement was to both raise the number of cells per blade line (χ), and to properly capture the formation of tip vortices affecting the wake development.

Thanks to the modular approach followed in meshes generation, the main quality parameters were almost independent on the number of elements. In

41
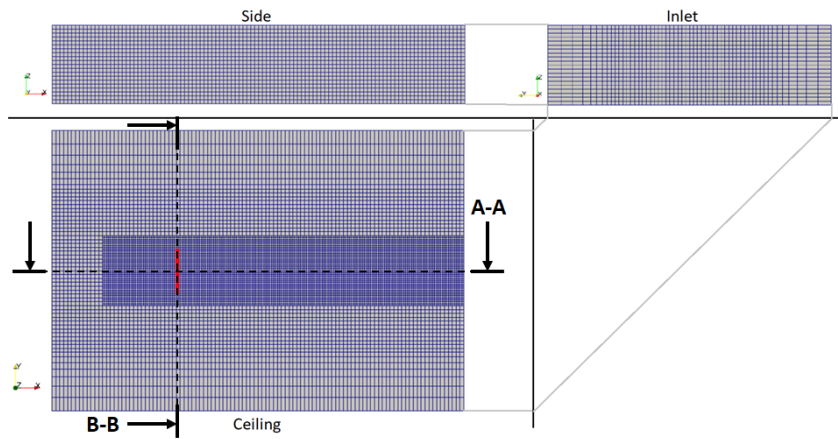
(a) Views of the meshed domain
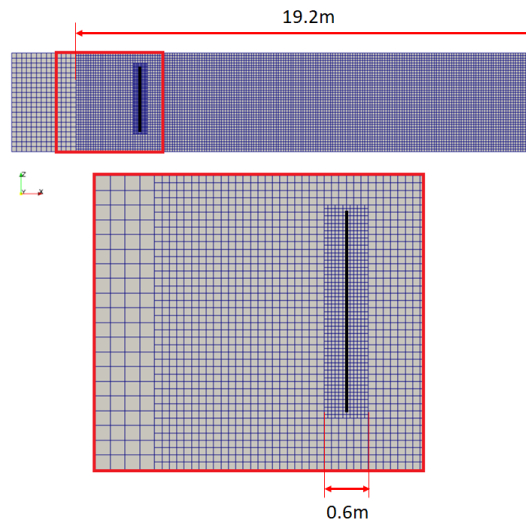
(b) A-A Section of the domain (zoom below)
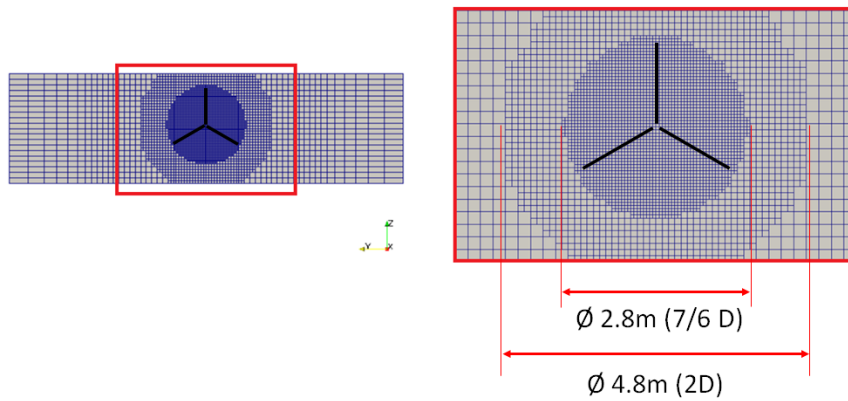
(c) B-B Section of the domain (zoom on the right)

Figure 3.3: scaled model experimental setup

particular, the maximum cell skewness was 0.33 for all the grids created; the average non-orthogonality index was always below 4°, monotonically reducing with the number of cells because in block E this index was close to zero. The mesh selected by the sensitivity analysis to perform all the unsteady simulations had an initial cell length $l_{cell0} = 64$mm. The total number of elements was 11,626,510 with 75 cells per actuator line. The reasons for the choice of this grid will be explained in Section 3.4.

3.3.3 Turbulence model

Thanks to the absence of the turbine, AL simulations can be often coupled with LES models to account for turbulence. Large Eddy Simulations rely on spatial filtering of pressure and velocity fields (incompressible case) rather than ensemble averaging (RANS). With this approach the turbulent structures greater than the filter size (Δ) are solved directly, while the smaller ones are accounted by means of a Sub Grid Scale model. The filtering operation is performed by the convolution of a generic field with a filter kernel function. This function has associated a characteristic time (time-step) and a scale (Δ), that determine what part of the energy cascade is solved and what is modelled. When filtering is performed, the fields can be splitted into filtered (denoted with $^{-}$) and sub-filtered portions ('):

$$\mathbf{u} = \overline{\mathbf{u}} + \mathbf{u}' \; ; \tag{3.7}$$

$$p = \overline{p} + p'; \tag{3.8}$$

Inserting this decomposition in the Navier-Stokes equations, the SGS stress tensor appears as a new unknown (more details can be found in [54]). To model this term and close the system, the standard Smagorinsky model was adopted. More complex dynamic models could have been selected but their impact on the results was proved small by Sarlak et al. [55], provided that sufficient grid refinement was present. The application of such model leads to the following formulation of the momentum equation (incompressible case, negligible body forces, AL source term):

$$\frac{\partial \overline{\mathbf{u}}}{\partial t} + \nabla \cdot (\overline{\mathbf{u}}\overline{\mathbf{u}}) + 2(\nu + \nu_{SGS})\nabla \cdot (\nabla \overline{\mathbf{u}} + (\nabla \overline{\mathbf{u}})^T) + \frac{\mathbf{f}}{\rho} = -\frac{1}{\rho}\nabla \overline{p} \; ; \tag{3.9}$$

$$\nu_{SGS} = (C_s\Delta)^2(\nabla\overline{\mathbf{u}} + (\nabla\overline{\mathbf{u}})^T); \tag{3.10}$$

with C_s=0.1678 for isotropic turbulence. For the filter size the cube root approach was chosen, thus in the internal zones where cells were cubes $\Delta = l_{cell}$.

3.3.4 Boundary conditions

The boundary conditions aimed at reproducing the tests' incoming wind speed and the pressure recovery in the far wake. The wind tunnel walls were considered perfectly smooth in order to avoid the need of solving the boundary layers, that would have required a lot more cells without adding useful information to the simulations. In fact, in wind tunnel tests the rotor was placed far enough from the walls so that the boundary layers had little influence on its performance. The most relevant effect was the contribution to the blockage due to the B.L.'s displacement thickness, which produced a minimal error anyway. A more significant impact would have been given by the inflow turbulence. Since these were the first simulations conducted on this topic and the wind tunnel flow quality was rather good (T.I. ∼2%), it was decided not to account for turbulence in the inflow. Its addition would have required computationally expensive precursor simulations. The large experience of the GVPM research group in such kind of problems, gives the possibility to take it into account in future works. However, for what concerns the dynamic part, the consideration of turbulence is just expected to add stochastic high-frequency components to the signals, that would be erased when the surge component is extracted. Therefore, it was decided to leave it out since its role was not relevant to the purpose of this Thesis. If, instead, an accurate wake development analysis had to be performed, inflow turbulence would have to be considered. It is worth to underline that the lack of turbulence at the inlet does not mean an absence in the whole field. Indeed, the LES turbulence model reproduces the flow instabilities in the domain, thus turbulent structures develop right after the inlet and are then promoted by the actuator lines. Hence turbulence was present in the simulations, but with a smaller intensity since it formed only after the inlet. The complete set of boundary conditions is reported in table 3.1. The *slip* condition on the sidewalls reproduces the ideally smooth wall surface. At the outlet an *inletOutlet* condition on the velocity was set, instead of simple *zeroGradient*, for better stability.

---

[1]Relative pressure.

BC	Inlet	Outlet	Sidewalls
U	*fixedValue* (V_0)	*inletOutlet*	*slip*
p	*zeroGradient*	*fixedValue* (0^1)	*zeroGradient*
ν_{SGS}	*fixedValue* (0)	*zeroGradient*	*slip*

Table 3.1: Boundary conditions for AL simulations

3.3.5 Numerical schemes

The code adopted the Finite Volume Method in order to solve the Navier-Stokes system of equations with Smagorinsky model (eq.3.1, 3.9 and 3.10). The discretization techniques used for the different terms were:

- **Time scheme**: *Crank-Nicolson 0.9*; a hybrid 1st-2nd order scheme with high blending coefficient (i.e. almost purely 2nd order). The short time step required by LES made its influence low anyway.

- **Gradient scheme**: *linear*; purely 2nd order accurate scheme based on central difference.

- **Divergence scheme**: *QUICK*; a 3rd order scheme was used for the convective term in order to improve the accuracy especially in the advection of tip vortices.

- **Laplacian scheme**: *linear corrected*; 2nd order scheme with non-orthogonal correction. In reality, the very good orthogonality of the mesh would have allowed to avoid the consideration of the correcting term. Although, it did not cause any instability issue to the solution, thus it was left in all simulations.

3.3.6 Solver settings

As previously anticipated, the AL solver was based on the PISO (Pressure-Implicit with Splitting of Operators) algorithm. Such algorithm grounds on the hypothesis that, if a sufficiently small time step size is used, the non-linear coupling given by the momentum convection term becomes negligible with respect to the pressure-velocity one. This observation allows to linearize the momentum equation and find an approximated solution efficiently. PISO is an extension to the unsteady case of the SIMPLE (Semi-Implicit Method for Pressure Linked

Equations) algorithm. The same two steps are required to solve the pressure equation indeed: the momentum predictor and the pressure correction. Before passing to the new time step, those two steps are iterated as many times as the number of correctors selected. Thanks to the initial hypothesis, the coefficients of the momentum predictor equation are evaluated from the velocity field of the previous time step and remain constant throughout the loop. Such strategy provides a fast and efficient solution scheme for highly unsteady cases, where high temporal resolution is required (e.g. LES). It is important to notice that the repetition of the pressure correction step allows to avoid the use of under-relaxation factors. Following the commonly accepted best-practices, 3 internal correctors were set without any non-orthogonal correction step, owing to the high quality of the mesh (average non-orthogonality $<5^o$).

For what concerns the linear equations solution, a GAMG (Generalised Algebraic Multi-Grid) solver with a Gauss-Siedel smoother was employed for the calculation of p. This algorithm is based on a multi-grid technique, i.e. it considers a progressively coarser mesh to find the solution faster. In fact, errors at high frequency are much easier to eliminate than low frequency ones; but, a low frequency error for a fine grid becomes an high frequency one when the grid is coarsened. Moreover, all the information of a coarse mesh is already contained within a finer one, thus there is no need of creating more than one mesh. This approach is typically the most efficient for the evaluation of p. For the other variables (i.e. **u** and ν_{SGS}), a preconditioned bi-conjugate gradient (PBiCG) method, with a diagonal incomplete lower-upper (DILU) preconditioner for asymmetric matrices, was adopted. For every variable, the tolerance level for the final iteration was set to 10^{-6} (without relative tolerance). The residuals' behaviour of every single simulation was carefully controlled to verify the proper convergence.

3.3.7 Actuator Line settings

The study of the optimal parameters selection for the Actuator Line model featuring EVM technique was performed by Bernini and Caccialanza [40]. The conclusions were drawn comparing the velocity profiles at several positions downstream of a fully meshed airfoil with those obtained with an actuator force; the tests were conducted in 2D. At first, they found that the minimum smearing parameter guaranteeing the lack of wiggles in the solution was $\varepsilon = 1\,l_{cell}$. This

confirmed the improved stability reached with EVM. Furthermore, they also sought the optimal upstream distance for the placement of the sampling line by minimizing the error among meshed airfoil and actuator force cases. They concluded that the best position was $1.5\,l_{cell}$ upstream of the actuator point. Finally, by considering the attack angle difference, they also suggested to set the line length to $5\,l_{cell}$. Despite the generality of such conclusions is undoubtedly arguable, the lack of more robust analyses (the code is still in development) together with the good results found, led the Author to trust these settings as empirical rules. Therefore, this set of parameters was used for all the simulations.

Another major input for Actuator Line simulations (as for any lifting line code) are the blade profiles' polar data. Indeed, to calculate the aerodynamic forces from eq.3.5 and 3.6 the knowledge of the curves $C_L(\alpha)$ and $C_D(\alpha)$ is required. As well-known from airfoil theory, also the profile's Reynolds number plays a role in the curves, especially if lower than a certain threshold (usually around $\sim 10^5$). Although, it is not common to include Re dependency of the polars in lifting line code. More often, care is taken in order to get lift and drag coefficients curves at a Reynolds which is representative of the actual airfoil's operating conditions. Latter approach was adopted also in this work. Despite the availability of tables for the aerodynamic coefficients of the SD7032 profile (used for the scaled model's blades), the polars used for the simulations were obtained experimentally. In particular, as part of the UNAFLOW project scope, a long test campaign on the performances of that profile was conducted in the DTU Red open-loop wind tunnel [11]. This facility was designed specifically for the 2D characterization of winglike profiles; its cross section measures 500x500mm^2 and the maximum wind speed is 65 m/s, reached with very low turbulence (T.I.<0.1%). Turbulence intensity can be increased adding wires of different widths upstream the test section. Another key feature of the DTU Red is the turntable for dynamic control of the aerofoil's attack angle, suitable to study dynamic stall cases. For the UNAFLOW campaign a wing model featuring the SD7032 profile and equipped with 32 pressure tabs at midspan (for lift evaluation) was manufactured. Both steady and unsteady (i.e. sinusoidally changing α) tests, at different Reynold numbers, with and without tripping wires were conducted. Steady tests were also compared with CFD simulations for cross validation. A very large database was created. Among all the steady curves obtained, Bernini (who personally participated to the experiments) carefully chose those closer to the scaled model

operating conditions. Those polars were then implemented in the code used for running the simulations of this Thesis. For what concerns the initial part of the blade root (up to $\sim 7\%$ of the span), which had a tubular shape ($\varnothing55$mm), only a constant $C_D = 1.035$ was assigned. Drag was considered independent on the angle of attack and vortex shedding was not considered for simplicity. The impact of this choice is expected to be negligible anyway.

To conclude this Section, it is important to remark a critical aspect regarding the airfoil's data. Even if high quality tests were undertaken to get accurate aerodynamic coefficients, all the data were obtained in 2D conditions. Nevertheless, it is now well-known that 3D effects play an important role at the root of wind turbines' blades, where radial flows tend to delay the stall drastically increasing the lift at the same time. In this region 2D aerodynamic coefficients are not suitable to accurately reproduce the forces exchanged. Moreover, with such a small rotor ($\varnothing2.38$m), the impact of these effects to the overall machine's performance might be high, increasing the uncertainty associated to the load estimation. Despite 2D polars corrections for 3D effects exists, they are still empirical and lack of generality; hence, no model was applied to account for that.

3.4 Mesh sensitivity analysis

A mesh sensitivity analysis was performed in order to verify the dependency of the simulations results on the size of the cells. This way a suitable grid, common to all simulations, could be selected. Five different meshes with increasing number of elements were created, always following the layout described in Section 3.3.2. In particular, the shapes and the sizes of both the domain and the refinement zones were common to all the grids. The only difference was in the initial selection of the characteristic cell length for refinement level 0 (set in the *BlockMeshDict*). This way all the quality parameters remained more or less constant and the finer meshes could be created progressively reducing the l_{cell0}. The main features of each grid are reported in tab.3.2. The sensitivity analysis was performed reproducing UNAFLOW - RATED2 conditions (tab.2.1). A key quality parameter for AL simualtions is the blade line resolution (χ), i.e. the average number of cells intersected by an actuator line at each time step. Several studies have shown that this number should be at least between 30-40 in order to achieve good

---

[2]Used only for RATED2 conditions.

Name	l_{cell0} [mm]	l_{cell1} [mm]	l_{cell2} [mm]	cells n^o.	χ	Δt^2 [s]
MESH#0	192	96	48	428,008	25	0.001
MESH#1	128	64	32	1,469,370	37	0.001
MESH#2	96	48	24	3,440,626	50	0.0005
MESH#3	64	32	16	11,626,510	75	0.0005
MESH#4	55	27,5	13.75	18,539,920	87	0.0004

Table 3.2: computational grids characteristics

accuracy [47,55]. Except MESH#0, which was used for preliminar tests, all the grids generated fulfilled such requirement. Another fundamental point is the selection of the time step size (Δt). For making this choice, different constraints were taken into account. First of all, the need of solving the grid scale turbulent structures directly, imposed a strict constraint on the CFL condition to ensure stability. In fact, in Large Eddy Simulations a good correspondence between spatial and temporal resolution must be guaranteed. Best practices suggest to keep the Courant number below 0.5 in LES; therefore all Δts were chosen to respect this requirement. Another important aspect, again inherited by AL simulations best practices, was to prevent the tip of the blade line from crossing more than one cell per time step to maintain a smooth application of the source term [47]. Finally, the value of Δt had to be chosen in order for the sampling frequency ($f_{samp} = 1/\Delta t$) to be a multiple of 0.125Hz to avoid leakage at any surge frequency of the UNAFLOW test matrix (all multiples of the minimum frequency, i.e. 0.125Hz). The respect of all these constraints led to the values of Δt reported in tab.3.2.

The convergence parameters chosen to perform the analysis were the integral thrust and torque values predicted, during steady turbine operation in RATED2 conditions. The results of such analysis are shown in fig.3.4 where the loads are compared with the steady wind tunnel tests conducted for UNAFLOW. The underestimation of the thrust force, no matter which mesh was chosen, can be noticed. However, the comparison between AL simulations and experiments will be discussed in detail in Chapter 4. For what concerns the grid sensitivity analysis, what mattered were the trends varying the number of elements. In particular, a weak increasing trend of both thrust and torque was found when the mesh was refined. The differences in terms of aerodynamic loads among MESH#2, MESH#3 and MESH#4 were rather small; hence, a good convergence
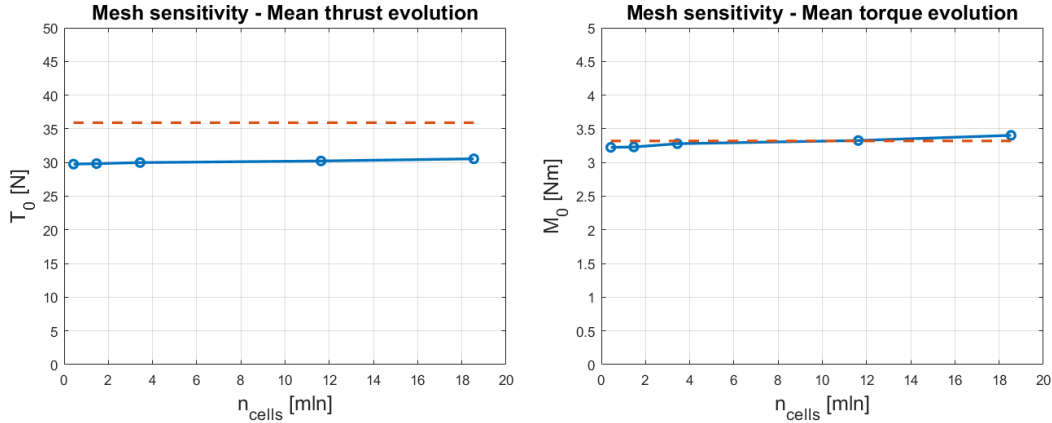
Figure 3.4: mesh sensitivity results

was already achieved with 50 cells per actuator line. Nevertheless, the lack of historical references on unsteady aerodynamic investigations with AL and the abundance of computational resources made available on Cineca HPC, pushed the Author to opt for MESH#3. In fact, having 75 cells per blade allowed for an increased confidence in model's predictions, even in the unsteady case for which there is not a history of validation. A finer mesh also allowed for a more accurate near wake reproduction, deemed fundamental for capturing eventual dynamic inflow effects. With such accuracy level, also a wake evolution analysis could be performed in future work, eventually adding inflow turbulence with a precursor simulation. Although, the increased number of cells adopted raised the computational cost of the simulations. The sustainability of this choice was guaranteed by the hours of calculation provided by ISCRA (Italian SuperComputing Resource Allocation) on Cineca Galileo HPC cluster. In Galileo the simulations could run in parallel on 216 processors featuring the MPI protocol, solving the simulation duration issue. On average, a second of simulation with MESH#3 took about 50 minutes to complete.

3.5 Conclusions

In this Chapter, the code used and the modelling choices made to perform the simulations were discussed. The mesh, the domain, the numerical schemes, the Actuator Line and solver's settings reported were common to all the calculations performed, so as to assure they were consistent to each other. A great care was devoted to the compliance of the AL parameters to the quality guidelines

suggested in literature. For the optimization of the EVM technique, the reference was the work of Bernini and Caccialanza [40]. For future improvement though, a detailed analysis of the influence of EVM's parameters on the results would be advisable, to verify the robustness of the optimal values adopted in this work. The basic, yet effective, code might be refined adding the possibility to include the nacelle in unsteady simulations. The relevant uncertainty involved in the simulations, especially in unsteady conditions, explained the conservative choice of the finer MESH#3, against MESH#2, despite the differences in terms of integral loads appeared small. The data generated would allow also for a detailed near-wake analysis focused on the tip vortices. However, for a more accurate reproduction of the near-wake/far-wake transition, the inclusion of both turbulence and nacelle would be indispensable.

In conclusion, a very useful task would be to compare the predictions of the code used with those of another AL code (e.g. from SOWFA) to verify the influence of the EVM technique.

Chapter 4

UNAFLOW Simulations

In this Chapter, numerical results and UNAFLOW wind tunnel tests are compared in terms of thrust oscillation's amplitude, phase and equivalent aerodynamic damping. The comparison aims at updating the one reported in the final UNAFLOW report [11]. The results shown in this Chapter come from a renewed fruitful cooperation among the former project partners: Polimi, TNO (former ECN) and USTUTT. Ultimately, also Rémi Corniglion from EDF actively participated to the work hereby presented, adding valuable numerical results to the comparison. Diversely from the UNAFLOW report, a revised version of TNO's numerical results was included, since a fault had been discovered in the set up of the original simulations. Moreover, also the outcomes of the full CFD model of USTUTT [60], which could not be inserted in the old report for a slight setback, were added to this new comparison. Another slight modification was that the reference experimental tests featured the new inertia subtraction procedure, described in Chapter 2, rather than the standard one. The base's displacement signal was chosen as reference. The results of Author's AL simulations were included too. Then, the last numerical data were kindly provided by Corniglion (EDF), who replicated all the AL simulations featuring a Free Vortex Wake model. Finally, a simple quasi-static model was developed and used to have a clear theoretical reference. To summarize, the comparison was composed by:

1. **Numerical Part**:

   - **BEM**: from TNO (ECN Aero-Module [61]).

   - **AWSM**: Free Vortex Wake code from TNO (ECN Aero-Module [61]).

   - **FVW**: Free Vortex Wake code from EDF.

- **AL**: Author's Actuator Line simulations.

- **CFD**: full CFD model (in FLOWer) from USTUTT [11].

2. **Experimental Part**:

   - **WT**: revised results from UNAFLOW experimental campaign. The inertia subtraction followed the alternative procedure, described in Chapter 2, using the LVDT as phase reference (i.e. BASE-Ref).

3. **Theoretical Part**:

   - **Quasi-static model**: simple linear model based on the quasi-static theory.

The Chapter is divided in three main sections. First, Section 4.1, presents the comparison in terms of steady turbine's performances and the induction extraction method used in AL simulations. In Section 4.2, instead, the focus is on the unsteady operation, with the turbine subjected to an imposed harmonic surge motion. The cases considered were part of the UNAFLOW matrix in RATED2 conditions. Section 4.2 also describes the simple quasi-static model, which is used as a theoretical reference, and its parameters evaluation. The last section (Section 4.3) reports the final comments and conclusions. The work presented hereinafter pursued the double aim of validating AL code results while updating and completing the cross-comparison started in UNAFLOW.

4.1 Steady results

For what concerns the AL code, as soon as the reference mesh (MESH#3 of tab.3.2) was chosen, an assessment of the turbine's performance in steady conditions was conducted to test the model's prediction capabilities. For the purpose, all the steady UNAFLOW tests at RATED1, RATED2 and ABOVE conditions were considered. Unfortunately, the complete scaled model's characteristic curves had not been obtained in the experimental campaign. Therefore, the AL simulations involved only the three UNAFLOW steady cases. To run those simulations the set up described in Chapter 3 was adopted. The only exception was the time step selection: the lower rotor speed (Ω) at RATED1 allowed for a $\Delta t = 0.0008$s; vice versa the ABOVE simulation required a $\Delta t = 0.0004$s.

During the final post-processing also some tests performed within LIFES50+ were found and have been included in the comparison of fig.4.1. For reference, also the design curves of the DTU10MW RWT have been added. It can be noticed that the difference in terms of power coefficient between the scaled model and the original turbine was relevant, especially at low wind speeds. In fact, the scaling procedure's priority was to match the thrust force rather than the torque. Getting both at low wind velocities collided with other design constraints, thus a similar mismatch was justified. Moreover, the original velocity scale chosen for the model was of 1:2, only afterwards changed to 1:3 in order to reduce the surge frequencies to be considered for unsteady tests. This caused a further reduction of Re, that explained the slight differences with the reference C_T curve [10]. Some discrepancies between LIFES50+ and UNAFLOW tests were also there, especially for C_p, probably owing to measurement uncertainties. In RATED2 and ABOVE conditions though, the match with the RWT curve was satisfactory.
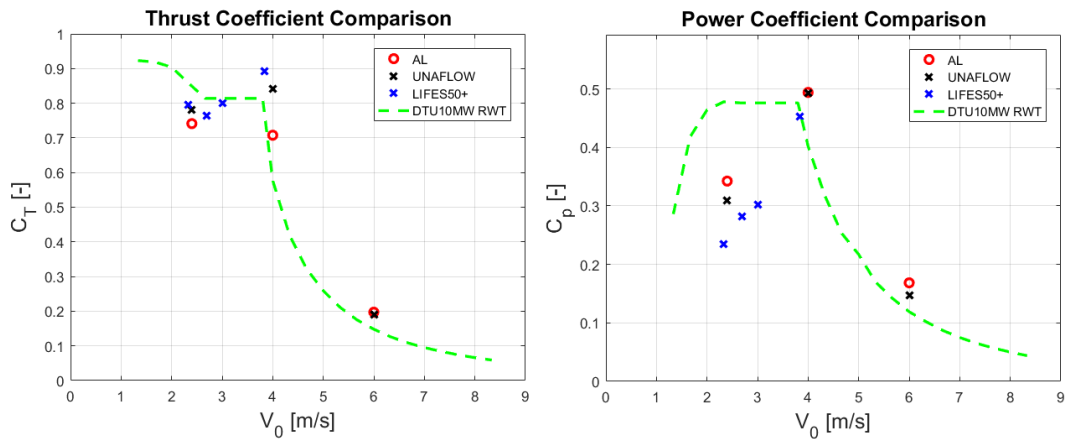
Figure 4.1: Thrust and power coefficients comparison at different wind speeds

With regard to the AL model, at RATED1 the thrust was slightly underestimated ($\sim$5%) whilst the opposite happened for the power coefficient. Much more important was the comparison at RATED2, where the power was perfectly matched but the thrust force was underrated of about 15%. Finally, in ABOVE conditions where the pitch regulation was active and the angle of attack was reduced to keep a constant power output, the thrust was well captured with just a slight C_p overestimation.

Overall, the Actuator Line code had the tendency to under-predict the thrust force, whilst slightly overrating the torque. The first effect was much more

pronounced, especially in RATED2 conditions where the angle of attack was greater than in ABOVE and W_D was higher than in RATED1. It is important to highlight that similar thrust force prediction deficits are not uncommon when dealing with AL simulations. In traditional AL literature it is common to find errors from $\sim 5\%$ up to $20 - 25\%$ in the thrust coefficient, most of the times below the experimental values [43,47,55,56]. Such faulty behaviour might be ascribed to several concurring reasons. First of all, the presence of radial flows at the roots of the blades, delaying stall and significantly increasing lift, might have had an impact in the scaled model's loads. In fact, the span portion operating in 2D conditions (i.e. far from tip/root) was small in such short blades; hence the relative importance of finite wing effects could have been high. The experimentally obtained polars used, despite their quality, could not foresee these phenomena since they had been obtained in 2D (Chapter 3). Three-dimensional effects at the root had a limited impact on the torque because of the short lever arm, eventually explaining why it was not under-predicted too. Furthermore, this hypothesis agreed also with the evidence that the RATED2 deficit was higher than RATED1, while in ABOVE conditions the gap was absent. The aerodynamic forces, indeed, scale with W_D^2 which increased when the wind speed and the rotational speed (variable speed rotor) were raised. Instead, in ABOVE the feathering pitch regulation reduced the attack angles decreasing also the impact of root radial flows on the thrust force. Nevertheless, the severity of the underestimation made it hard to believe this to be the only cause. In fact, another relevant contribution quoted also by Martínez-Tossas [47], might have been the lack of the nacelle. In the simulations, the flow in the hub zone was free to pass across the rotor instead of impinging to the nacelle and contributing to the thrust. Even if a pure stagnation was assumed thereby, the additional force generated (estimated as $1/2\,\rho V_0^2 A_D$) would have only raised the estimate of about 1%. A more important consequence might have been the reconfiguration of the flow field at the inboard section. The nacelle would have caused an increase of the axial velocity component at the root (as a blockage effect) that would have strengthened the root forces previously discussed. Finally, also the extremely simple modelling of the inner cylindrical parts described with a constant C_D, might have had an impact, albeit weak. Unfortunately though, these reasons lost a bit of their credibility when the results from other lifting line codes (BEM, AWSM and FVW) were delivered. Those models indeed, provided better estimates for the thrust despite the use of

2D polars. Such unexpected differences have driven a thorough revision of the AL results with the help of the project partners, who provided additional data for spotting the error source. Unfortunately, this revision has initiated very close to the deadline for submitting this work. Therefore, the updated results available at the latest possible time will be reported in Appendix C.

The steady thrust mismatch in RATED2 conditions did not stop the analysis to move forward. Indeed, the real focus was on unsteady aerodynamic effects rather than steady loads estimation. Despite the better accuracy reached in the ABOVE case, the interest was on rated wind conditions where the turbine loading was maximum and dynamic inflow effects would have been more relevant if present. The better signal to noise ratio, with respect to RATED1 unsteady tests, explained the preference for RATED2 that will be considered henceforth. The exact same choice had been made in the unsteady part of the UNAFLOW project, but the revision and update of both the numerical and experimental data arouse the will of restoring that comparison. For what concerns the steady conditions, the results from all the codes are reported in tab.4.1. The CFD simulations were performed by USTUTT featuring the solver FLOWer, developed by DLR, and using a k-ωSST turbulence model. For the steady case, only 1/3 of the turbine was modelled (named CFD 1/3) exploiting the symmetry [11]; with this approach the wind tunnel environment was neglected. The full model, which reproduced the test section faithfully instead, was employed only for the unsteady cases. Nevertheless, the verified validity of the quasi-static theory (Section 4.2.3), allowed to estimate the the steady predictions of the full model simply considering the time averages of the unsteady thrust and torque responses. The corresponding outcomes are referred to as "CFD" in tab.4.1. Free Vortex Wake model results were then provided by both TNO (with AWSM) and Corniglion (with EDF's in-house code). Only the second modelled the test section, but the profile polar data used were different. TNO also shared the data from their BEM code, part of their Aero-Module, always neglecting the presence of the wind tunnel.

	WT	AL	CFD	CFD 1/3	AWSM	BEM	FVW
Thrust [N]	35.91	30.44	36.57	34.2	34.5	34.65	31.73
Torque [Nm]	3.32	3.32	3.34	2.91	2.97	2.93	2.83

Table 4.1: steady performance comparison: UNAFLOW RATED2 conditions

As anticipated, the AL results featured a 15% thrust underestimation with

a perfect torque match. Hopefully, the ongoing revision will clarify the root causes of such discrepancy (Appendix C). The full CFD results considering the wind tunnel environment reached very good accuracy, with an error below 2% on the thrust and lower than 1% on the torque. The good agreement among 1/3 CFD simulation and both TNO's codes aroused the belief that their loads underestimations could be utterly ascribed to the blockage effect. In fact, the blade mesh of the 1/3 case was the same used in the full model and, provided that the incoming flow was uniform, the only relevant difference was the presence of the wind tunnel walls. The significant underestimation, of both thrust and torque, found with the FVW model was almost certainly caused by the use of standard tabulated airfoil data rather than experimental ones. Corniglion indeed, who performed such simulations, was not part of the UNAFLOW project and did not have access to DTU's profile data at that time. At the end of the ongoing AL results revision, all the codes will employ the same polars and updated results will be published.

4.1.1 Induction extraction

The knowledge of the induction field is fundamental for the analysis of rotor unsteadiness phenomena like dynamic inflow. The long experience matured with BEM codes has made induction among the most useful parameters to draw information on the turbine's operating conditions. Since AL simulations compute the flow field from the Navier-Stokes equations, unlike BEM or FVW codes the axial and tangential inductions are not used for aerodynamic forces calculation. Therefore, the values of a and a_t have to be derived from the flow field to compare with the outputs of other codes, or to simply gain insight on the loading conditions. Several ways to extract the induction parameters from CFD computations were proposed. A complete review and comparison among the different methods was produced by Rahimi et al. [57] and it was then summarized in Mexnext III [16]. Originally, the main purpose of extracting induction and, consequently, angle of attack from high-fidelity simulations was to obtain the 3D corrected airfoil polars by reverse engineering. Although clever, this strategy was blocked by a limitation common to all the methods: the impossibility to provide accurate results in the regions affected by 3D effects, i.e. the most interesting ones. In fact, it was shown that all the techniques proposed performed very well in the midspan region with minimal differences among them. Conversely, close to the tip or the root, none of

the models could systematically match the measurements. As a result, the choice of the method was dictated by the ease of implementation in OpenFOAM. The simplest way to avoid the need of adding pieces of code to the solver, was the so-called Azimuthal Average Technique (AAT) or axial velocity method proposed by Hansen et al. [58]. A reference for the use of this approach was the work of Sørensen [59].

The AAT consists of estimating the axial and tangential velocity components at the rotor plane (V_a^D, V_t^D), required for calculating a and a_t, by interpolation between upstream and downstream samples. First of all, two planes parallel to the rotor's have to be placed one a little upstream and one a little downstream of the turbine. Then, the radial position at which the induction needs to be known is selected and the corresponding circles (centered at the hub) are considered in the two planes. A series of sample points are evenly distributed azimuthally along these circumferences. At each of these points the axial and tangential velocity components are stored at each time step. At this point the azimuthal average is performed: at each time step the values of axial and tangential components of all the points of the annulus are averaged respectively. This way, for the radial position chosen, at each time step the pairs of values ($\overline{V}_a^{up}$, $\overline{V}_a^{down}$) and ($\overline{V}_t^{up}$, $\overline{V}_t^{down}$) will be available. This averaging step is required to cancel the effect of the blade passage, because the induction parameters are inherited from momentum theory in which the turbine is modelled as a disk (i.e. as if it had an infinite number of blades). Finally, to get the velocity components at the rotor plane at that time step it is enough to take the average between upstream and downstream values, provided that the sampling planes are equidistant from the rotor plane. The accuracy of this method strictly depends on the streamwise position of the planes. They should not bee too close to be heavily affected by the passage of the blade, but close enough to have the sampling points approximately on the same streamline. In fact, the method grounds on the local 2D flow assumption which is unsuitable in case of significant radial flows and wake expansion. Furthermore, as for any averaging technique, the higher the azimuthal resolution the greater the accuracy. Of course this method is only effective in azimuthally uniform conditions and should not be used otherwise, e.g. in yawed flows. The simplicity of its implementation is an asset that is counterbalanced by the cumbersome data processing effort to be performed. Indeed, a large number of values have to be stored at each time step.

(a) Sampling grid layout

(b) Qualitative velocity profile interpolation
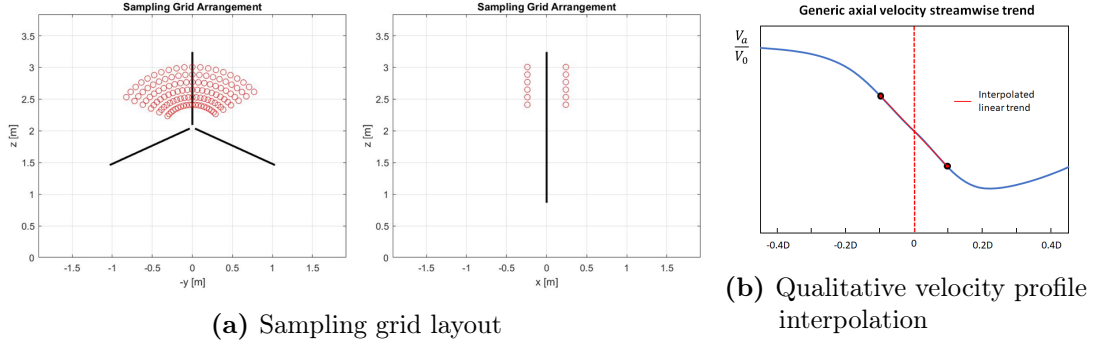
Figure 4.2: Azimuthal Average Technique implementation

In Author's AL simulations it was chosen to extract the induction coefficients at five different radial positions, respectively at $(30,40,50,60,70,80)\%$ of the span. The upstream and downstream planes were located at a distance of 0.1D from the rotor plane. Since the inflow was always uniform in the cases considered, the symmetry was exploited: instead of considering the full annulus, the samples were put only along $1/3$ (i.e. 120°) of the circle. The layout of the samples is shown in fig.4.2a. The points were placed at an angular distance of 6°, hence there were 20 points per arch for a total of 200 sampling points. At each sampling time step, the three components of the velocity in the wind tunnel frame of reference were stored, leading to a total of 600 values per instant. In order to reduce the effort, these values were sampled every 10 simulations time steps (i.e. $f_{samp} = 200Hz$). From these values the tangential components at each position were obtained rotating the reference system. Therefore, if a generic point j along the arch at radial position i was considered, the induction coefficients were calculated as:

$$\overline{V}_{a_i}^{up}(t) = \frac{\sum_{j=1}^{20} V_{a_{ij}}^{up}(t)}{20}; \overline{V}_{a_i}^{down}(t) = \frac{\sum_{j=1}^{20} V_{a_{ij}}^{down}(t)}{20} ; \tag{4.1}$$

$$\overline{V}_{t_i}^{up}(t) = \frac{\sum_{j=1}^{20} V_{t_{ij}}^{up}(t)}{20}; \overline{V}_{t_i}^{down}(t) = \frac{\sum_{j=1}^{20} V_{t_{ij}}^{down}(t)}{20} ; \tag{4.2}$$

$$V_{a_i}^{D}(t) = \frac{\overline{V}_{a_i}^{up}(t) + \overline{V}_{a_i}^{down}(t)}{2}; V_{t_i}^{D}(t) = \frac{\overline{V}_{t_i}^{up}(t) + \overline{V}_{t_i}^{down}(t)}{2} ; \tag{4.3}$$

$$a_i(t) = 1 - \frac{V_{a_i}^{D}(t)}{V_0} ; \tag{4.4}$$

$$a_{t_i}(t) = -\frac{V_{t_i}^{D}(t)}{\Omega \, r_i} . \tag{4.5}$$

In eq.4.3 the equivalent upstream/downstream distance was used, otherwise the

value at the rotor plane had to be obtained from the equation of the line in fig.4.2b. Latter approach was attempted in unsteady surge simulations, as discussed in Chapter 5. Following the Azimuthal Average Technique, the time histories of the two induction coefficients during steady operations for the different radial positions were extracted. Their plots are shown in fig.4.3. The signals were constant as
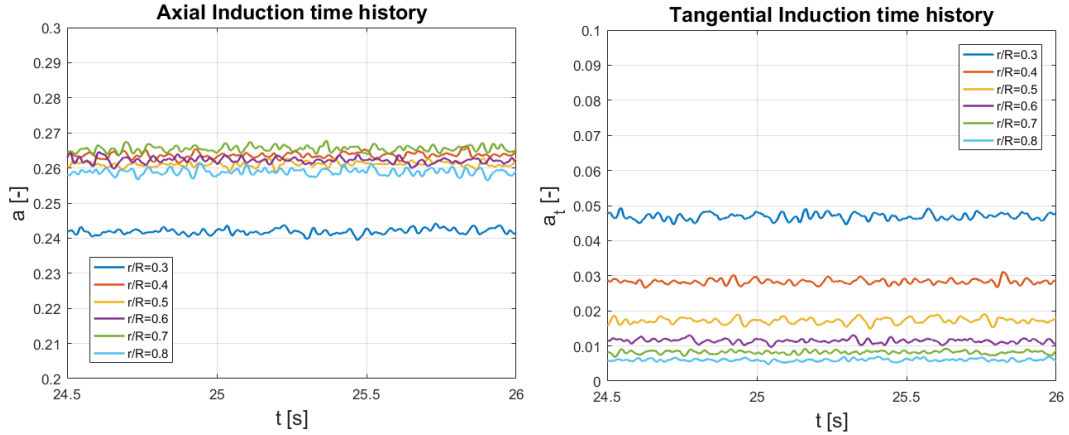
Figure 4.3: axial and tangential induction time histories

expected, with some minor high frequency components superimposed due to turbulent fluctuations. As already stated, the absence of turbulence in the inflow did not mean absence within the domain. Hence, to get the steady distributions of the induction coefficients, their time average values were considered. Such spanwise distributions are reported in fig.4.4. Both the profiles were consistent, proving the effectiveness of the AAT. The tangential induction was small as expected (high TSR). The axial one instead, stood around 0.26-0.27 for most of the span. The reduction visible towards the inner part could have been unphysical because the samples were too close to the root of the blades, likely affected by 3D effects. In general, the limits of the induction extraction method reduced the confidence in the 30% span results.

4.2 Unsteady results

The unsteady tests of the UNAFLOW campaign studied the dynamic response of a turbine undergoing an harmonic surge motion, aimed at reproducing a possible wave induced displacement of a FOWT. The complete unsteady test matrix is reported in Appendix A. For the numerical comparison only RATED2 conditions
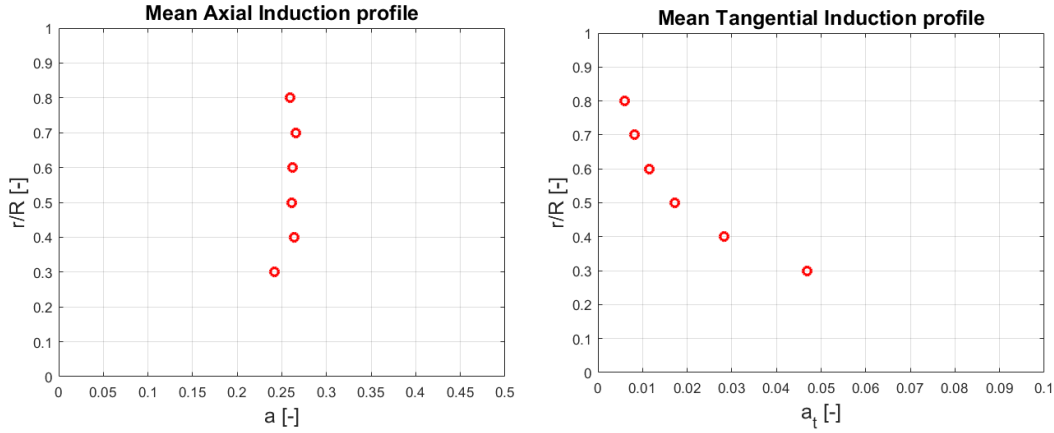
Figure 4.4: axial and tangential induction profiles

were considered. As for the UNAFLOW project, the main focus of the analysis was the thrust force oscillation component at the surge frequency. The reason behind this choice was the leading role that the thrust has in the dynamics of floating turbines. Since typical floating machines are huge, the towers are really tall and the force, applied approximately at hub height, produces a severe pitching moment with respect to the base. Balancing such moment is a compelling task of the floater, ruling the stability of the whole system. The lack of rigid substructure makes the turbine subjected to large displacements, that affect the aerodynamic performance and loads applied. To guarantee the requested stability margins, a robust control strategy must be designed. Being the thrust force the most important player, a reliable FOWT controller cannot prescind from a good modelling of its response to possible (even though simplified) floater movements like the considered surge. In particular, the presence of dynamic inflow phenomena must be investigated since they could jeopardize the stability of these complex systems. In fact, controllers rely on the quasi-static theory to model the thrust response. Should the real behaviour be characterized by unsteadiness, the risks of failure of these machines would be very high. In this context one can understand the outmost importance of both amplitude and phase of the thrust oscillation. Whatever complex control strategy begins by considering Liapunov's stability theorem, i.e. referring to a simple linearized system. Therefore, only the perturbations from equilibrium conditions are relevant, i.e. ΔT. Amplitude and phase of the signal concur to determine the equivalent damping and mass (or stiffness) coefficients, fundamental for controller design.

UNAFLOW #	f_s [Hz]	A_s [mm]
33	0.125	125
37	0.25	125
41	0.5	65
45	0.75	40
49	1	50
50	1	35
51	1	25
53	1.5	20
55	1.5	10
57	2	15
59	2	8

Table 4.2: simulations matrix. **Black** - AL+FVW; **red** - AWSM+BEM; **green** - AWSM+BEM+CFD; **blue** - all codes.

As explained in the introduction to this Chapter, the comparison hereinafter presented includes: 5 numerical codes with different fidelity; experimental data from UNAFLOW employing the new inertia subtraction procedure, choosing the base signal as reference (see Chapter 2); a simple theoretical model based on the quasi-static theory, presented in Section 4.2.1. Both AL and FVW simulations involved nine cases chosen among those of the UNAFLOW matrix at RATED2 conditions. The selected tests are listed in black in tab.4.2. For the CFD simulations instead, USTUTT focused on the two test cases presented in green that were also conducted by TNO in their revised simulations. TNO also added test #33 highlighted in red. This way, most of the original matrix was covered by the different codes.

4.2.1 Simple quasi-static model

Exploiting the quasi-static theory, a reference expression for the thrust force oscillation could be obtained. The procedure followed exactly what it is usually done for the stability analysis of an airfoil, starting from its aerodynamic coefficients. After linearization, an expression for the equivalent aerodynamic damping was found providing a theoretical reference to be used in the comparison. The key asset of this simple formulation is that it only requires the knowledge of the steady turbine operating conditions and characteristic curves. Being purely theoretical then, it can be applied in general to provide an estimate of the thrust force and

power output oscillation. In this work, the focus will only be on the thrust, hence the model will be used to obtain just ΔT. Nevertheless, a theoretical expression for ΔP can also be deduced, just starting from the expression for P instead of T in eq.4.6 and following the same procedure (see Appendix B).

In general, the thrust force of a wind turbine during steady operation can be expressed as a function of the thrust coefficient as:

$$T_0 = \frac{1}{2}\rho A_D\, C_T(\lambda)V_0^2 \; ; \tag{4.6}$$

being the thrust coefficient a function of the Tip Speed Ratio (λ). In case of surge motion, as long as the reduced frequency is small (i.e. absence of dynamic inflow effects) it can be assumed that the induction field around the turbine adjusts immediately to the change in relative wind imposed by the surge movement. Thus, it is still possible to describe the turbine's performance with the quasi-steady 1D model, simply using the expression of the relative wind velocity accounting for the surge motion:

$$V_w(\dot{x}) = V_0 - \dot{x} \; ; \tag{4.7}$$

$$\lambda_w(\dot{x}) = \frac{\Omega\,R}{V_w(\dot{x})} = \frac{\Omega\,R}{V_0 - \dot{x}} \; ; \tag{4.8}$$

$$T(\dot{x}) = \frac{1}{2}\rho A_D\, C_T(\lambda_w)V_w^2 \; . \tag{4.9}$$

To obtain the simple model it is enough to linearize eq.4.9 assuming small surge velocity ($\dot{x} \to 0$) which, in case of harmonic surge, can be translated to a condition on the displacement amplitude ($A_s \to 0$). Thus, using Taylor's expansion truncated at the first order:

$$T(\dot{x}) \approx T_0 + \frac{dT}{d\dot{x}}|_{\dot{x}=0} \; ; \tag{4.10}$$

$$\frac{dC_T}{d\dot{x}}|_{\dot{x}=0} = \frac{dC_T}{d\lambda_w}|_{\dot{x}=0} \cdot \frac{d\lambda_w}{d\dot{x}}|_{\dot{x}=0} = \frac{dC_T}{d\lambda}|_{\lambda_0} \cdot \frac{\Omega\,R}{V_0^2} \; ; \tag{4.11}$$

$$\frac{dT}{d\dot{x}}|_{\dot{x}=0} = \frac{1}{2}\rho A_D[\frac{dC_T}{d\lambda}|_{\lambda_0} \Omega R - 2V_0\,C_T(\lambda_0)] \; . \tag{4.12}$$

Defining:

$$c_0 = \frac{1}{2}\rho A_D[2V_0\,C_T(\lambda_0) - \frac{dC_T}{d\lambda}|_{\lambda_0} \Omega R] = -\frac{dT}{d\dot{x}}|_{\dot{x}=0} \; ; \tag{4.13}$$

finally, the expression for the thrust oscillation and the aerodynamic damping is

obtained:

$$\Delta T(\dot{x}) = T(\dot{x}) - T_0 \approx -c_0 \, \dot{x} = -c_{aero} \, \dot{x} \ . \tag{4.14}$$

In the quasi-static case the aerodynamic damping coefficient is coincident with c_0. But c_0 is a constant, function only of the steady operating conditions of the turbine according to eq.4.13. It is important to note that c_0 is defined as the difference between two positive terms, provided that typical unregulated $C_T(\lambda)$ curves have always a positive slope. While the term $2V_0 \, C_T(\lambda_0)$ tends to stabilize the system providing positive damping, the other $(\frac{dC_T}{d\lambda}|_{\lambda_0} \Omega R)$ has a destabilizing effect; thus it might cause an unstable amplification of the surge oscillations. During normal operations though, $2V_0 \, C_T(\lambda_0) > \frac{dC_T}{d\lambda}|_{\lambda_0} \Omega R$ and the aerodynamic damping is positive. Of course, the $C_T(\lambda)$ curve is heavily affected by the regulation and the choice between regulated and unregulated curve strictly depends on how the wind speed measurement is performed. For example, if the wind velocity is taken from an anemometer mounted on the nacelle, then the measured value will see the variation activating the controller; therefore the regulated curve has to be considered. If, instead, the wind speed is measured from a neighbouring meteorological station, no surge induced variations would be seen and the unregulated curve should be used. As last observation, the quasi-static theory foresees a ΔT signal whose phase is at -90° with respect to the surge displacement (i.e. opposite to $\dot{x}$ with the chosen reference system). Its amplitude then, linearly varies with the surge velocity's amplitude (ΔV). Therefore no aerodynamic mass contribution is expected when the induction field behaves quasi-steadily.

4.2.2 Aerodynamic damping evaluation

In order to use the quasi-static model as a reference for UNAFLOW results comparison, it was necessary to evaluate c_0 for the turbine model tested. All the parameters of eq.4.13 were known for each test, except for the derivative of the thrust coefficient with respect to the TSR. In fact, the scaled model's characteristic curve was not available apart from few points. Moreover, the curve needed was the unregulated one because both the rotational speed (Ω) and the blade pitch (ϑ_p) had been kept constant during surge experiments. To overcome the lack of the model's C_T curve, it was decided to refer to the one of the DTU10MW RWT, provided that the scaled version had been specifically

designed to match the thrust coefficient behaviour. Assuming a perfect similarity, the two curves could be considered coincident. However, the curve available from DTU was of course affected by both pitch and rotor's speed regulation. The latter though, did not change the $C_T - \lambda$ curve since its effect was concentrated in one point, at the optimal Tip Speed Ratio ($\lambda = 7.5$). Blade pitch variations instead, broke the kinematic similarity varying the characteristic curve substantially with respect to the unregulated case. Anyhow, the only zone of interest for RATED2 conditions was that around the optimal TSR. Fortunately enough, in the RWT's C_T curve there were three points in that region almost unaffected by the pitch regulation. Those points have been highlighted in fig.4.5. The respective values of
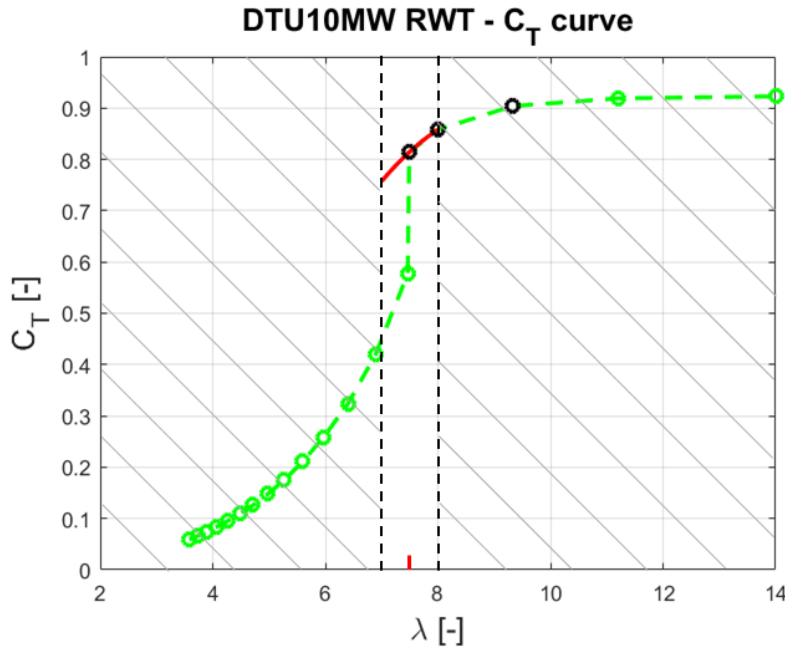
Figure 4.5: extraction of a piece of unregulated $C_T - \lambda$ curve

λ were: 7.5, 8 and 9. To be exact, in the last point the pitch control was already active, but it feathered the blade just around $\sim 0.5^o$; there was no alternative than neglect it. From those three points the $C_T(\lambda)$ curve in that range was approximated with a parabola, thus the term $\frac{dC_T}{d\lambda}|_{\lambda_0}$ could be estimated. Despite some rough engineering assumptions underlay this procedure, the comparison with experimental results was really satisfactory, with average errors well below 10%. This was true for both RATED1 and RATED2 conditions. For ABOVE tests, instead, it was not possible to apply this method since the feathering

regulation was too strong in that TSR range.

4.2.3 Results comparison

Following the same criterion adopted in Chapter 2, the comparison was first performed in terms of thrust oscillation modulus divided by the surge amplitude ($|\Delta T|/A_s$), plotted against the surge frequency (f_s). This way the reference quasi-static behaviour was linear with slope equal to $2\pi c_0$. The results are shown in fig.4.6, where the quasi-static line is represented in yellow. Despite
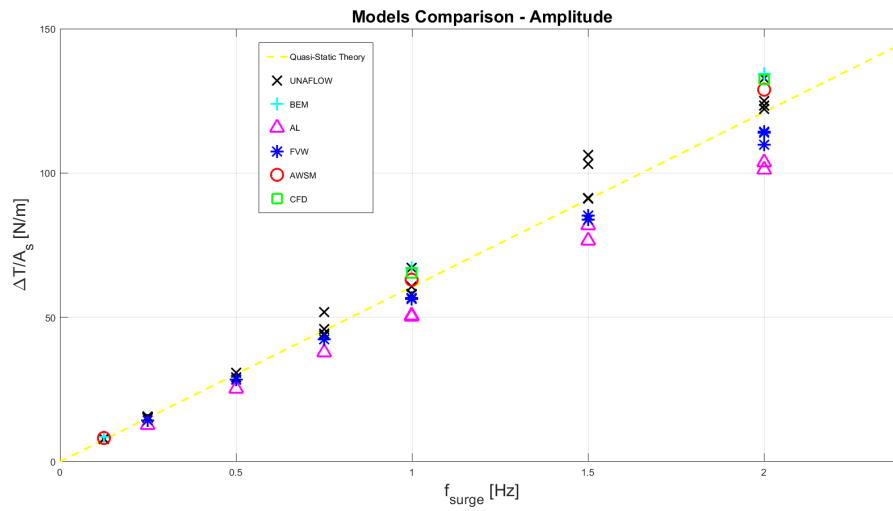
Figure 4.6: UNAFLOW models comparison - thrust oscillation amplitude

the approximations needed for the evaluation of c_0 (Section 4.2.2), the match with the experimental tests was really good. The theoretical approach only seemed to underestimate a little bit the slope, i.e. the aerodynamic damping. This was consistent with what found in steady tests at RATED2, where the thrust coefficient of the model turbine exceeded that of the RWT, used for the estimate of c_0. According to eq.4.13 indeed, a higher $C_T(\lambda_0)$ results in a greater theoretical damping coefficient. Anyway, also the experimental results could be well represented with a simple regression line, witnessing the linearity of the trend regardless the slight scatter. For what concerned BEM, AWSM and CFD results, the differences among their predictions were below 3% on average. All of them provided a slope slightly above the measurements' mean value, but always within the scatter. In particular, the best code in matching wind tunnel tests amplitudes was the AWSM, which went really close to the average experimental trend ($\sim$2%

mean error). Both AL and FVW codes instead, under-predicted the amplitude with respect to measurements and quasi-static theory, with an error very similar to the one made on the steady thrust (tab.4.1). The AL results, for example, were characterized by a linear slope about 15% lower than the experimental one, perfectly reflecting the thrust deficit of the steady case. In the same way, EDF's free vortex code featured a shortfall of $8-10\%$. While the reasons for the FVW discrepancies were clear, a root cause for the AL simulations thrust difference could hardly be guessed. To get the FVW results, in fact, the standard polar data of the SD7032 profile were used since those obtained at DTU within UNAFLOW were not available. Therefore, relevant differences could be expected especially arising from span regions with high attack angles. For AL simulations, instead, the polar data were inserted by Bernini following the DTU campaign. At present, a revision work is ongoing to make sure the same spanwise airfoil characteristics of TNO simulations are used (Appendix C). Although, for the purpose of this Thesis the thrust deficit of AL will be taken for granted and the focus will be put on the trend found rather than the exact values of the amplitudes.
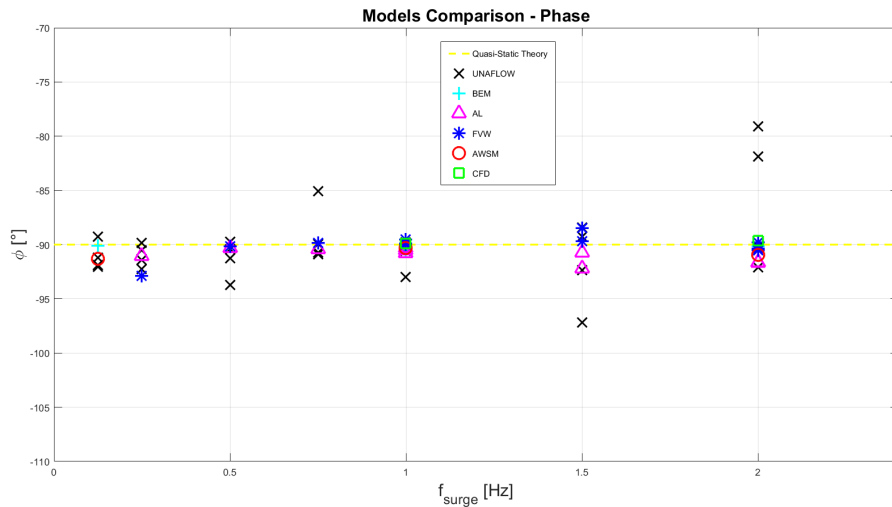
Figure 4.7: UNAFLOW models comparison - thrust oscillation phase

The comparison in terms of phase of ΔT is shown in fig.4.7. The phase was expressed with reference to the surge displacement signal. Therefore, the theoretical quasi-static value was of -90°, i.e. opposite in phase to $\dot{x}$, according to eq.4.14. As explained in Chapter 2, the experimental detection of the exact phase of the thrust oscillation signal was a complex task, owing to the relevant inertia forces involved and the measurement noise. This explained why the scatter of

the wind tunnel values was so relevant. For what concerned the numerical codes instead, the phases were always very close to the quasi-static reference. Some slight discrepancies in the free vortex codes (both FVW and AWSM) were found especially at low surge frequencies. These errors could be ascribed to leakage issues: the time step of those simulations was set as a fraction of the revolution period rather than the surge's. Overall, the agreement among the codes and the theoretical model was excellent; despite their scatter, the experimental data could be assumed to confirm the codes' results.
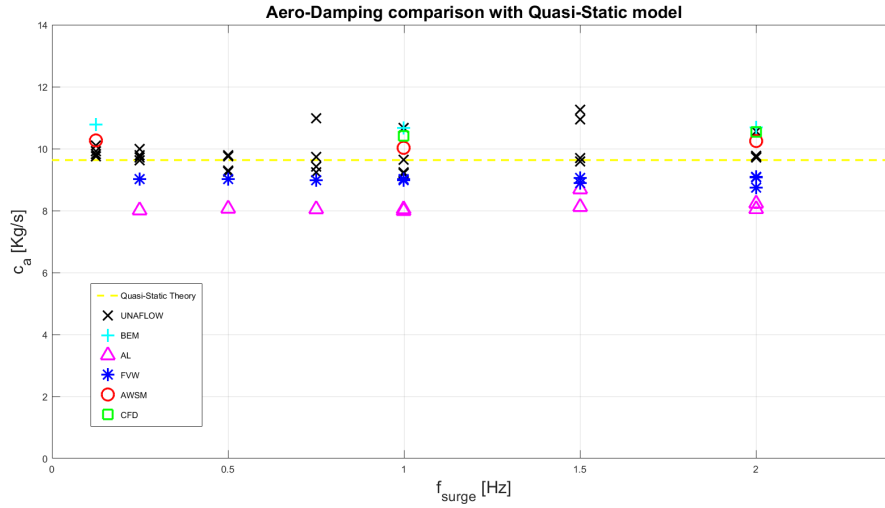
Figure 4.8: UNAFLOW models comparison - aerodynamic damping

Finally, the aerodynamic damping coefficient (calculated with eq.2.7) was considered, again versus the surge frequency. The resulting plot is reported in fig.4.8. For the simple quasi-static model $c_{aero} = c_0$, which was constant with f_s. From latter comparison the same conclusions of the amplitude case could be drawn. The relative differences among codes and measurements are even more clear from this graph. The real aim was to confirm that c_{aero} was almost independent on f_s in this frequency range. Despite some codes were not accurate at spotting the exact values, they all agreed on the constancy of c_{aero}, proving the quasi-linearity of the trends of the amplitudes plot (fig.4.6). This witnessed the validity of the quasi-steady assumption in this frequency range.

4.3   Conclusions

The unsteady tests comparison confirmed the conclusion drawn by de Vaal et al. [62]. The surge oscillations in the most typical frequency range of the sea waves, are not affected by dynamic inflow phenomena. Therefore, the unsteady response is utterly determined with an aerodynamic damping coefficient, independent on the surge oscillation, that can be known a priori from the steady turbine operations as long as the amplitude remains limited (i.e. the linearity assumption does not fall). This observation was confirmed by the revision of the UNAFLOW experimental campaign. The wide effort of code validation also confirmed the capability of current codes of capturing well the unsteady behaviour. After all, the most relevant outcome of this Chapter was the successful use of the simple quasi-static model, which allows to accurately estimate the aerodynamic damping from steady turbine's operating conditions only. The validation of this approach, gives a solid foundation for the design of FOWT controllers. In fact, with such a simple and flexible tool, the unsteady surge response in any possible condition can be fully determined knowing the initial conditions and the characteristic curves. Dynamic effects on both thrust force, for fatigue and stability, and power output, for economical impact and grid stability, can be then easily accounted. For further validation, it would be advisable to obtain the scaled model's characteristic curves experimentally so as to reach a greater accuracy, while being able to use eq.4.13 for c_0 in any operating condition. The great asset of this quasi-static model is that it is valid also in presence of pitch regulation as long as the proper characteristic curve is used; hence, a nice test to confirm its robustness would be to use it in regulated cases where pitch and rpm change during motion. Of course, the use of the steady characteristic curve is appropriate as long as actuation delays are negligible.

Concerning the AL simulations, the steady thrust force deficit in RATED2 conditions affected also the unsteady results, leading to an underestimation of both the aerodynamic damping coefficient and the amplitude of ΔT. This error was systematic and rather constant throughout all the simulations; thus, at least the trends were completely in line with experiments and other codes' results. The phases of the oscillations were also well captured and in promising agreement with the other values. The great match obtained by TNO's codes testifies that, unless a detailed wake analysis has to be performed, the AL is probably not

the most suitable choice in terms of cost-accuracy trade-off. In fact, even if the thrust force had been reproduced better, the great performances of the AWSM would not have justified the computational cost increase for the AL. Nevertheless, the possibility of making observations like that was one of the key purposes of such comparative effort. In this context, it is necessary to underline the outstanding work performed by USTUTT on the full CFD modelling. Despite the tough difficulties in performing high-accuracy simulations on wind turbines, they succeeded in getting extremely precise results even in unsteady conditions. This could only be reached devoting great care to the construction of the grid, to the accurate geometrical reproduction, to the fulfilment of the strict y^+ requirements, and to the choice of all the simulations parameters.

A thorough revision of all the data and models used in the AL code is currently ongoing, to understand the causes of the thrust mismatch. For future improvement, apart from the inclusion of the nacelle in the code expressed in Chapter 3, the Author would suggests to implement the possibility of determining the induction coefficients at each time step with the method proposed by Herráez et al. [63]. This method, in case of uniform axial inflow, consists of sampling the velocity at the disc plane on a line placed half way between two consecutive blades, where the bound circulations balance each other. This way the induction coefficients could be calculated directly from the sampled values, without requiring the cumbersome data processing of the AAT or the need of performing inverse BEM calculations. The implementation would also be very similar to that of the actuator line, since the motion is the same (only the initial position varies) and mesh intersections can be calculated in the exact same way. This simple tool could ease the analysis of dynamic inflow phenomena, earning accurate information on the induction field evolution in time and space.

Chapter 5

Out-of-UNAFLOW Simulations and Dynamic Inflow

The revised comparison of Chapter 4 proved the absence of dynamic inflow effects, at least for a "normal" wave induced surge motion of a FOWT. The maximum frequency considered for the scaled model (2Hz) corresponded to a real scale $f_s = 0.08$Hz, more or less representative of a possible peak in the sea waves' PSD. The lack of unsteady effects was a direct consequence of the narrow frequency band of interest. Therefore, it was decided to investigate the impact of higher surge amplitudes and frequencies, eventually associated to extreme events (e.g. storms). This further step was required to understand the validity borders of the quasi-static model presented in Chapter 4. Filling the knowledge gap in this field would also allow for testing state-of-the-art dynamic inflow models, moving towards more general and flexible approaches. Bearing this in mind, ten numerical simulations out of the UNAFLOW matrix were run, featuring the AL code with the same numerical set up described in Chapter 3. Thanks to the precious cooperation of Corniglion (EDF), all the results of Author's simulations could be compared against those of a FVW code. Once again, the real interest was in unsteady trends more than the absolute values of the quantities. Before entering the unsteadiness field though, the AL code was validated with a traditional dynamic inflow case: the blade pitch step. This way, even if the lack of tests on that specific turbine model hindered a quantitative assessment, the AL's capabilities with dynamic inflow were investigated.

This Chapter is organized in three sections, similarly to Chapter 4. At first, Section 5.1 focuses on a classical dynamic inflow case in which both thrust and

axial induction coefficient responses are analyzed. The results are also provided in non-dimensional form to attempt a comparison with literature. The thrust response to a very fast pitch step is also considered to verify the capturing of the staircase effect. Section 5.2 discusses the core of this Thesis: the out-of-UNAFLOW simulations. A description of the tests selection criteria is given first. Then, the AL simulations results are presented; based on those results, an extension of the quasi-static model accounting for dynamic inflow effects is proposed. Subsequently, the tuning of the model's parameters is performed and the full comparison including FVW results is considered. The Section concludes with the analysis of the extracted unsteady induction behaviour. Finally, Section 5.3 addresses final comments and conclusions.

5.1 Dynamic inflow: pitch steps

All the traditional literature concerning wind turbines' rotor unsteadiness is focused on fast load changes. As discussed in Chapter 1, the induction field reconfiguration occurs with a delay producing instantaneous load overshoots (or undershoots). This phenomenon was referred to as dynamic inflow. The sudden load changes typically reproduced high gain controller effects, like sharp blade pitch variations (e.g. emergency feathering) or rpm adjustments in variable speed rotors. In theory, these loading peaks could affect the fatigue life of such machines; thus, several engineering models allowing BEM codes to account for them were developed. In reality, if the controller is properly tuned, the real extent of this unsteadiness is low, as it is the impact on the fatigue life. Therefore, the concrete driving forces for the research were the pure aerodynamic comprehension and the challenge of numerical reproduction of dynamic effects. Lately, a broader picture of this induction delay is being depicted, investigating also alternative triggering mechanisms such as sudden wind gusts. As a result, the term dynamic inflow has assumed a wider meaning; it is not solely linked to blade pitch (or rpm) steps, but it refers to the general induction field unsteadiness, no matter what causes it. In this context, the presence of eventual induction delays due to the surge motion in FOWTs could be deemed dynamic inflow matter too. Latter inspection was the core of this Thesis and it will be presented in Section 5.2. However, before considering unconventional cases, it was necessary to validate the AL code with classical problems first. Thus, a preliminar analysis of the responses of both thrust

force and induction field to a steep ϑ_p variation was conducted. Unfortunately though, pitch step tests on the UNAFLOW turbine have not been performed yet. According to funding and availability of the wind tunnel, they may be carried out only after the end of this work. Without experimental data on this specific case, the assessment had to remain rather qualitative, also owing to the lack of a thorough non-dimensional description of classical dynamic inflow parameters. In fact, literature results were often provided in dimensional forms because of the difficulties in finding a more general representation. One of the main causes was the large number of independent parameters involved. The time constants associated with the induction/thrust responses, for example, depend on both the initial operating conditions and the characteristics of the pitch step itself. This, together with the limited amount of experimental data available, hindered the realization of a reference non-dimensional analysis allowing to compare outcomes of different tests and turbines. The pursuance of a similar aim would have required a specifically devoted work and could not be included in the scope of this Thesis.

In order to study the classical dynamic inflow behaviour, the very same numerical set up of the surge simulations was adopted. Again, to be consistent, the pitch steps were performed in RATED2 conditions and the Azimuthal Average Technique described in Chapter 4 was used to extract induction. The amplitude of each pitch step was set to $\Delta\vartheta_p = 6^o$, following Berger and Kühn [31] who performed an experimental campaign on a similar scaled model in Oldenburg. Both forward, i.e. from 0° to 6° (unloading), and backward, i.e. from 6° to 0° (loading), steps were considered. This way, a generic blade feathering actuation was reproduced, while ensuring that most of the blade always worked in attached flow conditions for AL accuracy. Forward and backward pitch steps were repeated consecutively, with a rest period of 2.5s (about 10 revolutions) in the middle, to allow the re-establishment of steady-state conditions. Each step was repeated four times and the ensemble averaged response was then considered to clean the signal from turbulent oscillations. Having neglected inflow turbulence, four repetitions proved to be enough to obtain a satisfactory outcome. To account for the finite actuation time the steps were approximated with a constant regulation velocity ($\dot{\vartheta}_p$); no smoothing of the extreme points was employed since the numerical code did not require it. Two different values of $\dot{\vartheta}_p$ were selected. The choice was made looking at the ratio between the time needed to complete the pitch step and the period of a rotor revolution. In particular, the first actuation velocity was chosen

to have $t_p/T_{rev} \cong 0.5$, which was intermediate between the values of NASA Ames ($\sim 30\%$) and New Mexico ($\sim 100\%$). This resulted in $\dot{\vartheta}_p = 48^o/s$ for the *standard* step. The second speed selected was much higher, to investigate the occurrence of the staircase effect reported in Mexnext III [16]. The t_p/T_{rev} ratio was reduced to $\sim 10\%$ resulting in a $\dot{\vartheta}_p = 240^o/s$ for the *fast* step. The two pitch time histories are shown in fig.5.1.
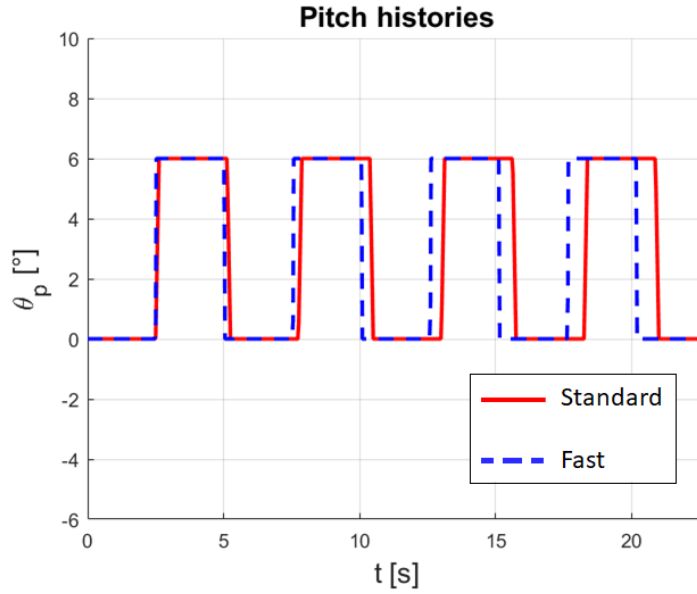
Figure 5.1: pitch steps time histories

5.1.1   Thrust response

Seeking a clever way to express the thrust force in non-dimensional form, it was decided to follow a common formulation that seemed the most robust among those available in literature. The nicest feature of this approach was that it referred both undershoots and overshoots to a unique value, i.e. the steady-state thrust variation. In particular, T^* was expressed as:

$$T^*(t) = \frac{T(t) - T_0}{T_0 - T_6} \ .\tag{5.1}$$

For the standard step case, the resulting response is shown in fig.5.2 where the presence of dynamic inflow effects is clearly visible. In particular, a thrust undershoot was generated by the forward step (unloading), while an overshoot

followed the backward one. Thanks to the ensemble averaging procedure, the signal presented only weak residual disturbances due to turbulence. Before the start of a subsequent step, the thrust reached its steady-state value confirming the appropriate selection of the rest period.
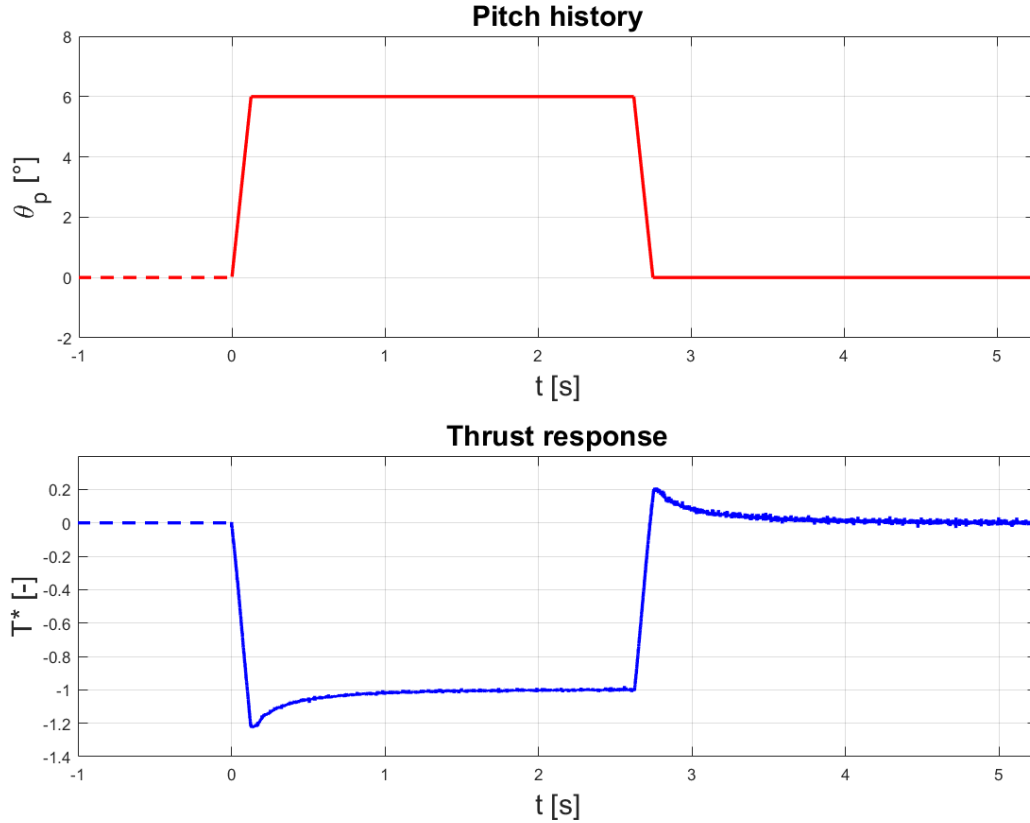
Figure 5.2: ensemble averaged thrust response

The first interesting parameter to be analysed was the amount of overshooting (or undershooting) with respect to the quasi-static thrust variation. Literature showed that the size of the overshoot in backward steps is typically lower than the undershoot in forward ones. The reason behind this evidence is the higher initial induction coefficient before the upward step. A higher axial induction indeed, means a slower near wake convection velocity -usually quantified as $V_0(1-1.5a)$- resulting in a longer initial part of the induction field reconfiguration. For what explained in Chapter 1, a slower wake means that the old vorticity takes longer to move farther; hence, the initial change of the induced velocity is slow. This produces a more pronounced load variation from the steady-state value. Conversely, the second part of the wake development is faster for the

upward step, since the axial induction reduces and the wake convects quicker. The AL simulations confirmed this behaviour: the forward step produced an undershoot of 22.87% with respect to the difference between the steady-state values (i.e. $T_0 - T_6$); the backward one instead, resulted in a crest of 21.16%. The difference was slighter than what typically found, probably owing to the limited rotor loading variation.

Traditionally, the thrust response (but also torque's or flapwise moment's) was modelled with an exponential behaviour characterized by a single time constant τ. This model was originally developed by ECN for the Tjæreborg turbine [22]. The value of τ was evaluated from the decay part of the thrust time history and it was then linked to the induction field evolution. Hence, the thrust response had to be known to estimate the time constant. The decay after the peak was exponential indeed, but the associated time parameter progressively varied with the wake development. Therefore, considering τ as a constant involved a certain degree of approximation. Despite the necessity of more accurate models (at least with two constants) is now commonly accepted, its simplicity and its long usage history make the single constant analysis the most popular way to compare with traditional dynamic inflow results. Therefore, that approach was followed. First, the time varying τ for forward and backward steps were evaluated as:

$$\tau_{Forw}(t) = -\frac{t - t_{und}}{\log\left(\frac{T_6 - T(t)}{T_6 - T_{und}}\right)} \; ; \qquad \tau_{Back}(t) = -\frac{t - t_{ov}}{\log\left(\frac{T(t) - T_0}{T_{ov} - T_0}\right)} \; . \qquad (5.2)$$

As well-known from literature, eq.5.2 are only valid when t is above the peak (either overshoot or undershoot), but before the steady-state value is reached; otherwise meaningless values arise from indeterminate forms of the mathematical expression. The choice of the evaluation intervals were made in order to avoid those meaningless values. Both $\tau_{Forw}(t)$ and $\tau_{Back}(t)$ had an increasing trend, confirming that the initial dynamics causing the peaks was faster than the following part. Although, to extract a single reference value the average of the signals had to be taken:

$$\tau_F = \overline{\tau}_{Forw}(t) = 260ms \; ; \qquad \tau_B = \overline{\tau}_{Back}(t) = 268ms \; . \qquad (5.3)$$

Using these values and inverting eq.5.2, the approximated expressions for the thrust force time histories could be obtained. In fig.5.3 are shown the comparisons

among the thrust responses. Despite the simplicity of the model, the fit was rather good in both forward and backward cases.
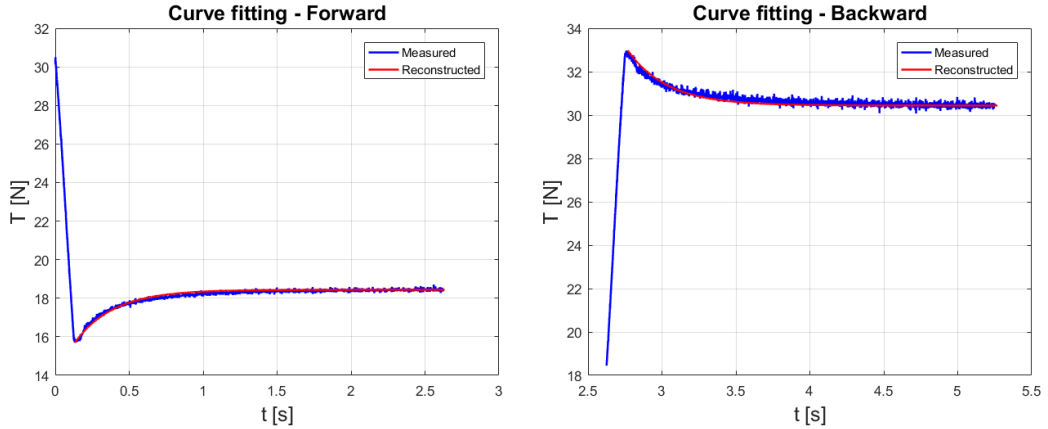
Figure 5.3: thrust responses and single time constant model approximations

In terms of dimensional values, the two constants were smaller than those of larger turbines found in literature, resembling a little those obtained by Berger and Kühn on a similar scale model [31]. The backward constant was slightly higher than the forward, meaning that the second (slower) part of the decay was prevailing over the initially fast dynamics. This, though, depended strictly on how long was the time considered after the overshoot: the greater the interval the larger the difference, since more importance was given to the second part of the response. Dimensional values were useless to compare with traditional experiments on larger diameters turbines. However, as previously anticipated there is not yet a common agreement on how to make the results non-dimensional. The simplest possibility was to consider the undisturbed wind velocity and the diameter $\tau^* = \tau V_0/D$. Despite this was the most popular approach, it did not take into account the turbine loading which was fundamental for the dynamic response. To account for that, Sørensen and Madsen [64] proposed to use the wake convection velocity instead of the free stream one, i.e. $\tau^{**} = \tau V_0(1 - 1.5a)/D$; this way at least the information on the steady-state turbine loading was provided by the induction factor. Even with this approach the generalization of the time constant was impossible, because there was no information on the step size for example. Furthermore, several traditional tests considered cases in which considerable parts of the blades were stalled or with the turbine operating in turbulent wake state. This made the quantitative assessment of the obtained

AL results inconceivable without specific wind tunnel tests. Then, only some qualitative range comparison could be performed. The values corresponding to the two different adimensionalization strategies are reported in tab.5.1.

	τ [s]	$\tau^* = \frac{\tau V_0}{D}$	$\tau^{**} = \frac{\tau V_0 (1-1.5a)}{D}$
Forward	0.26	0.437	0.345
Backward	0.268	0.45	0.275

Table 5.1: thrust time constants for forward and backward steps

Focusing on τ^*, the values found for the Tjæreborg turbine were in the range 0.3-0.5 while for the TUD ⌀1.2m model they were within 0.4-0.68. To be exact, those constants were referred to the flatwise bending moment; although, the differences with those of the thrust are known to be rather small. In NASA Ames experiments, τ^* values for the thrust force in the spanwise range 0.3R-0.95R were found to go from 0.39 to 0.77. Finally, Berger got a τ^* for the thrust force equal to 0.51 for the upward case and 0.63 for the backward. The values found by the AL fell within these ranges and respected the main know trends, allowing to believe them to be at least likely estimates.

5.1.2   Induction field

To complete the analysis, the behaviour of the induction field at five radial locations (0.3,0.4,0.5,0.6,0.7,0.8)R was obtained with AAT (Chapter 4). For comparing the different responses, they were rescaled so as every one of them went from 0 to 1 and vice versa. Thus:

$$a^*(t) = \frac{a(t) - a_6}{a_0 - a_6} \ .$$
(5.4)

The resulting time histories are plotted in fig.5.4. Despite the expected quasi-exponential trends were found, the radial variation of the time constant did not match the typical weak reduction towards the tip in the forward step. Except for the signal at 30% of the span, which showed a much slower dynamics than the others, the rest did not present a clear pattern with the radius. For the forward step, indeed, the curves from 40% to 80% of R were all close to each other and the expected faster dynamics of the tip could not be recognized. In the backward case instead, a stronger radial variation was there but, once again,

there was not a monotonic trend of the time constant with the radius; the 0.4R and 0.8R histories were slower than those in the middle in fact. The 0.3R curve was the only one markedly different than the others but it was also the one with the lowest confidence associated, because of the vicinity with the root section. Despite their promising time histories, the axial induction coefficients extracted
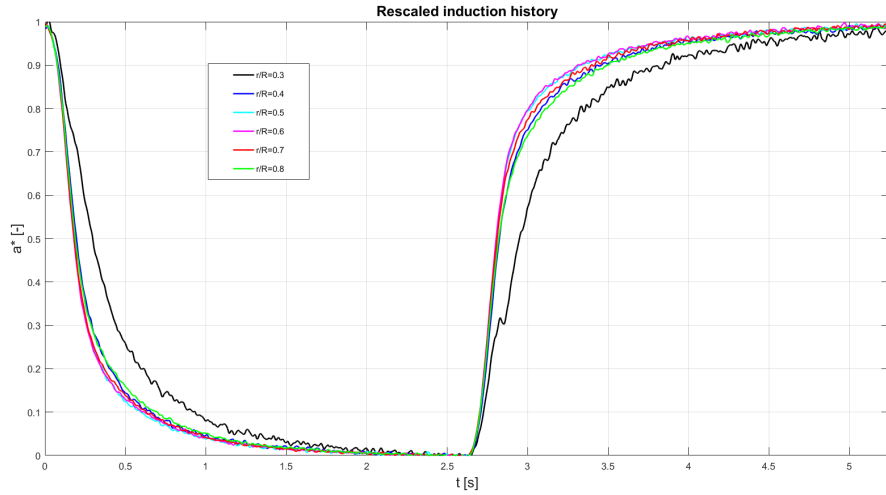
Figure 5.4: rescaled axial induction time histories

with the Azimuthal Average Technique did not seem to be in full agreement with literature results. From historical data one would have expected to find a monotonic (even if weak) dependency of the induction time constant with the radius: slightly reducing in forward steps and opposite in backward. In reality though, the variability of such results has always been rather high and strictly dependent on the analyzed conditions. Then, even though some doubts on the accuracy of these results aroused, it might be unwise to draw conclusions without having specific experimental data to compare with.

5.1.3   Fast step: staircase effect

Being momentarily constrained to a qualitative comparison, it was deemed interesting to test whether the code was capable of getting the staircase effect described in [16]. This name was given by the thrust response who showed some clear steps (like a stair) in the decay after the peak. Such phenomenon was found by CFD and free vortex codes considering fast pitch steps for the AVATAR turbine. Although it was found only numerically, it had a strong physical meaning.

In fact, each step width had approximately the size of 1/3 of the revolution period. Therefore, the cause was the finite number of blades. Basically, when the pitch regulation is very fast and a blade travels through the zone which has already been perturbed by the load change of the precedent blade, a sudden discontinuity is felt, causing a step in the thrust response. This effect starts during the first revolution and tends to disappear after some time, when the induction field redistribution becomes azimuthally even. Unfortunately, it would be very difficult to observe it experimentally, provided that several disturbances from both turbulence and structural vibrations are always present. Moreover, unrealistically high actuation velocities would be required.
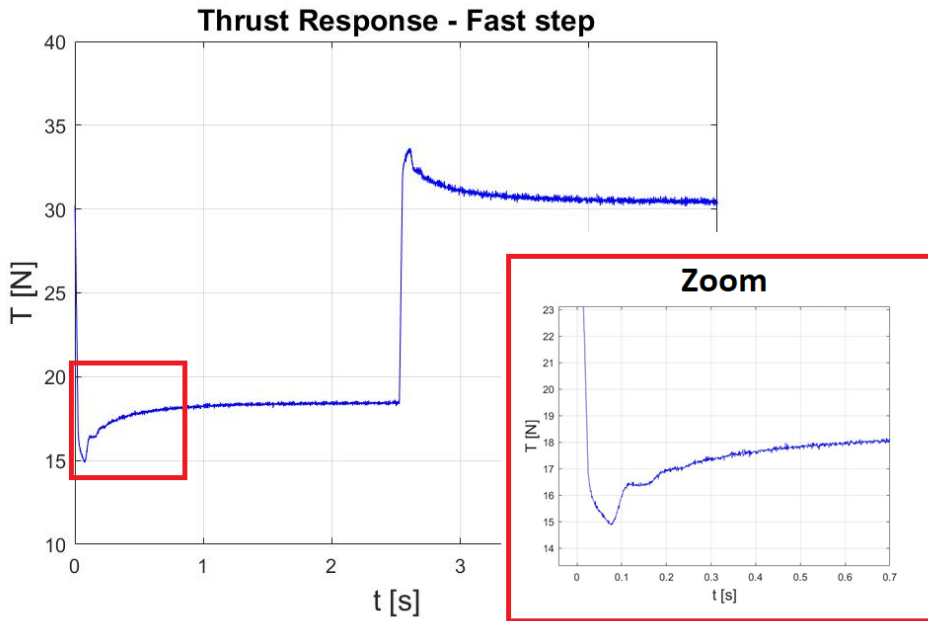
Figure 5.5: thrust response to fast pitch step and staircase effect

To spot the presence of a staircase effect, a faster pitch regulation velocity was imposed ($\dot{\vartheta}_p = 240\,^o/s$) so as to have $t_p/T_{rev} \cong 10\%$, close to the value of 7.3% of the AVATAR turbine case. The resulting thrust response, in fig.5.5, confirmed the capability of the AL code to capture also this phenomenon. The first two steps were recognizable and had a width of 0.085s approximately, which was exactly 1/3 of the revolution period. This simple test case increased the confidence in the reliability of the unsteady results drawn from the AL code in absence of an experimental counterpart.

5.2   Out-of-UNAFLOW surge simulations

Dynamic inflow effects have a limited influence on bottom-fixed wind turbines'
lives. In fact, loads overshoots/undershoots remain limited if the actuation
velocity (strictly linked to controller's gains) does not exceed certain values. In
floating turbines instead, dynamic inflow phenomena may potentially cause the
catastrophic failure of the system. In those machines indeed, aerodynamic loads
not only have an impact on fatigue life, but they also affect the overall stability of
the system (turbine+floater). Variances, of thrust especially, from the quasi-static
theory would produce unexpected excitations that might reduce the system's
stability margins. In fact, due to the limited number of studies in this direction,
FOWTs controllers are based on the assumption of quasi-steady loads, without
being fully aware of the limitations concerned. The large motions associated
to floating machines may trigger several unsteady effects. Dynamic inflow is
likely the most critical among them, since it occurs at full rotor scale and it
might generate relevant force deviations. This is a large opportunity for unsteady
aerodynamic research, since it sheds new interests in the dynamic inflow field and
it might finally lead to a comprehensive understanding of the phenomenon. The
Author firmly believes in the tight link among dynamic effects caused by sudden
load changes (e.g. blade pitch steps), wind variations (e.g. gusts) and turbine
motions (e.g. surge or turbine pitch). Therefore, once a deep investigation is
performed, possibly in non-dimensional terms, a full synthesis might be found
and an holistic dynamic inflow model valid for all the cases could be developed.

With that purpose in mind, a first step was to complete the study on the surge
motion response started with UNAFLOW. At the beginning of the experimental
campaign, it was a fairly common opinion that at least some of the tests would
have shown traces of dynamic inflow. Instead, the results obtained were almost
free of any unsteady effect and agreed surprisingly well with the quasi-steady
theory (Chapter 4). Although, it was expected that increasing the amplitude of the
surge velocity (ΔV) some influence of the induction lag would have been visible.
This brought the will to investigate what happened changing ΔV, by acting
on either the surge amplitude or frequency. The rather good agreement found
among AL simulations and UNAFLOW wind tunnel data, exception made for the
systematic thrust deficit, posed the grounds to continue using the numerical set
up of Chapter 3. From the AL results obtained (Section 5.2.2), a semi-empirical

extension of the quasi-static model was developed (Section 5.2.3 and 5.2.4) to account for the unsteady effects in a simple way. Finally, with availability of the FVW simulations a comparative analysis could be performed confirming the main trends found (Section 5.2.5).

5.2.1   Simulations matrix selection

Great care was taken in order to appropriately select the parameters of the out-of-UNAFLOW matrix simulations. In particular, the new surge amplitudes (A_s) and frequencies (f_s) had to guarantee a sound physical consistency. For this reason, three main constraints were set:

1. $\boldsymbol{f_s \leq 6Hz}$: the maximum surge frequency had to be still representative of a possible component of the sea spectrum. Due to the scale, a factor 25 distinguished model's frequency values from real ones, i.e. f_{s-real}^{max} =0.24Hz. This value did not correspond to a typical peak in the sea waves' PSD, but it was close enough to represent an event with lower return time than what prescribed by design standards.

2. $\boldsymbol{f_{red}^{airfoil} \leq 10\%}$: the airfoil reduced frequency had to remain below 10%, to preserve the validity of the quasi-static airfoil theory used to calculate the blade forces in AL simulations.

3. $\boldsymbol{\Delta\alpha \leq 4^o}$: the AoA variation due to surge motion lower than 4° above 30% of the span to avoid stall and dynamic stall effects that would have compromised the accuracy of the simulations.

The last constraint came from the observation of the steady angle of attack distribution along the blade, extracted from the AL simulation in RATED2 conditions and shown in fig.5.6a. From the airfoil's 2D data gathered in UNAFLOW, profile's stall occurred around α =12°; hence, if $\Delta\alpha$ was greater than 4° most of the blade span would have risked to stall, compromising polars accuracy. Note that the very high values at the root were not significant, because the section was cylindrical there and it was modelled by a constant C_D value.

In order to estimate the amplitude of the angle of attack variation caused by the surge motion, the assumption of constant induced velocities was made. This hypothesis allowed to simplify considerably the calculation and it was justified by the belief that the induction coefficient oscillation was in phase with the surge

(a) AoA along the span in RATED2   **(b)** $\Delta\alpha$ estimation
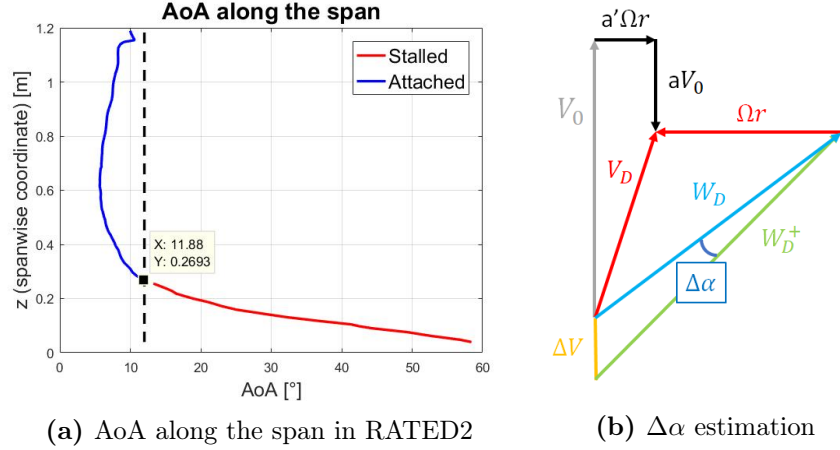
Figure 5.6: steady angle of attack and its variation

velocity (according to the reference system chosen). When the relative wind velocity increased because the turbine was moving towards the wind ($\dot{x} \leq 0$), the induction coefficient reduced because the wake was moved farther. As soon as no delay was there (quasi-static), the axial induction decrease tent to keep the induced velocity almost constant. Tangential induction variations were considered absolutely negligible. Thanks to these assumptions, only the steady induction coefficients' spanwise distributions were required; they were obtained interpolating from the values showed in fig.4.4 (Chapter 4). Provided that the blade pitch was kept constant during surge, the α variations were equal to the flow angle variations. In fig.5.6b the resulting velocity triangle at a generic radial location is reported, assuming 2D flow. With the hypothesis of constant induced velocity, the impact of ΔV on the relative velocity at the rotor plane is soon noticed. Consequently, $\Delta\alpha$ could be evaluated as:

$$\Delta\alpha = cos^{-1}\left(\frac{\mathbf{W}_D \cdot \mathbf{W}_D^+}{W_D \, W_D^+}\right) ; \tag{5.5}$$

$$\text{with: } \mathbf{W}_D = (1-a)V_0 \, \hat{\mathbf{a}} - (1+a_t)\Omega r \, \hat{\mathbf{t}} ; \tag{5.6}$$

$$\text{and: } \mathbf{W}_D^+ = [(1-a)V_0 + \Delta V] \, \hat{\mathbf{a}} - (1+a_t)\Omega r \, \hat{\mathbf{t}} . \tag{5.7}$$

The resulting spanwise distribution of the angle of attack's oscillation amplitude induced by the surge motion is reported in fig.5.7a. In particular, the plot shown was obtained for the worst case, i.e. the maximum considered $\Delta V = 0.754 m/s$ ($\sim$20% of V_0). Even in that case, stall was prevented along the most relevant part of the blade. To guarantee the appropriate use of the airfoil's quasi-

85

(a) α variation amplitude

(b) Airfoil reduced frequency
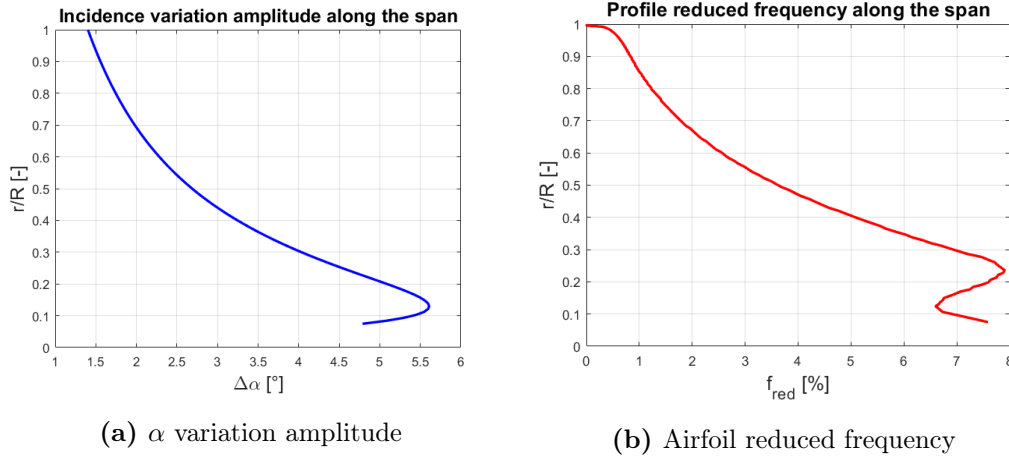
Figure 5.7: spanwise profiles of $\Delta\alpha$ and $f_{red}^{airfoil}$ in the worst cases

out-of-UNAFLOW #	f_s [Hz]	A_s [mm]
1	2	30
2	2	60
3	4	30
4	2.5	30
5	2.5	48
6	3	30
7	3	40
8	4	20
9	5	24
10	6	20

Table 5.2: out-of-UNAFLOW AL simulations matrix

static polars, also a check on the profile's reduced frequency was made. The importance of this parameter was discussed in Chapter 1. Here only its expression is recalled: $f_{red}^{airfoil} = f_s c / W_D$. Also in this case, the values varied with the radial position, giving rise to the distribution reported in fig.5.7b, for the maximum surge frequency case. In the evaluation of $f_{red}^{airfoil}$ the steady (or mean) value of W_D was used, simply taking the amplitude of eq.5.6. The peak reduced frequency was about 8%; from 0.4R till the tip the values were even below 5%. This confirmed the different time scales between airfoil's and rotor's unsteadiness, removing any concern on the use of quasi-steady aerodynamic coefficients.

Having guaranteed the weakness of all the other sources of unsteadiness, any discrepancy with respect to the quasi-static theory could be univocally ascribed

to dynamic inflow effects. As explained in Chapter 1, dynamic inflow is a rotor unsteadiness whose time scale can be quantified as D/V_0. Just like in the unsteady airfoil theory, the ratio between that time scale and the one of the motion (in this case surge) gives rise to a non-dimensional parameter that quantifies the importance of the unsteady effects. In this work, consistently with the treatment of the airfoil, a reduced frequency is hence defined as: $f_{red} = f_s D/V_0$. The higher its value, the greater the impact of dynamic inflow phenomena. It is worth to notice that this parameter is exactly the inverse of the reduced velocity defined by Bayati et al. in [65]. Having constrained the maximum surge frequency to 6Hz, the maximum reduced frequency was $f_{red}^{max} =3.57$. In conclusion, the 10 new simulations of the out-of-UNAFLOW matrix are listed in tab.5.2. The cases highlighted in red share all the same $\Delta V = \Delta V_{max}$, obtained with different combinations of A_s and f_s to study the influence of those two parameters. All the tests were conducted with both AL (by the Author) and FVW code (by Corniglion), always in RATED2 conditions. Simulations number 3 and 10 were also repeated with a reduced time step to investigate the impact of the AL's explicit formulation.

5.2.2 Actuator Line results

The results of the Actuator Line simulations, in terms of amplitude and phase of the thrust oscillation at different surge frequencies, are reported in fig.5.8. Two
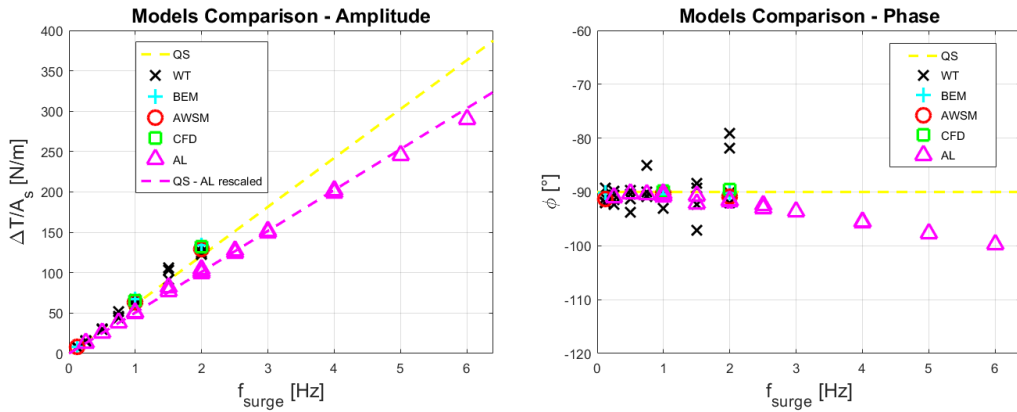
Figure 5.8: AL results - amplitude and phase of the thrust oscillation

main trends could be recognized. The clearest was the behaviour of the phase of ΔT, which progressively departed from -90° going towards -100°, as soon as f_s

was increased. Such delay perfectly resembled dynamic inflow phenomena since it could result from a delay in the induction field reconfiguration. Analysing the trend, a very good fit was found with a negative concavity parabola having its maximum in the origin (Section 5.2.4). In parallel to this phase shift, another less pronounced effect was spotted on the amplitude. In order to highlight such trend the value of c_0 found by the AL simulations, instead of the theoretical one, was used to rescale the slope of the quasi-static model. In the amplitude plot of fig.5.8, this rescaled slope is shown. A slight thrust oscillation amplitude reduction could be be recognized at the highest frequencies. Such a trend, albeit weak, could have a link with the loads amplitudes reductions recently found by Berger et al. [32] in sinusoidal wind experiments. However, they found a $|\Delta T|$ reduction of 16% already at 1Hz, while in this surge case the maximum reduction was around 5% at 6Hz. This much lower impact could be hardly explained solely by the lower ΔV (20% vs 30%) or the different turbine. Therefore, a strong interest to elaborate on similarities and differences between the surging turbine and the varying wind was born.
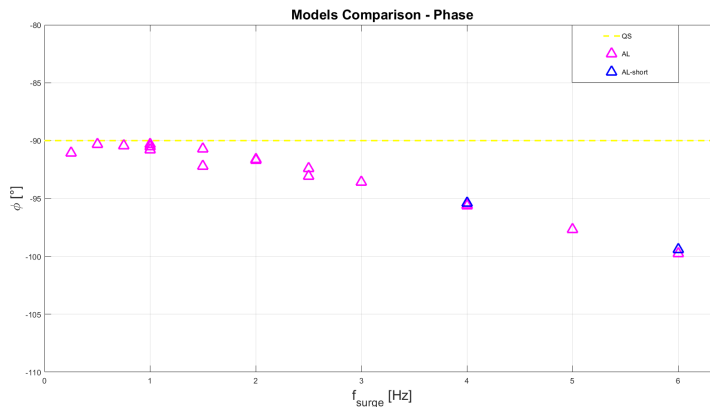
Figure 5.9: effect of the time step size on the phase delay

The explicit formulation of the AL solver, poured some concerns on the reliability of the values of the phase delays. In fact, provided that the force was calculated from the velocity field of the previous time step, this could have been a possible source of delay. The resulting phase shift could be, in principle, quantified as $\Delta\phi[^o] = 360^o f_s \Delta t$; this was not totally correct though, because while the flow field velocity was from the previous step, the turbine velocity was run time. Anyway, to spot the influence of this source of delay it was decided to run two additional simulations with a five times smaller time step (i.e. $\Delta t = 0.0001$s).

The cases chosen were #3 and #10 and the outcomes of these tests are shown in fig.5.9. It was clear that, despite a minimum phase increase was present, it did not change substantially the trend obtained.

5.2.3 Extended quasi-static model

The unsteadiness found in the out-of-UNAFLOW AL simulations could not be modelled with the quasi-static model described in Chapter 4. Even if the extent was rather limited in the frequency range considered, the will of finding a simple representation for those dynamic effects was high. Owing to the simplicity and accuracy of the simple model at low f_s, it was decided to start from that formulation, trying to find some corrections to fit the high frequency behaviour. This way, its nature of simple yet effective tool for preliminar controller design could be preserved. To keep the accuracy in the UNAFLOW range, the corrections had to act progressively depending on f_s. To account for both the amplitude reduction and phase delay effects, two empirical parameters were added to the original model, namely: the amplitude reduction coefficient (β) and the phase shift (φ). These corrective coefficients were both expressed as functions of the turbine reduced frequency ($f_{red} = f_s D/V_0$) to keep as much generality as possible; for a leaner notation latter dependency will be implied. Despite having purely empirical expressions, the parameters' physical meaning was clear. Surprisingly, dynamic inflow effects could be faithfully reproduced as they acted on the surge velocity signal felt by the turbine:

$$V_w(\dot{x}) = V_0 - \beta\,\dot{x}\,e^{-\mathbf{i}\,\varphi} \; ; \tag{5.8}$$

$$\lambda_w(\dot{x}) = \frac{\Omega\,R}{V_w(\dot{x})} = \frac{\Omega\,R}{V_0 - \beta\,\dot{x}\,e^{-\mathbf{i}\,\varphi}} \; ; \tag{5.9}$$

$$T(\dot{x}) = \frac{1}{2}\rho A_D\,C_T(\lambda_w)V_w^2 \; . \tag{5.10}$$

Basically, as the surge frequency increased, the amplitude of the relative velocity signal (V_w) was reduced and its phase was shifted. After having introduced β and φ in eq.5.8, the same procedure of the original model was followed. Thus, eq.5.10 was linearized assuming $A_s \to 0$ leading to:

$$T(\dot{x}) \approx T_0 + \frac{dT}{d\dot{x}}|_{\dot{x}=0} \; ; \tag{5.11}$$

$$\frac{dC_T}{d\dot{x}}|_{\dot{x}=0} = \frac{dC_T}{d\lambda_w}|_{\dot{x}=0} \cdot \frac{d\lambda_w}{d\dot{x}}|_{\dot{x}=0} = \frac{dC_T}{d\lambda}|_{\lambda_0} \cdot \frac{\Omega\,R}{V_0^2} \cdot \beta e^{-\mathbf{i}\,\varphi} \; ; \qquad (5.12)$$

$$\frac{dT}{d\dot{x}}|_{\dot{x}=0} = \frac{1}{2}\rho A_D[\frac{dC_T}{d\lambda}|_{\lambda_0}\,\Omega R - 2V_0\,C_T(\lambda_0)] \cdot \beta e^{-\mathbf{i}\,\varphi} = -c_0 \cdot \beta e^{-\mathbf{i}\,\varphi} \; . \qquad (5.13)$$

Therefore, the thrust oscillation could be expressed as:

$$\Delta T(\dot{x}) = T(\dot{x}) - T_0 \approx -c_0\,\beta\,\dot{x}\,e^{-\mathbf{i}\,\varphi} = -c_{aero}\,\dot{x} - m_{aero}\,\ddot{x} \; ; \qquad (5.14)$$

with:

$$c_{aero} = c_0 \cdot \beta\cos\varphi \; ; \qquad (5.15)$$

$$m_{aero} = -c_0 \cdot \frac{\beta\sin\varphi}{2\pi f_s} \; . \qquad (5.16)$$

The response was exactly the same as the simple model, only this time the surge velocity signal was rescaled by β and shifted in phase by φ. The ruling parameter was still the quasi-static damping coefficient c_0, always expressed by eq.4.13, depending only on turbine's steady operating conditions. However, with the introduction of β and φ, that term did not correspond anymore to the aerodynamic damping coefficient. Indeed, c_{aero} was now expressed by eq.5.15, involving both the semi-empirical coefficients. In particular, the factor $\beta\cos\varphi$ reduced the aero-damping with the surge frequency, meaning that $c_{aero} \leq c_0$. This reduction would unlikely cause problems in normal operations, when the quasi-static damping is rather high. Although, when the turbine is operated far from the optimal TSR and damping is low, a further reduction caused by dynamic inflow effects could affect the system's stability margins. With the theoretical expression of c_0, if the $C_T(\lambda)$ function is known, a simple optimization problem could be built-up seeking the most critical points, i.e. those at minimum c_0.

Another peculiarity of this extended model was the appearance of an aerodynamic mass term, besides c_{aero}, in the expression of the thrust oscillation (eq.5.13). In fact, having included the delay caused by dynamic inflow, the thrust oscillation was not in opposition of phase with $\dot{x}$, that is at -90° with x. This caused the birth of a component in phase with $\ddot{x}$. The expression for such m_{aero} is given in eq.5.16. Also this component was strictly dependent on the quasi-static aerodynamic damping. It is important to notice that if $c_0 > 0$, this aerodynamic mass term is always negative. Therefore, in a simplified linear equilibrium equation for the

FOWT in the surge direction, it would have acted as a reduction of the system's inertia. Even if this seemed a bit counter-intuitive, it was a direct consequence of the delay in the thrust oscillation signal. Nevertheless, the size of this component was very small in all the frequency range considered. From its expression it could also be recognized that its amplitude will always be small: at low frequency the numerator tends to zero, whilst at higher ones the inverse proportionality with f_s rules. Quantitatively, the aerodynamic damping reduction effect is much more relevant than the appearance of a tiny mass component which barely affects the inertia of the system.

The model just described is a semi-empirical extension of the quasi-static model of Chapter 4. The primary requirement of simplicity was totally respected. Unlike other dynamic inflow models suitable to be implemented in BEM codes, this prescinded from the description of the flow field, hiding the information about the induction's dynamics. Although, the target was utterly different: this model aimed at providing a quick tool for preliminary FOWT controller design. The focus was only on the integral thrust force, because of its importance for stability. The model's simplicity would allow usage in hand calculations too. The inclusion of dynamic effects occurred at the expense of a loss of generality. In fact, the proper tuning of the functions $\beta(f_{red})$ and $\varphi(f_{red})$ is fundamental, and their validity for different operating conditions or turbines must still be verified.

5.2.4 Model's parameters evaluation

The tuning of the extended model's parameters was performed referring to the AL simulations' results. In fact, before the delivery of the FVW data, the trends found with AL were the only ones available. Having assumed their validity, two regression analyses were performed to obtain the functions $\beta(f_{red})$ and $\varphi(f_{red})$. The only constraint to bear in mind was the requirement of quasi-static model generalisation: for $f_{red} \to 0$ the results of the extended model had to tend to those of the original one. Hence, at low frequencies the amplitude reduction coefficient had to tend to 1, whilst the phase delay had to tend to 0°. For what concerned the delay, its values could be simply obtained considering the difference $\varphi = -90^o - \phi^{AL}$, recalling that $\varphi > 0$ when the phase of ΔT was lower than -90°. The resulting trend with respect to the reduced frequency could be well

(a) φ **(b)** β
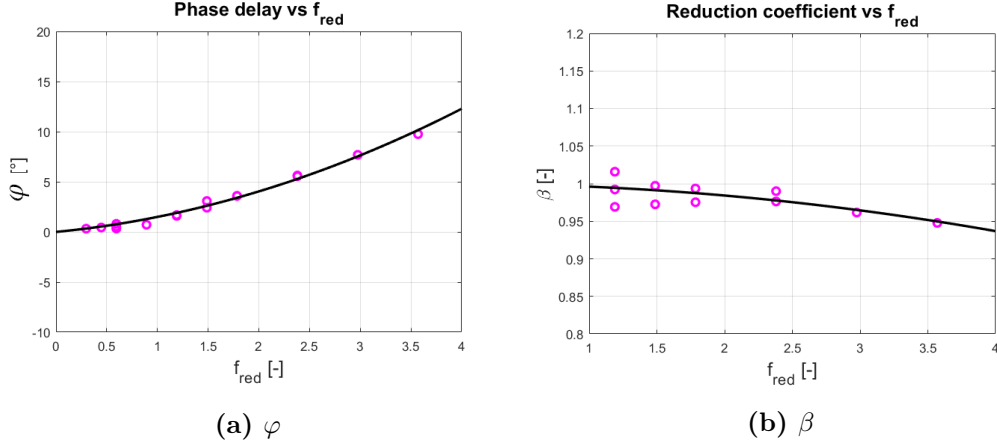
Figure 5.10: Regression analysis from AL simulations results

approximated by a parabola passing through the origin:

$$\varphi = \varphi(f_{red}) = a1 \cdot f_{red}^2 - a2 \cdot f_{red} \; ; \tag{5.17}$$

the coefficients $a1 \cong 0.5254$ and $a2 \cong 9695$, were determined with a least-square approach (pseudo-inverse matrix). The resulting fit is shown in fig.5.10a. The average error associated was below 0.26^o. A similar strategy was employed for the amplitude reduction coefficient. Also in this case the trend could be well represented with a parabola, passing from $\beta = 1$ at $f_{red} = 0$ and having its maximum thereby:

$$\beta = \beta(f_{red}) = 1 + b1 \cdot f_{red}^2 \; ; \tag{5.18}$$

once again, the coefficient $b1 = -3.149 \cdot 10^{-3}$ was determined with least-square minimisation. The corresponding plot is reported in fig.5.10b. The mean percentage error associated to the fit was below 0.7%.

5.2.5   Results comparison

The unsteady trends found with AL were confirmed by the FVW simulations, although with discrepancies in the exact values. In particular, both the reduction of the thrust oscillation amplitude and the phase delay appeared in free vortex results too. The comparison among out-of-UNAFLOW simulations and the quasi-static theory is first shown in fig.5.11 and 5.12. In the amplitude plot, the quasi-static slopes related to AL and FVW models were evaluated in order to highlight the non-linear effect at high frequencies. This was done simply
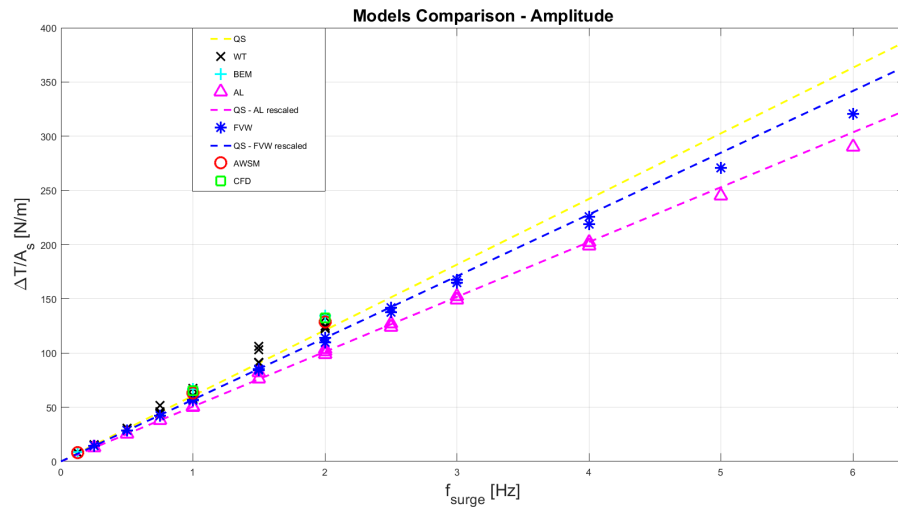
Figure 5.11: overall out-of-UNAFLOW amplitude comparison
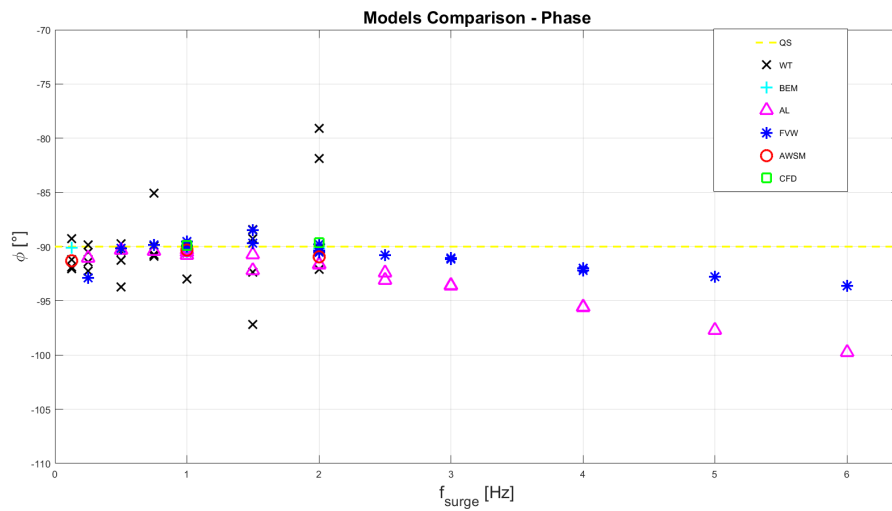
Figure 5.12: overall out-of-UNAFLOW phase comparison

obtaining c_0 from the lowest frequency test cases, rather than from its theoretical expression. Despite the absolute values were different, because of the reasons already addressed in Chapter 4, the amplitude reduction trends were definitely similar. Also in FVW results the amplitude reduction coefficient as function of f_{red} could be perfectly fitted by a parabola. The mean percentage error associated to the fit was about 0.86%. Compared to AL trend the reduction looked slightly more important, reaching almost 7% at the maximum frequency. It is expected that with the ongoing results revision, as soon as the steady performance gap will be eliminated adopting the same polars for all the models, a more accurate agreement will be achieved (Appendix C). With regard to the phase comparison, the FVW simulations found a slower phase reduction with respect to AL. The quadratic trend of φ was confirmed (mean error below 0.5^o), but it involved rather different fit coefficients. The maximum delay was around 4°, about half of what predicted by the AL. However, the clear parabolic behaviour found by both codes indicated that the nature of the unsteadiness was the same, with similar effects on the thrust oscillations. Once again the belief is that, with more consistent blade profiles' data, the values of the phases would be way more similar to each other.

For reference, the comparison in terms of equivalent aerodynamic coefficients is reported in fig.5.13 and 5.14. For a clearer representation only AL and FVW results have been included. The slight c_{aero} decrease was similarly foreseen by both the codes. Overall, the accordance between the results was satisfactory for the purposes of this work. Looking at m_{aero}, the models agreed on its smallness throughout the whole frequency range. Consistently with the phase shifts found, the sign of the aerodynamic mass was always negative above 2Hz. In the UNAFLOW range, the points were very close to zero with some scatter reflecting the distribution of ϕ values around -90°, caused by uncertainties (e.g. leakage issues). These errors were amplified at the lowest frequencies because of the inverse dependence of m_{aero} on f_s (eq.5.16). Therefore, the sharp reduction at 0.25Hz was deemed only caused by numerical troubles, i.e. unphysical.

To complete the comparison, the extended quasi-static model was included. It is worth to recall that β and φ were calibrated according to the regression analysis of AL results. The quasi-static aerodynamic damping (c_0) instead, was evaluated in different ways to remove the effects of steady thrust discrepancies. Results based on the theoretical c_0 (from eq.4.13) were referred to as QS_{ext};
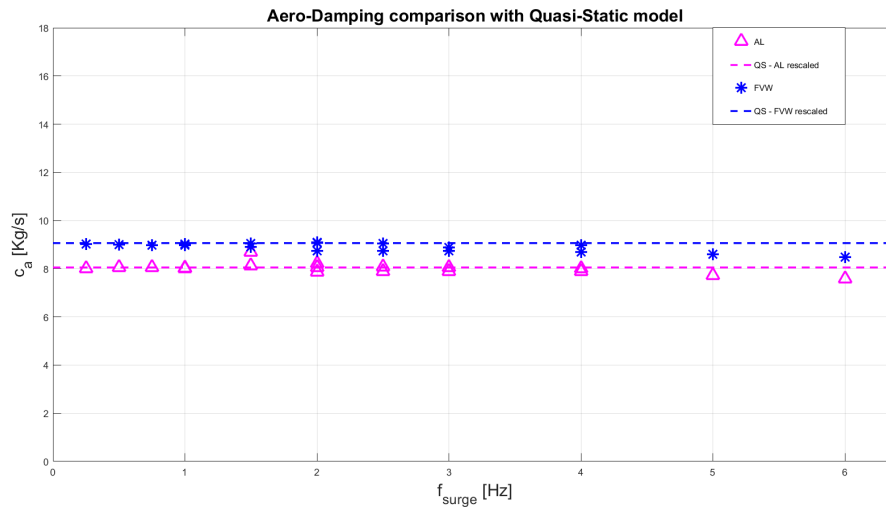
Figure 5.13: AL vs FVW aerodynamic damping comparison
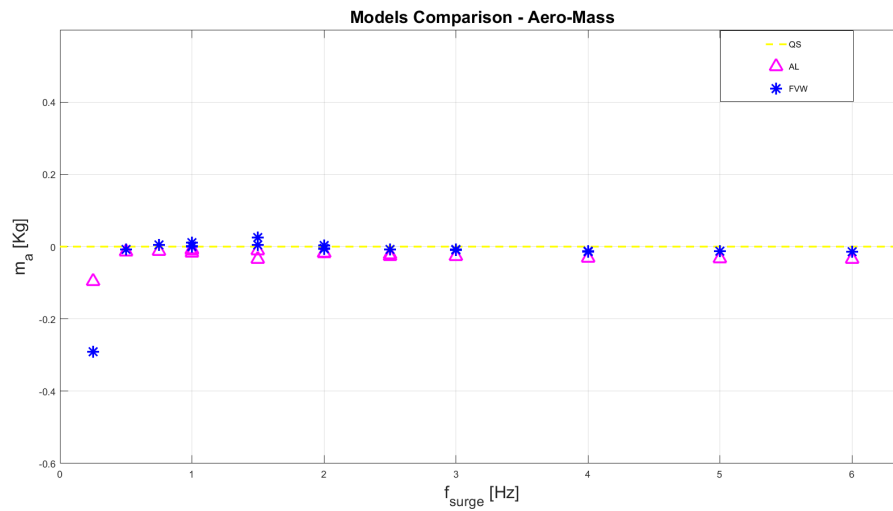
Figure 5.14: AL vs FVW aerodynamic mass comparison

the others, called "rescaled", estimated c_0 from the lowest frequency test of AL or FVW simulations respectively. The amplitude's comparison is shown in fig.5.15, the phase's in fig.5.16 and the aero-damping's in fig.5.17. Regarding the amplitude, despite the model's empirical parameters calibration was based on AL, the Quasi-Static FVW-rescaled results matched well with the free vortex simulations. This witnessed the similar amplitude reduction trend found by the two different models. The same conclusions of the amplitude case could drawn looking at the aero-damping comparison. Concerning the phase instead, the c_0 rescaling was avoided since it would not have had any effect. The only important parameter for the phase of the extended model was φ. Being it tuned after AL's results, the theoretical model followed their trend. The discrepancies with respect to FVW simulations were greater than in the amplitude case.
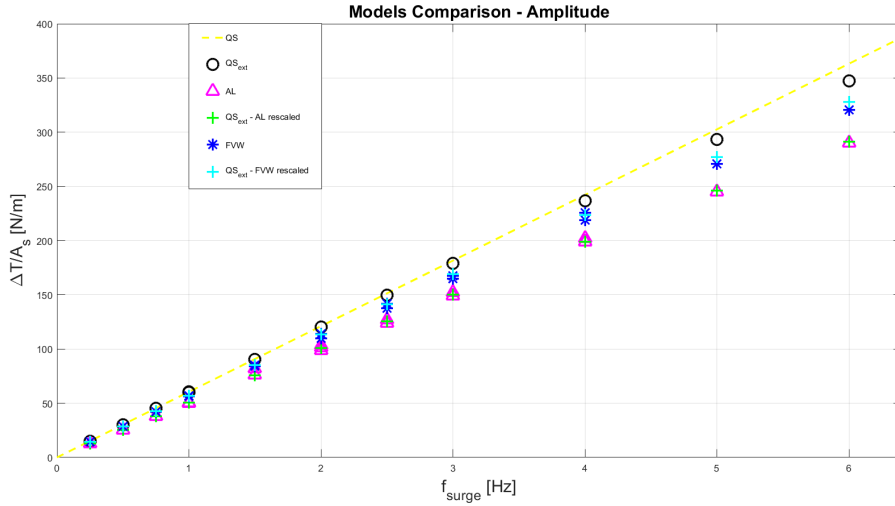
Figure 5.15: extended model amplitude comparison

5.2.6   Unsteady induction extraction

To gain further information on the unsteady surge behaviour, an attempt was made to investigate the induction dynamics featuring the Azimuthal Average Technique described in Chapter 4. The validity of such procedure still has to be verified, since the linearization of the axial velocity field on a streamline crossing the rotor might be inaccurate when surge occurs. In fact, in unsteady conditions the velocity profile might differ from what shown in fig.4.2b (Chapter 4), and the linear interpolation for the velocity in the rotor plane might be
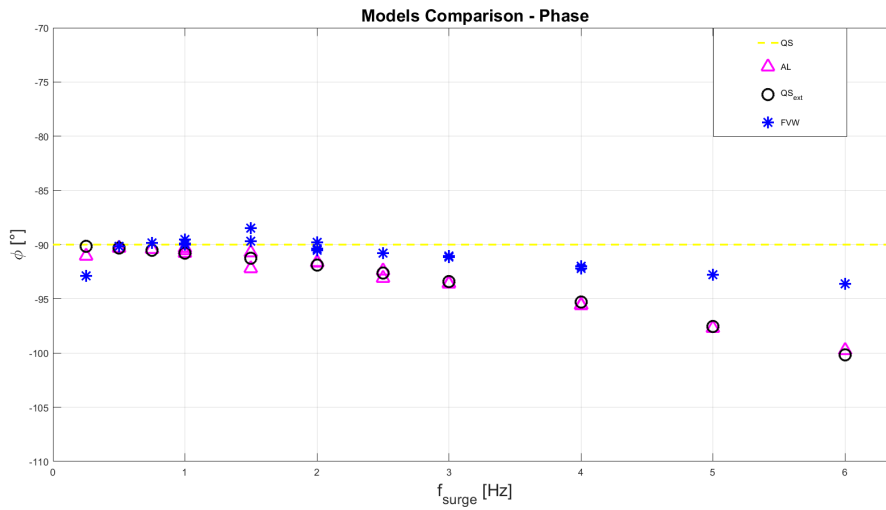
Figure 5.16: extended model phase comparison
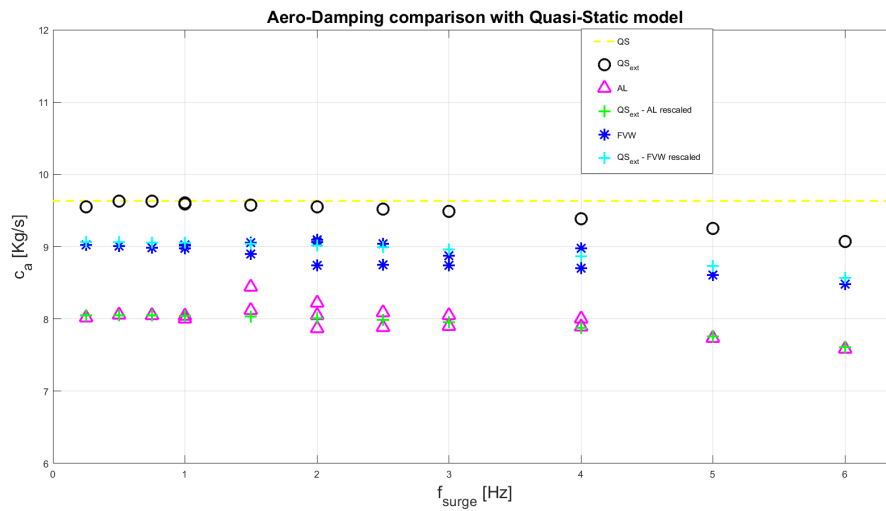
Figure 5.17: extended model aerodynamic damping comparison

ineffective. Moreover, since the sampling points could not be moved run time without implementing new pieces of code, the rotor plane was not equidistant from the sampling planes anymore. The turbine harmonically changed its position, i.e. moving back and forth with respect to the grid points. In order to take this into account eq.4.3 (Chapter 4) had to be adjusted; the position of the rotor plane had to be evaluated at each time step, considering the right point along the line of fig.4.2b. Therefore:

$$V_{a_i}^D(t) = c1 \cdot x + c2 \; ; \tag{5.19}$$

$$\text{with:} \qquad c1(t) = \frac{\overline{V}_{a_i}^{up}(t) - \overline{V}_{a_i}^{down}(t)}{x_{samp}^{up} - x_{samp}^{down}}; \qquad c2(t) = \overline{V}_{t_i}^{up}(t) - c1(t)\, x_{samp}^{up} \; ; \tag{5.20}$$

being x the surge signal, indicating the rotor plane's position. While the tangential induction could be calculated from eq.4.5 (Chapter 4) as in the steady case, the axial induction had to take the surge motion into account. Hence, the axial induction time history at radial position i was evaluated as:

$$a_i(t) = 1 - \frac{V_{a_i}^D(t) - \dot{x}}{V_w} = 1 - \frac{V_{a_i}^D(t) - \dot{x}}{V_0 - \dot{x}} \; . \tag{5.21}$$

Being aware of the large uncertainty involved, it was decided to test the outcome of this revised procedure for the highest frequency case: #10 of the out-of-UNAFLOW matrix. This way, at least an idea of the dynamic inflow effect could be drawn. The axial and tangential induction time histories obtained are shown in fig.5.18. The surge induced oscillation was clearly recognizable in the
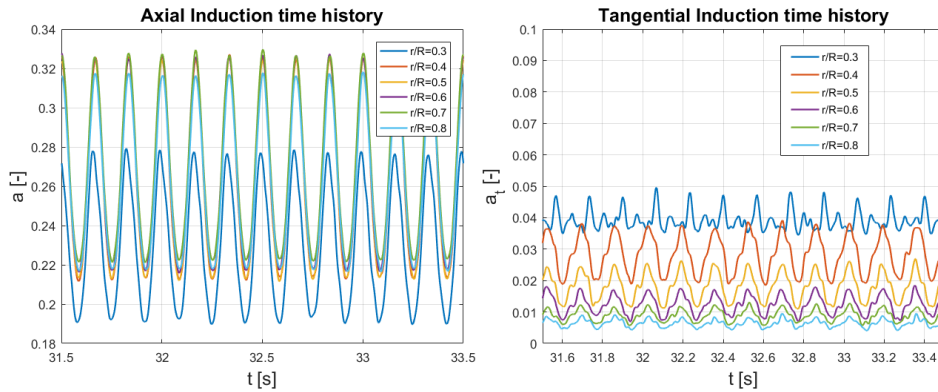
Figure 5.18: axial and tangential induction time histories for case #10

a signal; in a_t also other harmonic contributions could be appreciated. Once

again, the accuracy of the 30% span position was really uncertain. At first, the mean values of the histories were considered, to compare them against the steady induction profiles for validation. The results of this test are plotted in fig.5.19. The very good match found increased the confidence in the effectiveness of the approach followed. Focusing on the axial inductions, much more relevant than tangential, a Fourier decomposition was performed to assess amplitudes and phases of the induction oscillations (Δa_i) at the surge frequency. The spectra of the amplitudes for the different radial positions are reported in fig.5.20, where the values have been normalized with respect to the average inductions. In the case considered (i.e. $A_s = 20$mm and $f_s = 6$Hz) the peaks at the surge frequency were dominant at every radial position, standing around 20% of the mean induction values. Also the peaks of the second harmonics (at $2f_s$) were recognizable, but with much smaller extents. The phases of Δa_i at f_s, with respect to the surge displacement x are reported in fig.5.21. The quasi-static expected value was of 90°, since a had to be in phase with $\dot{x}$. In the case considered instead, a delay was observed throughout the span, consistently with dynamic inflow lag. The only exception was the 0.3R position, which was then assumed wrong. Despite the good qualitative performance of such method, the quantitative accuracy of the values obtained aroused some concerns. In fact, the phase delay of the integral thrust force could not be precisely linked to those of the axial induction along the span. Moreover, a physical interpretation for the resulting radial evolution of the phase delay could not be found.
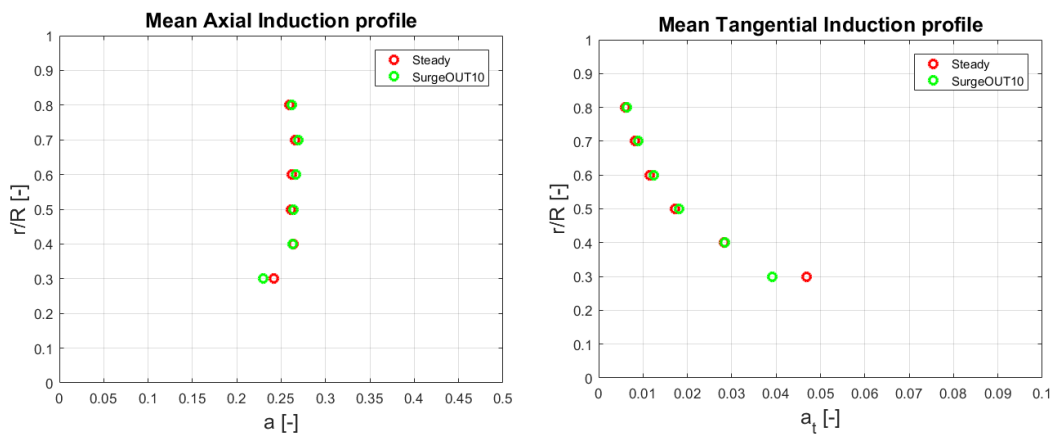
Figure 5.19: mean axial and tangential induction profiles

In conclusion, the accuracy of the strategy adopted was arguable and no
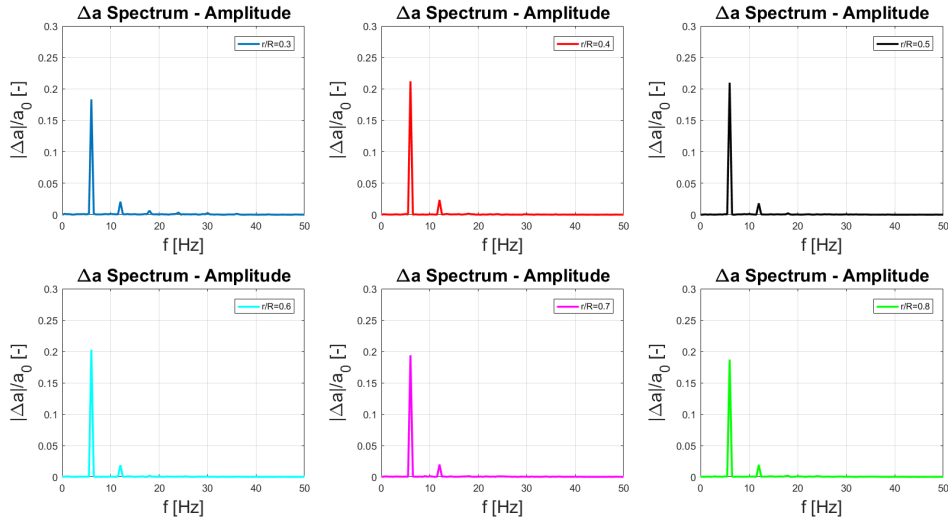
Figure 5.20: axial induction oscillation amplitude's spectrum for case #10

further analysis was conducted in absence of reference data to compare with. The purpose of spotting the unsteady behaviour of the induction field was only partially accomplished. Although, in order to link the phase delay of the induction field to the thrust force's one, a more suitable method should be employed. As suggested in Chapter 4, a great accuracy improvement could be reached using the method of Herráez et al. [63]. Even if this would require the effort of adding pieces of code, it would then save the tedious and error-prone data processing inherent to AAT. The strategy followed was anyway capable of confirming that an unsteady behaviour of the axial induction field was present as in classical dynamic inflow problems.
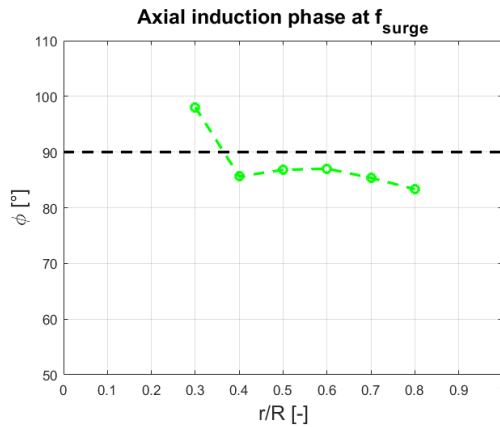
Figure 5.21: phase of Δa at f_s for case #10

5.3 Conclusions

In this Chapter, the results of the simulations conducted to extend the analysis of UNAFLOW have been shown. To investigate the limits of the quasi-static theory, the thrust force behaviour at different surge velocity amplitudes (ΔV) was studied. It was found that acting on A_s only, i.e. keeping the same reduced frequency, the simple model of Chapter 4 could perfectly represent the response without limitations. Increasing f_s instead, the reduced frequency was increased and some dynamic inflow effects arose. At first, a delay was observed on the phase of the thrust oscillation; then, at higher frequencies, also a reduction of $|\Delta T|$ could be recognized. Both these phenomena turned out to have a quadratic dependency on f_{red}, confirmed by both the numerical codes employed. The main consequence of such detachment from the quasi-static theory was a progressive reduction of the aerodynamic damping coefficient associated to the surge motion. Also a negative aerodynamic mass component appeared, but its effect on the system's dynamics was proved to be always small.

To account for these unsteady effects, a semi-empirical extension of the quasi-static model was proposed. The extended model was based on two parameters: an amplitude reduction coefficient (β) and a phase delay/shift (φ). Both these parameters were quadratic functions of f_{red}. The choice of the coefficients of such functions were made basing on the results of the AL simulations. A non-dimensional form for those expressions was adopted to keep as much generality as possible. More robust tuning of the coefficients will be fulfilled in future work, especially as soon as a better match between the codes will be achieved. The key asset of the model proposed is its simplicity, that would make it a powerful tool for preliminary FOWT controller design. Moreover, being a generalisation of the quasi-static model, it could be used at any reduced frequency without concerns on the accuracy. In fact, for $f_{red} \leq 1.5$ the results of the two models are almost identical. From what found in this Chapter, $f_{red} = 1.5$ can be assumed as a reference threshold for the validity of the quasi-static theory. Above that threshold, dynamic inflow effects become important and their quadratic trend can hardly be neglected. The simple integral approach combined with the physical soundness of the parameters involved, ensured this model to match the needs of control strategy designers clearly expressed by Pedersen [17].

From a practical point of view though, there are several reasons why surge

induced unsteadiness should not cause significant issues on FOWTs' operation. First of all, the frequencies that activate dynamic inflow effects are high enough to be associated to rather uncommon events. In the case considered for example, the f_{red} threshold corresponded to a real-scale frequency $f_s = 0.1$Hz that is usually in the right part of the waves' PSD peak already. Furthermore, the thrust oscillation amplitude reduction has a beneficial effect on the fatigue life of the turbine since it reduces the alternate stress. The only threat might be on the system's stability margins because of the reduction of the aerodynamic damping when f_s increases. Nevertheless, as long as c_0 is rather high, this effect should not be so dangerous. It is worth to recall that the rotor's control strategy enters in the expression for c_0. It is thus useful to be aware of this unsteady reduction so as to avoid to implement actions that might reduce the damping further. It is also important to notice that the contributions described account only for the aerodynamic part; also the structural and hydrodynamic shares will be important for stability analysis of a FOWT.

As anticipated, a revision work on the numerical models is currently ongoing to promote the use of the same polar data in the different codes (Appendix C). This refinement is expected to drastically reduce the discrepancies found in the steady turbine performances. Consequently, also a better match in the unsteady results will likely be obtained. Once the revised results will be available, also the expressions for the extended model's empirical parameters (β and φ) could be improved. The quadratic behaviour is expected to remain unchanged since it is seemed to be intrinsic in the dynamic inflow phenomenon. Indeed, the fact that both codes found similar trends despite their differences in absolute values, can hardly be thought as a coincidence. Once more refined results are obtained, it would be interesting to consider different operating conditions. This way, a more complete awareness on unsteady effects due to surge would be achieved, also allowing to test the extended model's prediction capabilities. More general expressions for the empirical parameters could be found with a non-dimensional analysis throughout the whole turbine's operating range. Finally, a simple step that will be performed in the near future is to start focusing on the dynamic behaviour of the torque (or power). All the simulations outputs already include the torque signals that only require little post-processing effort. In addition, the reference quasi-static model is already available (Appendix B) and, in presence of dynamic inflow effects, an extension similar to that of the thrust might be

developed. With such analysis, some light could be shed also on the unsteady behaviour of another important parameter to control. In that case though, no system's stability issues would be involved; the relevance would be more regarding the power output oscillation and the fatigue life of shaft and gearbox.

Chapter 6

Final Comments

With this Thesis a small brick in the characterisation of the unsteady behaviour of a FOWT was posed. The work performed confirmed the outcomes of previous studies first, then it went more in depth on the validity borders of the quasi-static theory, considering less common loading conditions. The outputs of this work were: an improved understanding of unsteady effects due to surge, a wide code validation campaign, the revision of UNAFLOW wind tunnel tests and, most importantly, two simple models capable of reproducing the obtained results. Those models might serve as useful tools for preliminary FOWT's controller design. Nevertheless, the focus of the Thesis was rather vertical and it only considered the thrust force response to the turbine's surge motion. To design a robust strategy, similar investigations have to be performed for each of the 6 degrees of freedom of the system. Moreover, other relevant quantities such as torque or blades' bending moments must be included in the analyses, to be aware of power output variations and fatigue loading conditions for example. Only a detailed and comprehensive knowledge of the unsteadiness involved would allow to reach the demanding LCOE reduction targets, making floating wind technology competitive in the market. In fact, an increased awareness would allow to design better control strategies increasing machines' lives, reducing O&M costs and mitigating investment's risk profile.

This final Chapter is divided in two sections: Section 6.1 resumes the main conclusions of the work performed; Section 6.2 gives a broader sight of the dynamic inflow field presenting possible future developments.

6.1   Main conclusions

The main conclusions of this Thesis can be resumed as:

1. **Quasi-static behaviour for $f_{red} \leq 1.5$**: up to that threshold dynamic inflow effects appeared to be negligible and the thrust response could be accurately characterised by the simple model of Chapter 4 (quadratic unsteady trends had still limited impact). In the case considered, the threshold corresponded to $f_s \leq 2.5$Hz at model's scale and $f_s^{real} \leq 0.1$Hz at full size. The generality of this threshold value has to be assessed by future works.

2. **Dynamic inflow effects scaled with f_{red}^2**: the variation from the quasi-static theory occurred with a delay in the phase of the thrust oscillation and a slighter reduction of its amplitude. Both the trends could be faithfully represented by quadratic curves. Despite the differences in the exact values between FVW and AL, the codes agreed on the parabolic trends. To account for dynamic inflow effects the extended model of Chapter 5 was developed.

3. **Codes validation**: the vast comparison in the UNAFLOW range showed a very good agreement among revised wind tunnel tests, quasi-static theory, CFD, AWSM and BEM models. The full CFD simulations were conducted by USTUTT [60], whilst both BEM and AWSM results were kindly provided by TNO. Author's AL and Corniglion's FVW simulations had some more troubles in matching the steady thrust and this reflected in the unsteady results too. Anyway, the trends found by those codes were always in good agreement with the theory. The different polar data employed are deemed to be the cause of such discrepancies. A revision work is ongoing aiming at a joint publication.

4. **Experimental awareness**: the dynamic amplification effects due to tower's flexibility were shown to be capable of biasing the results. The relevant inertial loads produced by the surge motion increasing f_s had a strong impact on the measurements. A proper inertia subtraction procedure had to be employed to avoid the problems encountered in LIFES50+. The details on the dynamic effects together with the different subtraction procedures and their limitations can be found in Chapter 2.

6.2 Dynamic inflow perspective and future works

The unsteady effects investigated in this Thesis were almost certainly induced by induction field lags, thus, they enter the wider dynamic inflow context that is being developed. The research on the unsteady effects triggered by wind gusts runs on a very close path with respect to surge induced unsteadiness. These cases are, indeed, two sides of the same coin. The only difference among the two is generated by the induction field; while in the surge case the velocity variation occurs directly "inside" the streamtube, changing the incoming wind the variation would be more "external". The analysis of the similarities and, eventually, differences between the two would be a very interesting path for the dynamic inflow research. This would shed more light on the contextualisation of the surge induced unsteadiness. It is clear now that the term dynamic inflow cannot be referred only to sudden load changes anymore. Furthermore, with the advent of FOWTs, the interest in finding a general model for rotor's unsteadiness has soared. Being the induction field reconfiguration delay the key mechanism common to all the cases, once a comprehensive sight is reached, an holistic model might be developed. Before trying to build up new ones though, it would be worth to test the capabilities of the latest dynamic inflow models like that of Yu [29]. This showed promising performances and it was already generalised for the varying wind case. Once more accurate results will be obtained from out-of-UNAFLOW simulations, it might be an opportunity to validate the predictions of other dynamic inflow models against those results. In the meantime, a nice experimental validation could be done considering the case of sinusoidally changing blades' pitch, comparing with numerical results from Yu et al. [66]. In a context with so many numerical codes available, there is an outstanding need of valuable experimental results.

The activity of Polimi in the near future will try to fill this experimental gap. Provided the tight relationship between FOWTs control and dynamic inflow effects, in future experimental campaigns there might be time to perform some code validation. The first step would be to consider simple pitch steps on the scaled turbine, to compare with classical dynamic inflow literature. Then, a simple upgrade could be the study of sinusoidal blade pitch changes comparing with numerical results. A big effort will be certainly devoted to the HIL technique for which coupled wind tunnel - water basin experiments are already planned. Those complex tests will give a strong push to the experimental characterisation

of FOWTs and the validation of the control strategies. If enough budget will be available, it might be possible to perform higher frequency surge tests to validate the results of this Thesis. In any case, it would be useful to obtain the scaled model's characteristic curves to improve the accuracy of the simple models proposed.

Appendix A

This appendix reports the complete test matrix of the UNAFLOW wind tunnel campaign. The list is divided in three tables, one for each wind condition: RATED1, RATED2 and ABOVE (see tab.2.1).

RATED1

UNAFLOW #	V_0 [m/s]	f_s [Hz]	A_s [m]	f_{red} [-]	λ [-]	Ω [rad/s]	ϑ_p [°]
1	2.41	0.125	0.125	0.123	7.77	150.3	0
2	2.42	0.125	0.12	0.123	7.74	150.3	0
3	2.42	0.125	0.08	0.123	7.74	150.3	0
4	2.42	0.125	0.04	0.123	7.74	150.3	0
5	2.4	0.25	0.08	0.248	7.8	150.3	0
6	2.39	0.25	0.06	0.249	7.84	150.4	0
7	2.41	0.25	0.04	0.247	7.77	150.3	0
8	2.41	0.25	0.02	0.247	7.77	150.3	0
9	2.42	0.5	0.04	0.492	7.74	150.3	0
10	2.41	0.5	0.03	0.494	7.77	150.3	0
11	2.41	0.5	0.02	0.494	7.77	150.2	0
12	2.41	0.5	0.01	0.494	7.77	150.3	0
13	2.42	0.75	0.03	0.738	7.74	150.3	0
14	2.41	0.75	0.02	0.74	7.77	150.2	0
15	2.4	0.75	0.015	0.744	7.8	150.3	0
16	2.41	0.75	0.007	0.74	7.77	150.3	0
17	2.42	1	0.03	0.983	7.74	150.3	0
18	2.42	1	0.025	0.983	7.74	150.3	0
19	2.42	1	0.015	0.983	7.73	150.2	0
20	2.43	1	0.008	0.98	7.7	150.2	0
21	2.42	1.5	0.015	1.475	7.73	150.2	0
22	2.42	1.5	0.01	1.475	7.74	150.3	0
23	2.43	1.5	0.007	1.47	7.71	150.3	0
24	2.43	1.5	0.0035	1.47	7.71	150.3	0
25	2.43	2	0.01	1.96	7.71	150.4	0
26	2.43	2	0.007	1.96	7.7	150.2	0
27	2.42	2	0.005	1.97	7.74	150.3	0
28	2.43	2	0.0025	1.96	7.71	150.3	0

RATED2

UNAFLOW #	V_0 [m/s]	f_s [Hz]	A_s [m]	f_{red} [-]	λ [-]	Ω [rad/s]	ϑ_p [°]
33	4	0.125	0.125	0.074	7.55	242.4	0
34	4	0.125	0.1	0.074	7.55	242.4	0
35	4.01	0.125	0.065	0.074	7.53	242.4	0
36	4	0.125	0.03	0.074	7.55	242.4	0
37	4.01	0.25	0.125	0.148	7.53	242.4	0
38	4	0.25	0.1	0.149	7.55	242.4	0
39	4	0.25	0.065	0.149	7.55	242.4	0
40	4	0.25	0.035	0.149	7.55	242.4	0
41	4	0.5	0.065	0.297	7.55	242.4	0
42	4.01	0.5	0.05	0.297	7.53	242.4	0
43	4	0.5	0.035	0.297	7.55	242.4	0
44	4.01	0.5	0.015	0.297	7.53	242.4	0
45	4	0.75	0.04	0.446	7.55	242.4	0
46	4.01	0.75	0.03	0.445	7.53	242.4	0
47	4	0.75	0.02	0.446	7.55	242.4	0
48	4	0.75	0.01	0.446	7.55	242.4	0
49	4	1	0.05	0.595	7.55	242.2	0
50	4	1	0.035	0.595	7.55	242.2	0
51	4	1	0.025	0.595	7.55	242.3	0
52	3.99	1	0.01	0.596	7.57	242.3	0
53	4	1.5	0.02	0.892	7.55	242.2	0
54	4	1.5	0.015	0.892	7.55	242.2	0
55	4	1.5	0.01	0.892	7.55	242.2	0
56	4	1.5	0.005	0.892	7.55	242.2	0
57	4	2	0.015	1.19	7.55	242.2	0
58	3.99	2	0.0125	1.193	7.56	242.2	0
59	4.01	2	0.008	1.187	7.53	242.2	0
60	4	2	0.004	1.19	7.55	242.2	0

ABOVE

UNAFLOW #	V_0 [m/s]	f_s [Hz]	A_s [m]	f_{red} [-]	λ [-]	Ω [rad/s]	ϑ_p [°]
65	6.06	0.125	0.125	0.049	5.47	265.9	12.5
66	6.05	0.125	0.1	0.049	5.47	265.8	12.5
67	6.06	0.125	0.065	0.049	5.47	265.9	12.5
68	60.6	0.125	0.03	0.049	5.47	265.8	12.5
69	6.07	0.25	0.125	0.098	5.46	265.8	12.5
70	6.07	0.25	0.1	0.098	5.46	265.9	12.5
71	6.07	0.25	0.065	0.098	5.46	266	12.5
72	6.08	0.25	0.03	0.098	5.45	266	12.5
73	6.06	0.5	0.1	0.196	5.45	265.2	12.5
74	6.06	0.5	0.075	0.196	5.47	265.8	12.5
75	6.07	0.5	0.05	0.196	5.46	265.8	12.5
76	6.07	0.5	0.025	0.196	5.46	265.8	12.5
77	6.07	0.75	0.065	0.294	5.44	265	12.5
78	6.07	0.75	0.05	0.294	5.45	265.4	12.5
79	6.07	0.75	0.03	0.294	5.46	265.8	12.5
80	6.06	0.75	0.015	0.295	5.46	265.7	12.5
81	6.06	1	0.07	0.393	5.43	264.3	12.5
82	6.06	1	0.05	0.393	5.45	264.9	12.5
83	6.07	1	0.035	0.392	5.46	265.8	12.5
84	6.06	1	0.018	0.393	5.46	265.7	12.5
85	6.06	1.5	0.03	0.589	5.45	264.8	12.5
86	6.07	1.5	0.025	0.588	5.45	265.7	12.5
87	6.06	1.5	0.015	0.589	5.47	265.9	12.5
88	6.06	1.5	0.008	0.589	5.47	265.8	12.5
89	6.07	2	0.018	0.784	5.42	264	12.5
90	6.06	2	0.0125	0.785	5.47	265.8	12.5
91	6.06	2	0.006	0.785	5.47	265.8	12.5

Appendix B

In this appendix a quasi-static model, similar to that of Chapter 4 is developed, for the output power oscillation ΔP. The procedure is exactly the same as for the thrust, but this time the power coefficient is involved:

$$P_0 = \frac{1}{2}\rho A_D \, C_p(\lambda)V_0^3 \; ; \tag{B.1}$$

being the power coefficient a function of the Tip Speed Ratio (λ). As for the thrust, the surge motion must be taken into account and the unsteady expression for the power becomes:

$$P(\dot{x}) = \frac{1}{2}\rho A_D \, C_p(\lambda_w)V_w^3 \; ; \tag{B.2}$$

being V_w and λ_w defined by eq.4.7 and 4.8 respectively. Once again, to obtain the simple model it is enough to linearize eq.B.2 assuming small surge velocity ($\dot{x} \to 0$) which, in case of harmonic surge, can be translated to a condition on the displacement amplitude ($A_s \to 0$). Thus, using Taylor's expansion truncated at the first order:

$$P(\dot{x}) \approx P_0 + \frac{dP}{d\dot{x}}|_{\dot{x}=0} \; ; \tag{B.3}$$

$$\frac{dC_p}{d\dot{x}}|_{\dot{x}=0} = \frac{dC_p}{d\lambda_w}|_{\dot{x}=0} \cdot \frac{d\lambda_w}{d\dot{x}}|_{\dot{x}=0} = \frac{dC_p}{d\lambda}|_{\lambda_0} \cdot \frac{\Omega \, R}{V_0^2} \; ; \tag{B.4}$$

$$\frac{dP}{d\dot{x}}|_{\dot{x}=0} = \frac{1}{2}\rho A_D [\frac{dC_p}{d\lambda}|_{\lambda_0} \Omega R V_0 - 3V_0^2 \, C_p(\lambda_0)] \; . \tag{B.5}$$

Defining:

$$\zeta_0 = \frac{1}{2}\rho A_D V_0 \, [3V_0 \, C_p(\lambda_0) - \frac{dC_p}{d\lambda}|_{\lambda_0} \Omega R] = -\frac{dP}{d\dot{x}}|_{\dot{x}=0} \; ; \tag{B.6}$$

finally, the linear expression for the power oscillation depending on the surge velocity can be written as:

$$\Delta P(\dot{x}) = P(\dot{x}) - P_0 \approx -\zeta_0 \, \dot{x} \, . \tag{B.7}$$

As for the thrust, where the dynamics was ruled by c_0, the power oscillation depends only the steady operating conditions via the term ζ_0. Acting on a different degree of freedom, this will be just an external excitation to the power caused by the surge motion. For this reason, it makes no sense to speak about damping coefficient. Therefore, ζ_0 only gives the effect of the surge oscillation on the turbine's power harvesting.

If a typical unregulated power curve is taken as reference (i.e. similar in shape to a negative concavity parabola), three zones can be distinguished: at low λ the term $\frac{dC_p}{d\lambda}|_{\lambda_0} > 0$, but being V_0 high the first term is likely to prevail, i.e. $\zeta_0 > 0$; at the optimal TSR the derivative term is null and again $\zeta_0 > 0$; at high λ $\frac{dC_p}{d\lambda}|_{\lambda_0} < 0$, then is always $\zeta_0 > 0$. The physical interpretation of having a positive ζ_0 is straightforward; it means that the power output always increases when the turbine moves against the wind ($-x$ direction) and vice versa. As for the thrust force, in the quasi-static case the phase is at -90° with respect to the surge displacement. It is worth to recall that, even in this case, the action of the controller affects the characteristic curve entering in the expression of ζ_0.

Appendix C

In this appendix the outcomes of the AL simulations revision are presented. The new results have been obtained right across the deadline for the submission of the Thesis, when all the chapters had already been completed. Hence, to guarantee the value of the dissertation, it has been decided to append them here avoiding to rush them into the previous chapters with little time to develop a thorough analysis. The revision relied on additional data kindly provided for the Author by TNO, aiming at a joint publication. Without their help the source of error could never be spotted among so many possibilities. Unfortunately though, the timing has not allowed to include the new results in the core of this Thesis. Anyway, the updated simulations' outcomes have not affected the validity of any of the conclusions drawn throughout the work. The new results have only improved the agreement among AL, experiments and other codes, confirming all the trends previously found. Only the hypotheses made in Chapter 4 (Section 4.1) on the possible causes of the thrust deficit, albeit reasonable, have been confuted by the new evidences.

The first step has been the revision of the polar data and blade parameters, originally inserted by Bernini, to adopt the same polars of TNO's codes. This modification resulted in a further reduction of both thrust and torque predictions in steady RATED2 conditions. This brought the will of comparing the spanwise axial and tangential loads distributions, which were then made available by TNO. Such distributions broke the hypotheses made in Chapter 4: the mismatch was not just confined at the root sections. Instead, it was spread throughout the whole span, although the shapes of the distributions were very similar. With this evidence it became clear that the fault was inside the code. Finally, after having double-checked all inputs and outputs of every single calculation within the solver, a trivial bug has been found. In the code version used, i.e. the one allowing the motion of the turbine, the multiplication of the obtained loads times the air

density when printing the outputs was missing. Indeed, being an incompressible solver, it was right to evaluate everything per unit density, but then the outputs were supposed to be multiplied by the reference ρ to obtain proper physical dimensions. This explained why the load distributions shapes, obtained with the new polars, were so similar: there was just a proportionality constant to be accounted for.

Having solved the issue, tab.4.1 from Chapter 4 has been updated (tab.C.1). The new AL error on the thrust force with respect to the experiments has become of excess, but just below 2%, with the torque's one lower than 4%. It is worth to notice the remarkable agreement with the full CFD model, where the wind tunnel section had been considered. For this reason, the source of the discrepancies with respect to 1/3 CFD, AWSM and BEM models have been associated to the lack of blockage effect in those results.

	WT	AL	CFD	CFD 1/3	AWSM	BEM	FVW
Thrust [N]	35.91	36.6	36.57	34.2	34.5	34.65	31.73
Torque [Nm]	3.32	3.45	3.34	2.91	2.97	2.93	2.83

Table C.1: updated steady comparison: UNAFLOW RATED2 conditions

As expected, having fixed the steady performances has resulted in a relevant improvement of the quantitative agreement among unsteady results too. The up to date comparison in terms of amplitude, phase, aero-damping and aero-mass, relative to the thrust oscillation component at f_s, is shown in fig.C.1. The most evident improvement has been achieved on the amplitude indeed, where the slope of the linear trend has got much closer to that of the experiments and of other codes. The high frequency amplitude reduction effect, quadratically dependent on f_{red}, has been confirmed and the agreement with FVW results has improved. For what concerns the phases, the values have become just slightly higher (i.e. less negative) than before and the quadratic reduction with f_{red} has been found again. The phase difference with respect to FVW is still relevant at high frequencies, but it is expected that inserting the same polars in the FVW code will reduce this scatter. As a consequence, also the aerodynamic coefficients matching has improved leaving the trends unchanged. Hence, the effectiveness of the extended quasi-static model of Chapter 5 has been utterly confirmed; the only difference is in the coefficients of the parabolic fits (eq.5.17 and 5.18) that have to be re-evaluated.

(a) Amplitude

(b) Phase

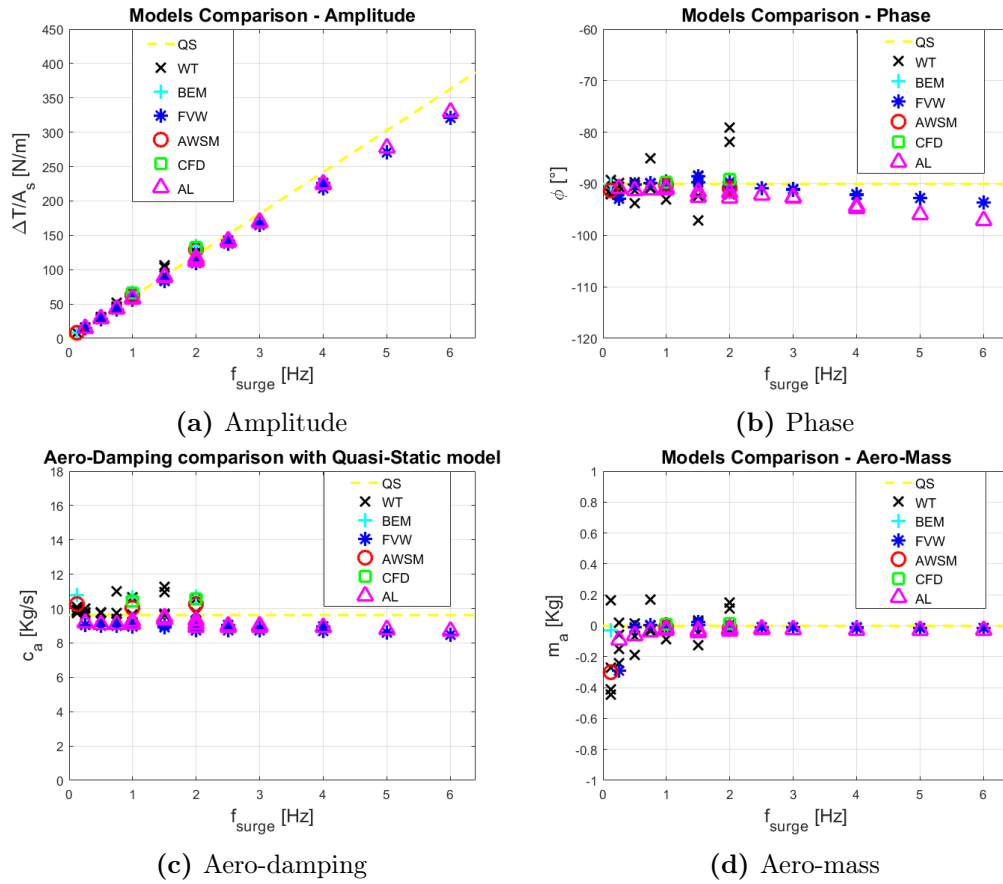**(c)** Aero-damping

(d) Aero-mass

Figure C.1: updated overall comparison

In conclusion, the good results finally obtained have increased the confidence in the capabilities of the AL code employed, without discrediting any of the final considerations made in Chapter 6.

Bibliography

[1] UNFCCC: Paris Agreement. December 2015.

[2] IEA (2019), Renewables Information 2019, IEA, Paris. Available at: `https://www.iea.org/reports/renewables-information-2019`

[3] GWEC, Global Wind Report 2018. April 2019. Available at: `https://gwec.net/global-wind-report-2018/`

[4] IEA (2019), Offshore Wind Outlook 2019, IEA, Paris. Available at: `https://www.iea.org/reports/offshore-wind-outlook-2019`

[5] Sebastian T., Lackner M.A., "Characterization of the unsteady aerodynamics of offshore floating wind turbines". *Wind Energy* (2013) 16:339-352. DOI: 10.1002/we.545

[6] Tran T.T., Kim D.H., "The aerodynamic interference effects of a floating offshore wind turbine experiencing platform pitching and yawing motions". *Journal of Mechanical Science and Technology* 29 (2) (2015) 549-561. DOI: 10.1007/s12206-015-0115-0

[7] Tran T.T., Kim D.H., "A CFD study into the influence of unsteady aerodynamic interference on wind turbine surge motion". *Renewable Energy* 90 (2016) 204-228. Available at: `http://dx.doi.org/10.1016/j.renene.2015.12.013`

[8] Tran T.T., Kim D.H., "Fully coupled aero-hydrodynamic analysis of a semi-submersible FOWT using a dynamic fluid body interaction approach". *Renewable Energy* 92 (2016) 244-261. Available at: `http://dx.doi.org/10.1016/j.renene.2016.02.021`

Bibliography

---

[9] Liu Y., Xiao Q., Incecik A., Peyrard C., Wan D., "Establishing a fully coupled CFD analysis tool for floating offshore wind turbines". *Renewable Energy* 112 (2017) 280-301. Available at: `http://dx.doi.org/10.1016/j.renene.2017.04.052`

[10] Bayati I., Belloli M., Bernini L., Zasso A., "Wind tunnel validation of AeroDyn within LIFES50+ project: imposed Surge and Pitch tests". *Journal of Physics* (2016): Conference Series. 753(9). DOI: 10.1088/1742-6596/753/9/092001

[11] Bernini L. et al., "UNAFLOW: Report". Technical Report, 2018.

[12] Bayati I., Belloli M., Facchinetti A., Giappino S., "Wind tunnel tests on floating offshore wind turbines: a proposal for hardware-in-the-loop approach to validate numerical codes". *Wind Engineering*, 2012. Available at: `https://doi.org/10.1260/0309-524X.37.6.557`

[13] Schepers J.G., "Engineering models in wind energy aerodynamics". PhD Thesis, TUD, November 2012.

[14] Schepers J.G., Boorsma K. et al., "Final report of IEA Task 29, Mexnext (Phase 1): Analysis of MEXICO wind tunnel measurements". ECN-E-12-004, Energy Research Center of the Netherlands, February 2012.

[15] Schepers J.G., Boorsma K. et al., "Final report of IEA Task 29, Mexnext (Phase 2): Analysis of MEXICO wind tunnel measurements". ECN-E-14-060, Energy Research Center of the Netherlands, December 2014.

[16] Schepers J.G., Boorsma K. et al., "Final report of IEA Task 29, Mexnext (Phase 3): Analysis of MEXICO wind tunnel measurements". ECN-E-18-003, Energy Research Center of the Netherlands, January 2018.

[17] Pedersen M.D., "Stabilization of Floating Wind Turbines". PhD Thesis, NTNU, June 2017.

[18] Burton T., Sharpe D., Jenkins N., Bossanye E., "Wind Energy Handbook". John Wiley and Sons, 2001.

[19] Carpenter P., Fridovich B., "Effect of a rapid blade-pitch increase on the thrust and induced-velocity response of a full-scale helicopter rotor". NACA Technical Report, Washington, November 1953.

[20] Pitt D., Peters D., "Theoretical prediction of dynamic-inflow derivatives". paper 47: SIXTH EUROPEAN ROTORCRAFT AND POWERED LIFT AIRCRAFT FORUM, September 1980.

[21] Øye S., "Tjæreborg wind turbine, 4. dynamic inflow measurement". Technical report, DTU, Lyngby, 1991.

[22] Snel H., Schepers, J., "Joint investigation of dynamic inflow effects and implementation of an engineering method". Technical report, ECN-C-94-107, Energy Research Center of the Netherlands, April 1995.

[23] Schepers J.G., "IEA Annex XX: Dynamic Inflow effects at fast pitching steps on a wind turbine placed in the NASA-Ames wind tunnel". ECN-E-07-085, Energy Research Center of the Netherlands, October 2007.

[24] Madsen H.A. et al., "The DAN-AERO MW Experiments Final report". Technical report, Risø DTU, 2010.

[25] Troldborg N. et al., "DANAERO MW: Final Report". DTU Wind Energy. DTU Wind Energy E, No. 0027(EN), 2013.

[26] Pirrung G.R., Madsen H.A., "Dynamic inflow effects in measurements and high-fidelity computations". *Wind Energy Science*, 3, 545–551, 2018. Available at:https://doi.org/10.5194/wes-3-545-2018

[27] Hammam M.M.A., "Analytical Unsteady Aerodynamic Models for Horizontal Axis Wind Turbines". PhD Thesis, University of Calgary, March 2016.

[28] Yu W. et al.,"Validation of engineering dynamic inflow models by experimental and numerical approaches". *Journal of Physics*: Conf. Ser. 753 022024, 2016. DOI:10.1088/1742-6596/753/2/022024

[29] Yu W., "The wake of an unsteady actuator disc". PhD Thesis, TUD, April 2018.

[30] van der Deijl W.E., "Dynamic wind speed in dynamic inflow models". M.Sc. Thesis, TUD, July 2018.

Bibliography

[31] Berger F., Kühn M., "Experimental investigation of dynamic inflow effects with a scaled wind turbine in a controlled wind tunnel environment". *Journal of Physics*: Conf. Series 1037 (2018) 052017. DOI:10.1088/1742-6596/1037/5/052017

[32] Berger F. et al., "Dynamic inflow due to gusts – an experimental wind tunnel study". Cork Wind Energy Science Conference, June 2019.

[33] Bayati I. et al., "UNAFLOW project: UNsteady Aerodynamics of FLOating Wind turbines". *Journal of Physics*: Conf. Series 1037 (2018) 072037. DOI:10.1088/1742-6596/1037/7/072037

[34] Boldrin D.M., "Wind Turbines Unsteady Aerodynamics: Experimental Analysis of Thrust and Wake Velocity". M.Sc. Thesis, POLIMI, April 2018.

[35] Bak C. et al., "Description of the DTU 10 MW reference wind turbine". DTU Wind Energy, July 2013.

[36] Bayati I., Belloli M., Bernini L., Zasso A., "Aerodynamic design methodology for wind tunnel tests of wind turbine rotors". *Journal of Wind Engineering & Industrial Aerodynamics*. 167. pp.217-227. 2017. DOI:10.1016/j.jweia.2017.05.004

[37] Bayati I., Bernini L., Zanotti A., Belloli M., Zasso A., "Experimental investigation of the unsteady aerodynamics of FOWT through PIV and hot-wire wake measurements". *Journal of Physics*: Conf. Series 1037 (2018) 052024. DOI:10.1088/1742-6596/1037/5/052024

[38] Bayati I., Belloli M., Bernini L., Zasso A., "A Formulation for the Unsteady Aerodynamics of Floating Wind Turbines, with Focus on the Global System Dynamics". Proceedings of ASME 2017 36th International Conference on Ocean, Offshore and Arctic Engineering, OMAE2017. Trondheim, Norway. 10(57786), June 25-30 2017. DOI:10.1115/OMAE2017-61925

[39] Schito P., "Large Eddy Simulation of wind turbines: interaction with turbulent flow". PhD Thesis, POLIMI, 2011.

[40] Bernini L., Caccialanza M.M., "Development of the Effective Velocity Model for wind turbines aerodynamics numerical simulation through an Actuator Line approach". M.Sc. Thesis, POLIMI, 2015.

[41] Sørensen J.N., Carsten W.K., "A model for unsteady rotor aerodynamics", *Journal of fluids engineering*, 1995. DOI:10.1016/0167-6105(95)00027-5

[42] Sørensen J.N., Shen W.Z., "Numerical modelling of wind turbine wakes". *Journal of fluids engineering* 124 (2002), 393–399. DOI:10.1115/1.1471361

[43] Sørensen J.N. et al., "Simulation of wind turbine wakes using the actuator line technique". Phil. Trans. R. Soc. A 373: 20140071, 2015. Available at: `http://dx.doi.org/10.1098/rsta.2014.0071`

[44] Mikkelsen R., "Actuator Disc Methods Applied to Wind Turbines". PhD Thesis, DTU, June 2003.

[45] Troldborg N., "Actuator Line Modeling of Wind Turbine Wakes". PhD Thesis, DTU, June 2008.

[46] Shen W.Z., Zhang J.H., Sørensen J.N., "The actuator surface model: a new Navier–Stokes based model for rotor computations". *Journal of Solar Energy Engineering* (2009) 131: 011002–1–011002–9. DOI:10.1115/1.3027502

[47] Martinez-Tossas L.A., Churchfield M.J., Leonardi S., "Large eddy simulations of the flow past wind turbines: actuator line and disk modelling". *Wind Energy* (2015), 18:1047–1060. DOI:10.1002/we.1747

[48] Ivanell S., Sørensen J.N., Mikkelsen R, Henningson D., "Analysis of numerically generated wake structures". *Wind Energy* (2009), 12:63–80. DOI:10.1002/we.285

[49] Li P., Cheng P., Wan D., Xiao Q., "Numerical Simulations of Wake Flows of Floating Offshore Wind Turbines by Unsteady Actuator Line Model". 9th International Workshop on Ship and Marine Hydrodynamics, 26 – 28 August 2015, Glasgow, UK.

[50] Cheng P., Huang Y., Wan D., "A numerical model for fully coupled aero-hydrodynamic analysis of floating offshore wind turbine". *Ocean Engineering* 173 (2019), 183–196. Available at: `https://doi.org/10.1016/j.oceaneng.2018.12.021`

[51] Melani P.F., "Experimental Assessment of an Actuator Line Simulation Tool for Vertical Axis Wind Turbines". M.Sc. Thesis, POLIMI, July 2018.

[52] Martínez-Tossas L.A., Churchfield M.J., Meneveau C., "A Highly Resolved Large-Eddy Simulation of a Wind Turbine using an Actuator Line Model with Optimal Body Force Projection". *Journal of Physics*: Conf. Series 753 (2016) 082014. DOI:10.1088/1742-6596/753/8/082014

[53] Martínez-Tossas L.A., Churchfield M.J., Meneveau C., "Optimal smoothing length scale for actuator line models of wind turbine blades based on Gaussian body force distribution". *Wind Energy* (2017), 20:1083–1096. DOI: 10.1002/we.2081

[54] Piomelli U., Chasnov J.R., "LARGE-EDDY SIMULATIONS: THEORY AND APPLICATIONS". From: Hallbäck et al., "Turbulence and Transition Modelling", 1996 Kluwer Academic Publishers, Chapter 7, pp.269-336.

[55] Sarlak H., Meneveau C., Sørensen J.N., "Role of subgrid-scale modeling in large eddy simulation of wind turbine wake interactions". *Renewable Energy* 77 (2015) 386-399. Available at: `http://dx.doi.org/10.1016/j.renene.2014.12.036`

[56] Deskos G., Sylvain L., Piggott M.D., "Turbulence-resolving simulations of wind turbine wakes". *Renewable Energy* 134 (2019) 989-1002. Available at: `https://doi.org/10.1016/j.renene.2018.11.084`

[57] Rahimi H. et al., "Evaluation of different methods for determining the angle of attack on wind turbine blades with CFD results under axial inflow conditions". *Renewable Energy* 125 (2018) 866-876. Available at: `https://doi.org/10.1016/j.renene.2018.03.018`

[58] Hansen M.O.L., Sørensen N.N., Sørensen J.N., Michelsen J.A., "Extraction of lift, drag and angle of attack from computed 3-d viscous flow around a rotating blade". Proceedings of the European Wind Energy Conference, Irish Wind Energy Association, 1998.

[59] Johansen J., Sørensen N.N., "Aerofoil Characteristics from 3D CFD Rotor Computations". *Wind Energy* (2004), 7:283–294. DOI: 10.1002/we.127

[60] Cormier M., Caboni M., Lutz T., Boorsma K., Kramer E., "Numerical analysis of unsteady aerodynamics of floating offshore wind turbines". *Journal of Physics*: Conf. Series 1037 (2018) 072048. DOI:10.1088/1742-6596/1037/7/072048

[61] Boorsma K., Grasso F., Holierhoek J.G., "Enhanced approach for simulation of rotor aerodynamic loads". Technical Report ECN-M–12-003, ECN, presented at EWEA Offshore 2011, Amsterdam, 29 November 2011 - 1 December 2011.

[62] de Vaal J.B., Hansen M.O.L., Moan T., "Effect of wind turbine surge motion on rotor thrust and induced velocity". *Wind Energy* (2014), 17:105–121. DOI: 10.1002/we.1562

[63] Herráez I., Daniele E., Schepers J.G., "Extraction of the wake induction and angle of attack on rotating wind turbine blades from PIV and CFD results". *Wind Energy Science*, 3, 1–9, 2018. DOI: 10.5194/wes-3-1-2018

[64] Sørensen N.N., Madsen H.A., "Modelling of transient wind turbine loads during pitch motion (paper and poster)". *Proceedings (online)* Brussels: European Wind Energy Association (EWEA).

[65] Bayati I., Belloli M., Bernini L., Zasso A., "Wind Tunnel Wake Measurements of Floating Offshore Wind Turbines". *Energy Procedia* (2017), 137:214-222. DOI: 10.1016/j.egypro.2017.10.375

[66] Yu W., Tavernier D., Ferreira Gijs C., van Kuik A.M., Schepers G., "New dynamic-inflow engineering models based on linear and nonlinear actuator disc vortex models". *Wind Energy* (2019), 17:105–121. DOI: 10.1002/we.1562